Remote Sensing of Aerosol and Cloud Properties from Ground Based and Satellite Remote Sensors to Explore Aerosol-Cloud Interaction

by

Yuzhe He

A thesis submitted to the Graduate Faculty in
Electrical Engineering in partial fulfilment of the
requirements for the degree of Doctor of Philosophy,
The City University of New York

2012

This manuscript has been read and accepted for the
Graduate Faculty in Engineering in satisfaction of the
dissertation requirement for the degree of Doctor of Philosophy.

Prof. Barry Gross

Date

Chair of Examining Committee

Dean Ardie D. Walser

Date

Executive Officer

Prof. Fred Moshary
Prof. Jorge Gonzalez
Dr. Mark Arend
Dr. Andrew Heidinger
Supervisory committee

THE CITY UNIVERSITY OF NEW YORK

Abstract

Remote Sensing of Aerosol and Cloud Properties
from Ground Based and Satellite Remote Sensors to
Explore Aerosol-Cloud Interaction

by

Yuzhe He

Adviser: Professor Barry Gross

The measurements of both aerosol and cloud properties are critical for climate studies since these mechanisms have the largest uncertainty in energy balance calculations. In addition, aerosols and clouds do not act independently but can significantly couple to each other. It is clear that being able to quantify these interactions is crucial to climate models. While there are many possible aerosol-cloud interactions, we limit our investigation to the Twomey indirect effect which relates how aerosols can modify the physical properties of clouds thereby changing the radiative properties.

Verifying and quantifying such machanisms on a global scale requires accurate measurements of both aerosols and clouds from satellites. Unfortunately, assessing this mechanism has been very difficult from satellites since both aerosols and cloud properties would have to be simultaneously measured. Therefore, only statistical approaches have been tried but it is easy to see that such approaches will tend to obscure the interpretation of local interaction mechanisms.

In this thesis, we investigate the potential of both satellites and ground based approaches to measure aerosol cloud interaction parameters. After assessing the limitations of satellite based approaches, we focus on the use of ground based remote sensing using a combination

of Lidar, Microwave radiometry, Doppler Lidar and sky radiometry. This instrumentation suite offers a more direct approach that can probe the properties of both aerosols and clouds simultaneously allowing us to investigate real time aerosol-cloud processes which occur on time scale < 1 minute.

To this end, we first provide a thorough description of the multi-sensor approach and how it can be implemented including a sensitivity analysis taking into account both atmospheric and surface variability as well as uncertainty in both the Liquid Water Path (LWP) and diffuse transmittance measurements. In addition, we use the Southern Great Plain (SGP) data to test our cloud parameter inversion algorithm against other algorithms. In addition, we illustrate the need to account for aloft aerosols in observations of aerosol cloud interactions. Finally, we describe how the CCNY site may ultimately be used for further improving ground observations of aerosol cloud interactions.

Acknowledgements

I am sincerely and heartily grateful to my advisor, Barry Gross, for the support and guidance he has provided to me throughout my Ph.D. studies as well as during my dissertation writing. This dissertation would not be possible without his help.

I would also like to thank to Professor Fred Moshary for his guidance and help throughout the years, as well as his inspiration for me to join the remote sensing lab and start the journey 6 years ago.

I was also very fortunate to work with Dr. Andrew Heidinger. Having the opportunity to stay and work with him at Madison in two summers brought my interest in aerosol cloud interactions and related subjects. Although it is more complicated, it is with great challenge and good direction.

I would also like to thank to Professor Jorge Gonzalez and Dr. Mark Arend for being on my committee. Their challenge for my defense and review of dissertation helped me to improve.

I also owe many thanks to colleagues who provided technical support for me to solve problems, to people who provided information resources, to my family and friends who boosted me morally.

Contents

List of Tables

List of Figures

Chapter 1

Introduction

Determining the radiative effects of aerosols is currently one of the most active areas in climate research. Aerosols influence the Earth's radiative balance directly by scattering incoming shortwave radiation back to space, or indirectly through their influence on cloud properties by modifying the optical and microphysical properties of the cloud condensation nuclei (CCN) [Houghton et al., 2001, Twomey, 1977, Rosenfeld, 2006, Lohmann, 2006]. As seen in Figure 1.1, the indirect effect is considered to be one of the largest uncertainties in radiative forcing which drive current global climate models (GCMs). Correctly predicting the indirect radiative effect of aerosols requires that we understand the interactions between aerosols and clouds that determine cloud properties.

There are several indirect ways that aerosols influence the radiative balance of the Earth. The dominant effect and the one which we will focus on in this study is the cloud-albedo effect. For a cloud with a given vertical extent and liquid water content, an increase in aerosol concentration can result in the formation of a larger number of smaller droplets as and a subsequent increase in cloud albedo [Twomey, 1977, Charlson et al., 1992]. Qualita-

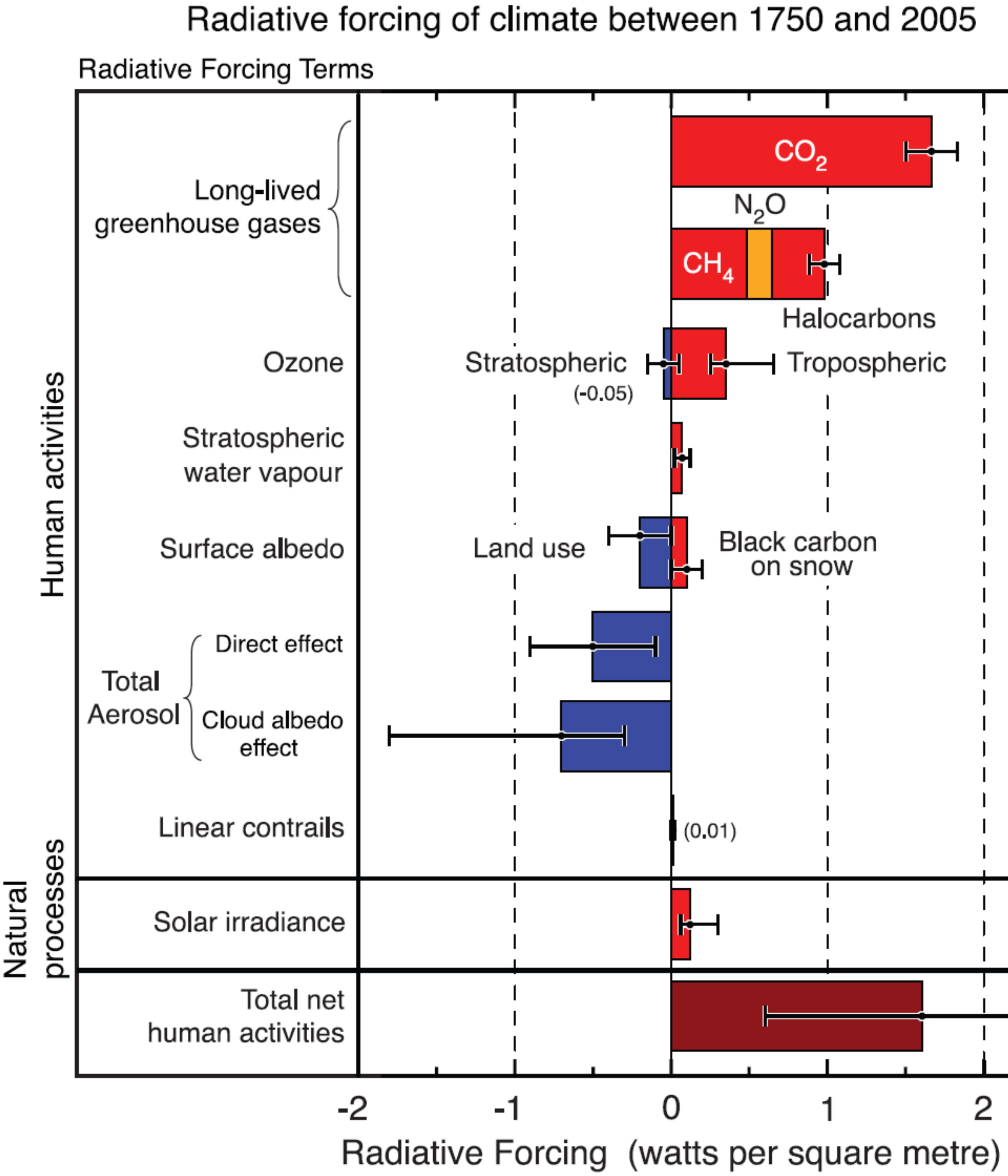

Figure 1.1: Climate forcing values and uncertainties (source: IPCC)

tive confirmation of this process was encountered quite early during the satellite era where observations [Radke et al., 1989] showed bright bands “burned” into the cloud albedo of low clouds in open oceans which were attributed to aerosol emissions from ships and further experiments in marine stratocumulus clouds have confirmed the general mechanism [Ackerman et al., 2000b, Coakley et al., 1987]. Since then, many investigations have been dedicated to investigating the relationship between aerosols and cloud albedo [Nakajima et al., 2001, Hansen et al., 1998, Kaufman et al., 2005, Breon et al., 2002] and their possible climate forcings.

On the other hand, there are other possible aerosol interactions. For example, the second indirect effect, or the Albrecht or cloud lifetime effect [Albrecht, 1989] states that an increase in aerosol concentration increases the cloud life time through reduction of precipitation efficiency due to smaller droplets, leading to increased cloudiness. Another possible mechanism is the so called semi-direct effect by which aerosol absorption in a cloud layer causes clouds to burn off, thereby decreasing their life time and reducing cloudiness [Hansen et al., 1997, Ackerman et al., 2000a].

In general, from these observations, an increase in the ambient aerosol concentrations is expected to increase the cloud albedo unless the cloud is extremely thick. However, it should be emphasized that the albedo effect is not the only mechanism that can lead to an increase in cloud reflectivity. In particular, the cloud reflectance is a function of the total optical depth of the cloud, the single scattering albedo of the droplets, and the particle size distribution which modifies the asymmetry parameter (describing the fraction of energy scattered into the forward direction). An aerosol-cloud interaction that modifies any of these parameters can also affect cloud reflectivity. For example, if the cloud travels through absorbing aerosols such as emissions from biomass-burning or urban pollution, the bulk single scattering albedo will change and decrease the cloud reflectivity [Kaufman et al., 2005]. In addition, the short wave radiation reaching the surface is smaller thereby reducing the water-evaporation cycle needed for cloud formation. This effect (termed a semi-direct effect) counterbalances the cooling effects predicted by the aerosol indirect effects. It is clear that the quantitative assessment of these effects which allow us to connect aerosol changes directly to cloud change can only be performed if detailed information about the aerosol microphysical properties are known.

In probing the aerosol indirect effect, the primary relationship between cloud drop size and aerosol loading is fundamental but cloud drop size is a difficult and error filled measurement. Therefore, other measures of the aerosol indirect effect (AIE) such as the liquid water path (LWP) have also been undertaken. If the AIE mechanism is true, smaller cloud droplets should also lead to a reduction in precipitation and subsequent increase in cloud water path. However, extensive satellite based studies [Han et al., 2002, Matsui et al., 2006, Ackerman et al., 2004] have shown that the relation between aerosol loading and liquid water path is not a simple direct correlation which may be due to complex effects relating to modifications in the evaporation cycle which unfortunately cannot be probed by means of satellite measurements under cloud cover.

1.1 Motivation

It is clear from our discussion that many factors including the meteorology and life cycle of the cloud will affect the radiative properties of clouds and aerosols are only one factor. Therefore, it is vital to quantify separately the meteorological as well as aerosol properties experienced by individual clouds. Such measurements between critical input variables and the cloud radiative properties cannot be done through spatially averaged correlation studies on a regional scale but require a coordinated effort between high temporal resolution satellite imagery and a comprehensive ground measurements below cloud base. These measurements offer the hope of providing relationships between cloud parameters, the local meteorology and aerosol concentration and albedo properties that can help test and refine regional cloud models and parameterizations.

1.2 Outline of the thesis

Chapter 2 of the thesis describes the aerosol-cloud interaction and the mechanisms of cloud formation as well as the role of aerosol in the cloud formation in which the aerosol acts as the CCN. Here, we discuss the current techniques for quantifying the AIE from satellite observation, in particular the polar orbiting satellites. In addition, some of the ambiguities and difficulties are documented to provide a sense of the difficulties involved. This motivates the exploration of complementary approaches and we provide a background discussion of the use of ground based remote sensing techniques which can be used to explore AIE directly.

Chapter 3 presents the satellite retrieval techniques for aerosol properties. While providing an overview of many of the polar orbiting multispectral approaches to aerosol retrieval, we focus on the potential and performance of the GOES geostationary platform to provide aerosol retrievals. For this case, with only a single broadband channel in the visible, we discuss the importance of a realistic aerosol model, in particular aerosol size distribution and the complex refractive index (albedo) to a robust and unbiased retrieval. In particular, seasonal comparisons are made of the GOES retrieved AOD product against AERONET AOD. Here, we show that the best result occurs for the important summer case which we show to be the result of the representativeness of the GOES continental aerosol model with the North East regional model. Finally, we show that the performance is highly degraded for cases where the aerosol is strongly absorbing and develop more appropriate regional models

Chapter 4 describes the performance of GOES satellites to retrieve appropriate cloud properties In particular, the GOES (Visible Infrared Solar-Infrared Split Window Technique) VISST algorithm is presented. In assessing the algorithm, statistical intercomparison between GOES VISST and MODIS cloud retrievals are made which show consistent matchups in COD and Reff with high correlation and minimal bias. To further assess performance of satellite retrievals, matchups during the Intense Observation Period (IOP) field campaign at the DOE ARM site in the Southern Great Plains(SGP) during March 2000 In these intercomparisons, the retrieval of COD and LWP were shown to be more robust than effective radius pointing to probable poor calibration of the old GOES 8 calibration of the IR channel which is most sensitive to Reff. Further comprehensive matchups using different versions and satellites at the SGP site are being made to assess the improvements expected.

Chapter 5 presents our efforts to develop inversion algorithms to process suitable ground-based measurements to quantify aerosol cloud interaction. The focus here is on developing an iterative retrieval algorithm using Microwave Radiometer (MWR) and Multifilter Rotating Shadowband Radiometer (MFRSR) measurements which is available at CCNY to simultaneously retrieve COD and Reff. The performance of our iterative algorithm was assessed against a number of existing algorithms and approaches. In these comparisons, the strong impact of the integrated LWP are shown to be the most important. In this direction, we point out that the standard 2 channel MWR is not optimal and show that the use of a more sophisticated multispectral MWR including high frequency channels > 50 GHz can reduce errors. In making this claim, we resort to intercomparisons of integrated water vapor between the 2 channel radiometer and CCNY's Microwave radiometer against AERONET and radiosonde profile. In assessing the errors that can be attributed to the ground retrieval, a statistical uncertainty analysis is made to quantify the expected errors that can result from variability in the underlying aerosol loading below cloud based on aerosol climatologies from AERONET, the uncertainty in the surface albedo at 415nm and the measurement uncertainty attributed to estimated errors in LWP and the diffuse transmittance due to imprecise calibration errors. Here, the improvement that may be gained with a more advanced radiometer is quantified. Finally, A case study of AIE effects is given for the SGP site. One interesting feature we bring out is the importance of using simultaneous lidar to quantify aloft aerosols in better observing AIE.

Since the aerosol variability in CCNY in comparison to the SGP makes this site an attractive place for studying AIE, Chapter 6 discusses the progress and future directions in developing the CCNY testbed suite to quantify AIE. Here, preliminary performance of cloud properties is assessed against GOES retrievals and most of the biases seen are removed. Furthermore, we further discuss the development of novel instrumentation in this effort including first assessments of a coherent wind doppler lidar.

Chapter 2

Aerosol-cloud interactions

Aerosol and clouds are strongly coupled to each other making their effect on the Earth's energy balance extremely difficult to quantify. This coupling works in both directions. For example, the impact of atmospheric aerosol on cloud properties, such as the size of the cloud droplets and subsequent radiation scattering properties of the cloud droplet, has been confirmed in a number of studies [IPCC, 2001, Ackerman et al., 2000a, Houghton et al., 2001]. On the other hand, clouds and precipitation can wash away aerosols in the atmosphere thereby changing both the size distribution and chemical components of the aerosol, as well as the chemical properties of the clouds. Recent studies also indicate that clouds can be involve in the nucleation process of new aerosols. Clearly, this complex coupling is very difficult to isolate. To make things manageable, we therefore limit the main focus of our study to possible anthropogenic aerosol effects on clouds. This choice is motivated by the accessibility of these processes to measurements by remote sensing approaches as well as a particular interest in studying the impact of anthropogenic sources such as those which can occur in a metropolitan area such as New York.

2.1 Aerosol indirect effects

Clouds can scatter the incoming solar radiation back to space. Thus, in general, it results in cooling force on the climate. On the other hand, atmospheric aerosols also play an important role in affecting the climate through modification of the microphysical properties of the cloud droplets and thus affecting the cloud formation process. Aerosols, especially the water soluble particles, can act as the cloud condensation nuclei (CCN). Thus, the number of cloud droplets formed depends on the number of the CCN, which is determined by the chemical composition and the size of the aerosol particles. The size of the cloud droplets is also determined by the size of the aerosols forming the CCN. The clouds consisting of more numerous but smaller droplets have higher reflection. Also, if the sizes of the cloud droplets are small, the time to form precipitation clouds by collision-coalescence process might take longer time compared to large cloud droplets. Thus, the time of the clouds lives longer. The long-living clouds would reflect more incoming solar radiation back to the space, thus it has cooling effect on the climate. This process is called *Twomey Indirect Effect* [Twomey, 1977].

2.2 Cloud droplet activation

Cloud droplets form in the atmosphere by condensation of supersaturated water vapor on aerosol particles. Those particles that have the potential to nucleate liquid cloud droplets are called cloud condensation nuclei (CCN).

In order to understand the aerosol effect on clouds, we need to understand the process of cloud droplet activation in the atmosphere. In Earth's atmosphere, the cloud droplets can not form by homogeneous nucleation of supersaturated water vapor. In homogeneous nucleation process, the water molecules need to spontaneous collide and subsequently stick together, thus eventually grow into cloud droplets. However, the supersaturation required for homogeneous nucleation process is several hundreds of percentage, which does not occur in the natural atmosphere. On the contrary, the heterogeneous nucleation process only requires the supersaturation at a relative low percentage. In the heterogeneous nucleation process, the presence of aerosol particles greatly facilitates the condensation of water vapor grow into droplets ranging from several micrometers to tens of micrometers in diameter.

The process in which water vapor condenses and form liquid droplets is described by Kohler theory, which is based on equilibrium thermodynamics. It combined the "Kelvin effect" and "Raoult's law". Kelvin effect shows that the equilibrium vapor pressure over a strongly curved surface is much greater than that over a flat surface. Raoult's law shows that the equilibrium water vapor pressure over a solution is lower than that over pure water. In the subsection 2.2.1, the equilibrium behavior of pure water drops in a water vapor field is discussed. The section 2.2.2 discusses that of the solution droplets in a wate vapor field.

2.2.1 Kelvin effect

The Kelvin equation describes the change in the equilibrium vapor pressure due to a curved liquid/vapor interface with radius r. If in the system the temperature and total air pressure are held constant, the variation of water vapor pressure with the radius of the drop is expressed by

$$\frac{p_{r,\omega}}{p_{sat,\omega}} = exp\left(\frac{2M_\omega\sigma_{\omega/r}}{RT\rho_\omega r}\right) \tag{2.1}$$

where $p_{r,\omega}$ is the actual water vapor pressure over the droplet surface, $p_{sat,\omega}$ is the saturated water vapor pressure, M_ω is the molecular weight of water, $\sigma_{\omega/r}$ is the surface tension of water with respect to air, r is the radius of the water drop, R is the universal gas constant, T is the temperature, and ρ_ω is the density of water. It shows that equilibrium vapor pressure depends on droplet size. If $p_{r,\omega} < p_{sat,\omega}$, the water evaporates from the droplets. If $p_{r,\omega} > p_{sat,\omega}$, the water vapor condenses onto the droplets, therefore, increases the droplets volumes. As r increases, $p_{sat,\omega}$ decreases and the droplets grow into bulk liquid. Vice versa, if the radius of the drop is small, the saturation vapor pressure needs to increase exponentially, which shows that the saturation vapor pressure over the surface of a water drop is much larger than that over a flat surface.

Various experiments have been attempted to validate the theory [Shereshefsky and Steckler, 1936, Pruppacher and Klett, 1998]. It was found by [Wilson, 1900] that saturation ration in air free of all ions and impurities can reach a relative humidity of 800% before a water droplet forms in an expansion chamber.

2.2.2 Solution drops

Since Raoult law opposes the Kelvin effect, Kohler theory describes that for each dry soluble particle size there is a "critical supersaturation", S_c, at which the difference between the Raoult and Kelvin effect is at a maximum. Kohler theory predicts that S_c decreases with increasing size of a soluble particle, or with increasing mass of a soluble substance contained in a mixed particle containing both soluble and insoluble components [Pruppacher and Klett, 1998, Seinfeld and Pandis, 1998].

Kohler equation describes the ration of actual saturation vapor pressure e (in equilibrium over a solution with a curved surface), to vapor pressure over a flat pure water surface. It can be expressed by

$$\frac{e}{e_s} = \frac{exp\left(\frac{c_1}{TR}\right)}{1 + \frac{c_2 i m_s}{M_s R^3}} \tag{2.2}$$

where T is the absolute temperature, R is the droplet radius, i is the number of ions per molecule in solution, m_s is the mass of solute in the droplet, M_s is the molecular weight of solute, c_1 and c_2 are constant. $c_1 = 0.3335 K\mu m$, $c_2 = 4.3X10^{12}\mu m^3 g^{-1}$.

Figure 2.1 shows the Kohler curve calculated for dust particles containing small amount of K^+, Mg^{2+}, or Ca^{2+} compounds [Kelly et al., 2007]. From the Kohler curve, we can see that for a particular relative humidity, for a particle with large radii, the droplet will grow. But for a particle with small radii, the droplet will shrink. If the relative humidity becomes greater than the peak of the Kohler curve, the droplet can grow unimpeded. We can also see that on the left of the Kohler curve peak, small CCN grows into small droplet that stop growing at equilibrium stat of humidity, temperature, and solute. The common phenomenon is wet haze droplets and smog. But on the right of the Kohler curve peak, CCN is activated and continues to grow as long as water vapor is available. This process generates the cloud droplets. The radius of the droplet where the critical point occurs (i.e. whether it will grow-be activated or reach equilibrium and remain small) is given by

$$R = \sqrt{\frac{c_3 i m_s T}{M_s}} \tag{2.3}$$

where $c_3 = 3.868X10^{13}\mu m^2/Kg$, i is the number of ions per molecule in solution, M_s is the molecular weight of solute, T is the temperature.

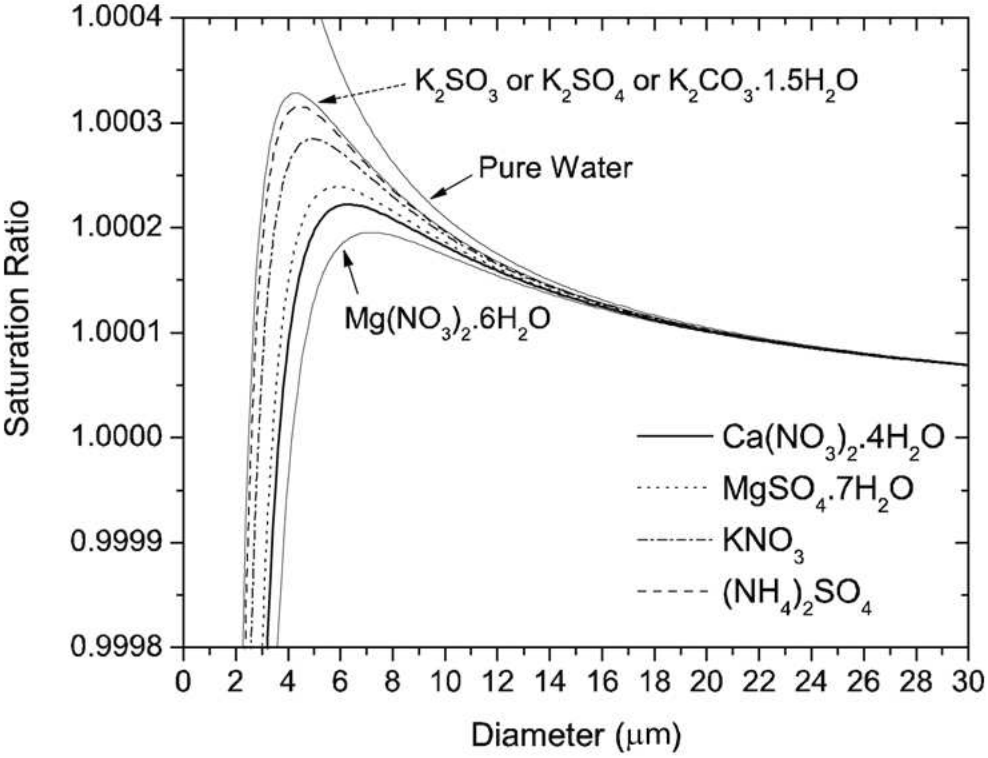

Figure 2.1: Kohler curves for particles having a 0.79 μm SiO_2 core coated with highly soluble conpond. [Kelly et al., 2007]

2.2.3 Time Variation

From previous discussion, it is quite clear that both size and chemical composition affect the ability of aerosol particles to become CCN, therefore greatly affect the cloud formation process. However, the kinetics of cloud droplet activation is not only limited to variation in aerosol size and chemical composition. Due to the local environment including the cloud height and vertical wind uptake, the cloud droplet curves can change dynamically from point to point.

The attempt to model the kinetics of condensation and evaporation of a droplet started about 100 years ago. The well-known Maxwell equation [Maxwell, 1890] describes the dynamics of the droplet with assumption that continuity of vapor and temperature fields at the surface of a wet-bulb thermometer. This assumption is valid for large growing or evaporating droplets under stationary conditions. Maxwell's equation has been widely used in cloud physics. But for the growth of a small droplet, the equation cannot describe the rate of the growth and evaporation well. [Fukuta and Walter, 1970] derived equations taking all of the factors into consideration except heat transfer by radiation.

For a solution droplet the equation is

$$\frac{dm}{dt} = 4\pi r_s^{'}(S - A)/\left(\frac{ALL'M}{KRT^2_{infty} f_\alpha} + \frac{1}{D_{\rho\infty,sat} f_\beta}\right) \tag{2.4}$$

where

$$A = \frac{n}{n + in'} exp\left(\frac{2\sigma' V_L'}{r_s' R T_\infty}\right) \tag{2.5}$$

where m is the mass of droplet, K is the thermal conductivity of air, L is the latent heat of condensation of water vapor, L' is the latent heat of condensation of water vapor in solution, M is the molecular weight of water, f_α is the correction factor for temperature difference, f_β is the correction factor for vapor density difference, r_s is the droplet radius, S is the saturation ratio, T is the temperature, D is the diffuse coefficient of water vapor in air.

The model based on equation 2.4 can calculate the growth of droplet with time [Schwartz, 2000]. Although the calculation is quite idealized, the result is still quite informative. The calculation takes a distribution of droplets and then integrates this equation for a given wind updraft velocity, which translates into a cool rate, which translates into a rate of generating

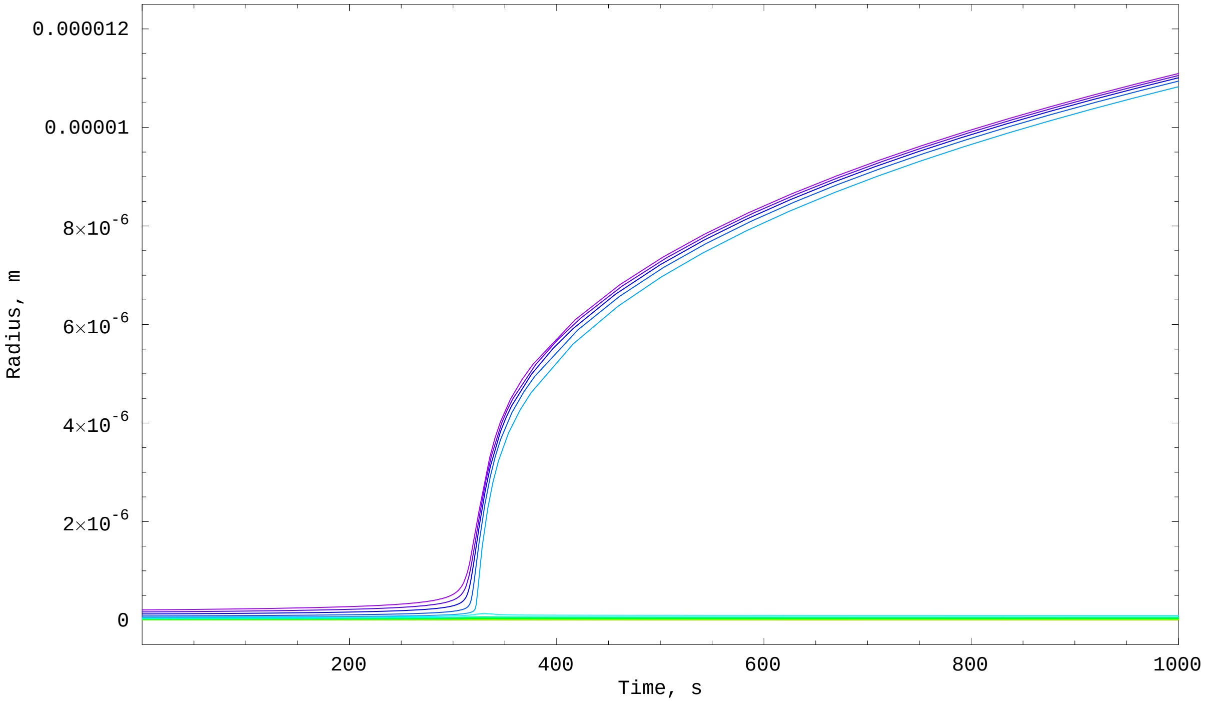

Figure 2.2: The growth of droplet size with time. [Schwartz, 2000].

supersaturation. Basically, a time varying uptake moves the aerosol particle upwards resulting ion a cooling temperature which causes the super saturation to increase with time so that $S = S(t)$. So as $S(T)$ goes from a subsaturation value (.9) to a supersaturation ($S > 1$) the system grows fast.

Figure 2.2 illustrate the growth of the droplet. When we zoom in the activation region shown in Figure 2.3, we can see the sharp separation of activated and inactived particles.

It is also worth noticing that the activation of drop occurs within hundreds of seconds. It is clear that to observe this process, we need to use a fast measurement, which can provide sufficient sampling information to quantify the aerosol effect on clouds. More details are discussed in 2.3.2.

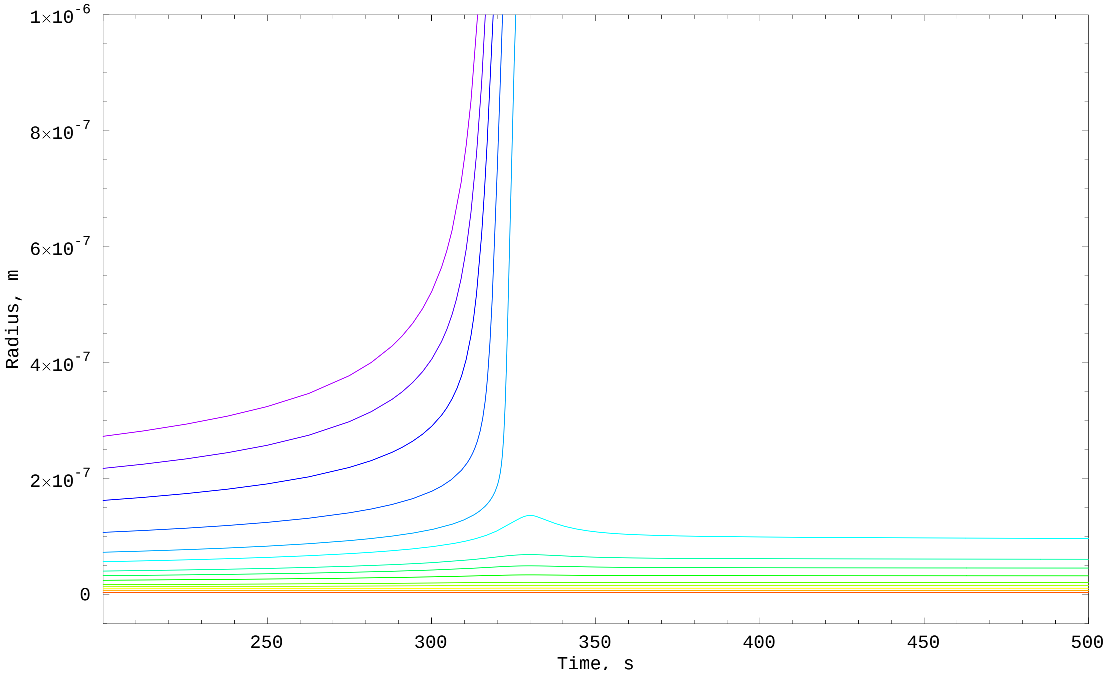

Figure 2.3: Zoom in the growth of droplet size with time. [Schwartz, 2000].

2.3 Quantification of aerosol-cloud interaction

2.3.1 Satellite approaches

Unlike direct cloud effects on the climate, the aerosol-cloud interactions are very hard to measure from satellites directly since simultaneous measurement of aerosol loadings (especially below cloud base) and cloud properties such as COD / Reff are not possible and therefore efforts at quantifying these effects are limited to statistical trend studied over large domains. However, because of the difficulties in more direct approaches, extensive satellite studies of aerosol cloud indirect effect have been pursued aided by significant improvement in multispectral satellite sensors onboard polar orbiting satellites.

For example, extensive regional measurements and resultant cloud products from MODIS

(MODerate resolution Imaging Spectroradiometer) were used [Myhre et al., 2007] together with aerosol properties estimated from the MODIS aerosol optical depth product to ascertain statistical relationships between appropriate aerosol and cloud parameters which include Cloud Top Temperature and Pressure, Cloud Droplet Number Concentration, Total Cloud Fraction, Water Path, Cloud Effective Radius, Cloud Optical Thickness, Cloud Condensation Nuclei and Aerosol Optical Thickness. In this study, it was found that on average, large regions are laden with fluctuating correlations between cloud and aerosol metrics which average to zero as might be expected. However, by appropriate binning of the data by LWP and with ancillary data provided by ISCCP data (International Satellite Cloud Climatology Project) to ascertain regions of dominant cloud type (stratus or convective clouds), an inverse relationship between the size of the water droplet (effective radius) and column cloud droplet number concentration cloud optical thickness (reflectivity) and cloud fraction emerged. These relationships were connected to the aerosol properties through an observed inverse correlation between aerosols and droplet radius in support of the general AIE effect.

However, the story is not so clear cut. For example, if the AIE is occurring, there should be a positive correlation between aerosol optical thickness and water path. However, analysis of the data showed significant differences between low AOT ($\tau < 0.1$) and higher AOT ($\tau > 0.1$). In particular, for low AOT, a strong positive correlation was observed but for high AOT, a strong negative correlation between aerosols and water path was observed. Further studies show even more complex behavior. For example [Han et al., 2002], the results of a global survey for warm water clouds (cloud-top temperature > 273 K, optical thickness $1 < \tau < 15$) revealed three distinct relations between cloud liquid water path with aerosol changes: increasing, approximately constant, or decreasing as cloud column number concentration increases, each occurring with nearly equal probability. The negative correlation may result from the mechanism that an increase of cloud droplet number concentration with subsequent reduction in cloud droplet size can enhance evaporation just below cloud base. In this scenario, the cloud decouples from the boundary layer in warmer locations, decreasing the supply of water to the cloud from the surface thereby reducing the cloud liquid water. We have seen contradictory results attempted to relate the liquid water path to aerosol properties. [Sekiguchi et al., 2003] study shows a positive correlation between the AVHRR water path and the column CCN on the global scale whereas [Matsui et al., 2006] show a negative correlation. [Han et al., 2002] identify that the correlation between these parameters may be positive or negative and varies regionally while the results of [Kaufman et al., 2005] suggest that the sign of the response may depend on aerosol type. Even with a given region of cloud type, evidence from both remote sensing [Coakley Jr. and Walsh, 2002] and in situ [Ackerman et al., 2000b] analyses indicate that the liquid water response of individual clouds may be either positive or negative. Furthermore, modeling studies [Ackerman et al., 2004, Wang et al., 2003] frequently demonstrate decreases in cloud water path resulting from increased entrainment of subsaturated air leading to increased droplet evaporation. [Jiang et al., 2006] modeling study suggests that CCN concentrations may not significantly effect cloud lifetime or the cloud fraction.

Despite the fact that the ambiguity in quantify the aerosol indirect effect, the poor temporal statistics makes it difficult to establish true correlations, while such statistical studies have provided useful information. Recently, however, suitable multispectral imagers on geostationary (GOES) platforms have been developed. In particular, the availability of additional spectral channels at 1.6, 3.9, and 12 or 13.3 μm in addition to the original VIS (0.65 μm) and IR (10.8μm) channels has led to operational retrieval of optical depth, effective radius and LWP and motivates the possibility of following the cloud through its lifecycle as it is transported in polluted areas [Palikona et al., 2006]. The characterization of the cloud diurnal cycle is potentially feasible with geostationary satellite instruments but will require data fusion between these instruments and more accurate measurements from polar satellites for cross-calibration.

Further, it is important to realize that beyond the problems associated with the statistical nature of the data, an equally difficult issue is retrieving a true aerosol loading near cloud base. In particular, it is quite evident that column measures of aerosol optical depth do not provide the vertical information needed to quantify the pollution level at cloud base. In addition, the relationship between optical depth and particle number depends on the microphysical distribution models and does not discriminate between aerosol types below cloud base, that impact cloud microphysics, and aerosol particles located higher than cloud top, that only interact with the radiative transfer above clouds. Therefore, the need for short term measurements with high temporal resolution is needed to eliminate many of the above cited ambiguities. In particular, simultaneous measurements of clouds and aerosol loading are achievable and the exact nature of the cloud within the cloud lifecycle is not relevant on these short term measurements.

2.3.2 Ground based approaches

Various efforts have been made to develop retrieval algorithms to infer cloud optical depth and effective radius from ground based passive radiometric measurements. In one approach, a Microwave Radiometer is combined with Millimeter Wave Cloud Radar (MWCR) to infer droplet diameters. In this case, the radar reflectivity and the MWR LWP provide the information to retrieve Reff [Frisch et al., 1998]. However, the cost of the MWCR in particular makes this method very unattractive. On the other hand, significant success in combining Cloud Optical Depth from the Multifilter Rotating Shadowband Radiometer (MFRSR) together with the LWP from a MWR is a reasonable cost effective solution [Leontieva and Stamnes, 1994, Min and Harrison, 1996a]. One drawback in this method is obviously the limitation that observations must be made during daytime but it is expected that the largest aerosol cloud interaction signals occur in daytime when convective heating enhances vertical winds [Han and Baik, 2009] making this restriction palatable.

In particular, a number of studied have made the attempt to explore Aerosol Cloud Interaction at the SGP site using the available instrument suites. For example, the MWCR / MWR technique was applied [Feingold et al., 2003] to explore a number of potential cases together with a raman lidar which was used to estimate aerosol CCN below the cloud. This study did in fact find a number of cases which showed reasonable AIE effects. In particular, defining the Aerosol Cloud Index (ACI) as

$$ACI = -\left(\frac{dlogR_{eff}}{dlog(\alpha)}\right)_{LWP} \tag{2.6}$$

values of ACI $\sim .1$ were found for multiple cases over the multiyear datasets which is reasonable considering the upper theoretical limit ACI $< 1/3$

However, one of the main purposes is to avoid the use of the MWCR and explore the potential of the MFRSR / MWR retrieval. For example, [Kim et al., 2003] made use of this approach to explore potential aerosol-cloud modifications. Unlike the Feingold study however, they did not make use of the lidar extinction being content to use surface nephelometer measurements instead. This approach seems to be sufficient if the cloud base is sufficiently low to the surface, which in fact holds for most examples considered. However, it was noted in their study that some examples did not satisfy this requirement and that the poor results on these days are in fact due to a decoupling of the surface aerosol to aloft aerosols. In fact, we illustrate that the coupling of the surface is usually limited to < 500 meters and the use of aloft lidar is significant in demonstrating such effects.

Due to the lack of current long term data at the NYC CCNY site, we content ourselves at present to testing and demonstrating this approach using the multi-year measurements performed at the Southern Great Plains (SGP) site of the Atmospheric Radiation Measurement (ARM) Program. In addition, we make use of the filtering accomplished by previous studies to identify optimal cases. After we have demonstrated the data processing on the SFGP site, we will provide preliminary assessment of the CCNY site progress.

Chapter 3

Aerosol retrievals from satellite

Quantification of the aerosol properties, in particular aerosol optical depth (AOD), has become one of the fundamental information needed for studying the aerosol cloud interaction. Satellite observations have the ability to provide global coverage of the aerosol monitoring, which cannot be achieved by any other type of instruments (such as ground or *in situ* instruments). However, it has been well known that accurate aerosol retrieval from satellite observations has difficulties over land, especially in the urban area, due to the bright surface contamination. Our focus of the study is on aerosol retrieval by geostationary operational environmental satellite (GOES) because its high temporal resolution gives much more statistical information than polar orbiting satellites.

In this chapter, we explore the potential of GOES aerosol retrieval in studying the aerosol cloud interaction. The current aerosol retrieval techniques by polar orbiting satellites are discussed in section 3.1. The current operational GOES aerosol and smoke product (GASP) algorithm is presented in section 3.2. In section 3.3, we continue the results of the assessment of the current GASP against AErosol RObotic NETwork (AERONET) AOD retrievals. In section 3.4, the aerosol models are analyzed. Then, the conclusion of the performance of GASP is given in section 3.5.

3.1 Current satellite aerosol retrieval techniques

The AOD retrieval algorithm is basically the inversion algorithm that extracts the AOD from the top of atmosphere (TOA) measurements by satellite. Therefore, the knowledge of the atmospheric radiative transfer (RT) mode is needed. In AOD retrieval problem, the RT model is the mathematical (or numerical) estimation of the TOA reflection measurement, calculated based on the light interacted with the medium, given the underlying aerosol properties. Once the RT model is known, the inversion problem becomes to seek the aerosol properties which best fit the measurement.

The simplest way to solve the AOD retrieval problem is to use brute force method. It evaluates all possible fittings of the aerosol properties. However, the disadvantage of the brute force method is quite apparent. Each evaluation of the possible aerosol properties takes time. When large amount of data needs to be processed, this method becomes very time consuming.

The alternative way to solve the inversion problem, which is commonly found in the satellite community, is to use look up table (LUT) approach. The LUT is a pre-calculated vector or associated arrays based on RT model with given parameters in selected values. It replaces the run time computation with interpretation with a simpler array indexing operation, therefore, reducing the time consumption in the AOD retrieval process.

3.1.1 The general approach of aerosol retrieval algorithm

The AOD retrieval algorithm is also heavily dependent on the sensor's characteristics. Different sensors have different capabilities. The spectral and angular information vary from one satellite instrument to another. The multispectral sensors can provide the information of fine mode aerosol properties at short wavelengths (UV, VIS), and the information of the coarse mode aerosol properties at longer wavelength (NIR). The multi-angle sensors can provide angular information of aerosol scattering, which depends on the particles microphysical properties (size, shape, and refractive index). The sensors with polarization measurements can measure the polarized intensity besides the total intensity of light. The combination of the measurement in multi wavelengths and multi angles along with total intensity and polarized intensity makes the aerosol properties retrieval feasible [Mishchenko and Travis, 1997a,b]. However, most sensors do not have the capabilities to provide the measurements containing all spectral, angular, and polarized intensity information. Thus, in order to compensate the restricted information content, the aerosol retrieval algorithms have to rely on a-priori assumptions. The use of the assumptions could lead to uncertainties in retrieved aerosol properties, which could propagate errors in in the estimation of aerosol impact on climate.

The satellite aerosol retrieval algorithm in general consists of three important pieces of processes. It must be able to quantify the surface contribution, which is called surface correction. It also needs to be able to remove the atmospheric effects, such as gas absorption, as well. This process is referred to as atmospheric correction. In addition, all aerosol retrieval algorithms require accurate and robust cloud screening procedures. The reason for these processes is that the solar reflection signal collected by the satellite sensors consists of photons that either directly interact with surface or interact with the atmosphere. Those photons are essentially indistinguishable.

Table 3.1 presents the summary of the characteristics and aerosol products of current operational aerosol retrieval satellite instruments.

3.1.2 Advanced Very High Resolution Radiometer (AVHRR) approach

The current AVHRR is a radiometer on board of NOAA's Polar Operational Environmental Satellite (POSE). It only uses a single visible channel at 0.63 μm to retrieve AOD. It only measures the total intensity of light along a fixed view angle. Apparently, AVHRR's aerosol retrieval algorithm is far from optimal. Because of the limitation of the sensor's capability, the aerosol model must be decided a-priori based on historical climatology data sets [Knapp, 2002a, Stowe et al., 2002, Hauser et al., 2005b,a]. The retrieval algorithm only provides rough estimation of AOD over ocean [Husar et al., 1997, Ignatov and Stowe, 2002]. But it should be kept in mind that the long time series data makes AVHRR AOD processing very useful as a long term climate or environmental data record (CDR or EDR) particularly over the ocean where the aerosol variability is less and the ocean surface is accurately estimated as dark. The same is true for AOD product from the Total Ozone Mapping Spectrometer (TOMS), which is retrieved above both land and ocean [Torres et al., 2002] with limited accuracy.

Table 3.1: Satellite instruments for aerosol retrievals

Satellite Instruments	AVHRR (Multiple)	MISR (Terra)	MODIS (Terra/Aqua)	POLDER (PARASOL)	GOES (EAST/WEST)
Launch	May 1981	Dec 1999	Dec 1999 / May 2002	Dec 2004	Oct 1975
Spectral bands	5 bands (0.63 to 11.5 μm)	4 bands (0.47 to 0.86 μm)	12 bands (0.41 to 2.1 μm)	8 bands (0.44 to 0.91 μm)	VIS band
Viewing angles	1	9	1	Multiple	1
Polarization measurement	No	No	No	Yes	No
Average revisit time	1 day	9 days	1 to 2 days	1 day	30 minutes
Aerosol products	AOD	AOD, Ångstrom exponent	AOD	AOD, Ångstrom exponent	AOD

3.1.3 Multi-angle Imaging Spectro-Radiometer (MISR) approach

Since aerosols have rich angular dependent scattering behavior, it is reasonable to believe that multi-angle observations can improve aerosol retrieval. MISR observes the Earth on board of the polar-orbiting Terra platform (on the same platform with the MODIS-Terra) at altitude of 750 km. It measures the total intensity of TOA radiance by using nine cameras which are paired (fore / aft) in a symmetrical arrangement and acquire multispectral images with fixed view angles at 0^o, 26.1^o, 45.6^o, 60.0^o and 70.5^o. Each camera is fixed at a particular view zenith angle in the along-track direction and has four spectral bands (446, 558, 672 and 866 nm). A cross-track ground spatial resolution is 275 m (in all nine cameras in 672 nm and the nadirs camera in 446, 558 and 866 nm) or 1.1 km (remaining eight cameras in 446, 558 and 866 nm) in global mode (operational mode). However, in local mode, 275 m spatial resolution in all 36 channels (nine cameras in four wavelengths) can be achieved [Diner].

The objective of the MISR aerosol retrieval algorithm is to take advantage of both the multi-spectral and multi-angle viewing capability to separate scattering radiance from atmosphere and underlying surface without a priori knowledge of the land surface type. In the current version of the retrieval algorithm, two steps are included. The first step is based on the principal components analysis of multi-spectral and multi-angle TOA MISR data from which empirical orthogonal functions (EOFs) for each wavelength for all camera angles were obtained to describe the directional reflectance properties of the surface [Martonchik et al., 1998, 2009]. The second step was implemented into the processing chain after 3 years of operation [Diner et al., 2005] and makes use of the fact that the bulk of the angular reflectance dependence at TOA is dominated by the surface angular reflectance.

MISR retrieves the AOD above the ocean [Kahn et al., 2001] and land, including bright surfaces, like deserts [Martonchik et al., 2004]. It also provides an estimation of the Ångstrom exponent, as well. Furthermore, its multi-angle capabilities introduce the possibility of determining the height of plumes by looking at complex spatial patterns in multi-angle configurations providing a stereo-projection approach, which, however, clearly dissipates away from the emission source [Kahn et al., 2001].

3.1.4 Moderate Resolution Imaging Spectro-Radiometer (MODIS) approach

MODIS is the current workhorse in the aerosol community. Flying on both Terra (EOS AM) and Aqua (EOS PM), they combine to view the entire Earth's surface every 1 to 2 days with a repeating orbit every 16 days and wide 2330 km swath. MODIS has 36 spectral bands (from 0.4 to 14.4 μm) with nadir on-ground spatial resolution of 1,000, 500, and 250 meters.

Historically, the MODIS algorithm for AOD retrieval over land required "dark" pixels as described in the Collection 4 (C004) algorithm [Kaufman et al., 1997, Kaufman and Tanre, 1998]. Since many land covers such as vegetation and some soils have very low surface reflectance in the red (0.66 μm) and blue (0.47 μm) wavelengths, it is reasonable to use the darkest pixels in the image to explore the aerosol optical properties. For example, dense dark vegetation in an image can be considered as "dark" pixel and the aerosol contribution can be isolated. Isolation of dark targets in the aerosol retrieval algorithm [Kaufman and Sendra, 1988] was based on the detection of green forests as dark pixels based on a high Normalized Difference Vegetation Index (NDVI).

Still, even moderately dark vegetation scenes have a residual reflectance that cannot be realistically ignored unless the aerosol optical depth is high, and this is even more so for urban scenes. For this reason, some estimate of the ground reflectance is essential and this estimate relies heavily on MODIS having a channel in the NIR (2120 nm) that can see the ground without atmospheric contamination. In C004, an empirical relationship derived from Landsat observations of vegetation for the SRR's were used In C005, significant progress in improving these relations was made based on global matchups between AERONET and MODIS [Levy et al., 2007a]. In particular, having AERONET provide local aerosol properties made it possible to directly retrieve surface reflections at the VIS and SWIR bands simultaneously. From this, it was possible to obtain relevant SRR's as a function of geometry (parameterized by the scattering angle) and land surface type defined by a so-called Modified Vegetation Index (MVI). This MVI uses bands 1240 and 2120 nm as opposed to the standard NDVI index which uses 670 and 860 nm to avoid atmospheric contamination in land type classification.

The operational MODIS aerosol retrieval algorithm over land is based on a LUT approach, i.e., radiative transfer calculations of TOA reflectance are pre-computed for a set of aerosol models. These include four fine modes (Continental, Generic, Absorbing smoke and Non-absorbing urban) and one coarse mode (non-spherical Dust). Details of the microphysical properties of these modes can be found in Levy et al [2007a]. The calculations are performed with the RT3 code developed by Evans and Stephens [Evans and Stephens, 1991] at four discrete wavelengths (0.466, 0.553, 0.644 and 2.12 μm, representing MODIS channels 3, 4, 1 and 7, respectively) for seven aerosol loadings ($\tau_{0.55\mu m}$ =0.0, 0.25, 0.5, 1.0, 2.0 3.0, and 5.0), and 9 solar zenith angles (θ_s = 0.0, 6.0, 12.0, 24.0, 35.2, 48.0, 54.0, 60.0 and 66.0), 16 sensor zenith angles (θ_v = 0.0 to 66.0 with increments of 6.0) and 16 relative azimuth angles ($\delta\phi$= 0.0^o to 180.0^o with increments of 12.0^o). Aerosol phase functions are calculated either using MIEV code [Wiscombe, 1981] for spherical assumption or a version of the T-matrix code for spheroid dust described in [Dubovik et al., 2006]. Because the MODIS over-land retrieval algorithm employs only three channels, there is insufficient information content to independently choose or retrieve the fine aerosol model [Remer et al., 2005]. Therefore, the MODIS aerosol retrieval algorithm must assign the fine aerosol model a priori of the retrieval based on season and location from a global aerosol models obtained from AERONET [Remer et al., 2005, Levy et al., 2007a,b].

To summarize, the algorithm performs a simultaneous retrieval over the parameter space whose variables are the AOD at 0.55 μm, the surface reflectance at 2.12 μm and the mixing fraction η using the three spectral channels (0.47, 0.660 and 2.12 μm). However, the operational algorithm is still less than optimum over urban areas. Unlike MISR, the aerosol retrievals are often over biased in selected urban areas and, as we will see, this is a direct consequence of the surface albedo estimates MODIS uses in the visible channels.

Finally, it is also of interest to note that the same basic algorithm structure is being applied to Visible/Infrared Imager/Radiometer Suite (VIIRS) as part of the National Polar-Orbiting Operational Environmental Satellite System (NPOESS) with AOD, angstrom coefficient and effective radius parameters being reported at 6 km Nadir resolution. However, an effort has been made to improve on the range of surface types where the SRR's using extensive Landsat atmospherically corrected training sets over diverse terrain. Updated relations between the VIS and SWIR ground reflections as function of the NDVI have been developed and further training to connect the shape of the directional reflectance to NDVI and thereby account for non-Lambertian surface reflection has been incorporated [VIIRS, 2010]. However, the surface model is designed only for vegetated and semi-vegetated surface types and overly bright pixels based on threshold tests on TOA reflectance of the 1240 nm and 2120 nm channels will be flagged so VIIRS retrieval into urban domains is not expected within the VIIRS operational retrieval.

3.1.5 POLorization and Directionality of the Earth's Reflectances (POLDER) approach

The POLDER radiometer provides multispectral, polarized measurements at multiple angles [Deschamps et al., 1994]. The POLDER 1 instrument was launched on the ADEOS Japanese platform in August 1996 and the third version of POLDER is flying in the A-Train on board the PARASOL (Polarization and Anisotropy of Reflectance for Atmospheric Sciences coupled with Observations from a Lidar) platform since December 2004. POLDER provides quantitative global measurements of total as well as polarized solar radiation reflected by the Earth-atmosphere system including multi-angle (up to 16 directions due to the wide FOV CCD imaging plane) data at eight spectral bands in the visible and near-infrared spectral domain (0.443 to 1.02 μm).

The value of this approach resides in the fact that the polarization of the reflected signal from the surface is significantly lower than the polarization of the signal scattered by fine mode aerosol in the atmosphere. Therefore, the relative contribution of the polarized ground reflectance to the TOA polarized reflectance is small and stable enough to determine with semi-empirical surface BPDF models [Herman et al., 1997, Deuzé et al., 2001] obtained from fitting clear sky surface retrievals. On the other hand, for dust aerosols, POLDER cannot separate atmosphere and surface signal very well since the coarse aerosols produce little polarization in atmospheric scattering. Therefore, POLDER retrieval focuses on the fine aerosol mode and the retrieval algorithm assumes only spherical scattering, which is valid for fine aerosols. Even though the POLDER retrieval algorithm shows is less effective for coarse mode aerosol, the retrieval method is still a very useful method for aerosol over land since most of the aerosol generated by pollution and biomasses burning are fine mode [Deuzé et al., 2001] providing excellent views of anthropogenic emissions.

In the retrieval algorithm, the aerosol optical depth and model is obtained by matching the precomputed LUT to the multi-directional polarized reflectance measurements at 670 and 865 nm. The aerosol retrieval algorithm considers only fine particles to compute LUT sampling the lognormal distribution range from 0.05 to 0.15 μm in ten modal radii rm with a fixed standard deviation of 0.403 and a refractive index of m=1.47-0.01i. To simplify the model, POLDER retrievals only consider the polarized light corresponding to single scattering by aerosols, single scattering by molecules, and direct reflection on the surface. Similarly, the BPDF (Bidirectional Polarized Distribution Function) from the surface are modeled by assuming that the polarized light comes from specular reflection on surface elements. The assessment of polarized reflectance is based on a priori values (as a function of observation geometry and surface type) derived from a statistical analysis of POLDER data [Nadal and Bréon, 1999]. More details can be found at [Deuzé et al., 2001].

Given the 2N (two wavelengths, N-viewing directions) measurements, for each aerosol model, the residual error ε,

$$\varepsilon = \sqrt{\frac{1}{2N}\sum_{\lambda}\sum_{j}[Q_{cal}(\lambda, \Phi_j) - Q_{meas}(\lambda, \Phi_j)]^2} \tag{3.1}$$

is calculated where Q_{cal} and Q_{meas} are the calculated and measured polarized intensity respectively. The retrieved aerosol parameters are the Angstrom exponent α and optical thickness τ_{670nm} corresponding to the model which gives the smallest residual error ε.

However, several points must be emphasized that make POLDER measurements quite difficult for aerosol retrieval over urban surfaces.

1. We reemphasize that the algorithm uses only single scattering and assumes only a single fine mode. While these assumptions can be relaxed by including full multiple scattering and assuming a coarse mode, the lack of a long wavelength channel makes it impossible to separate the fine and coarse components thereby biasing the AOD. This makes aerosol retrieval in urban coastal areas or areas with transported dust aerosols difficult.

2. The requirement of single scattering makes the AOD retrieval for wavelengths ¡ 670 nm problematic and unfortunately these wavelengths are critical for SSA estimates [Waquet et al., 2009].

3. The polarized surface models need to be tuned to the specific region. Significant errors are seen using a single global parameterized polarized reflectance and it has not yet been established that unique parameterizations for each land classification are sufficient to retrieve aerosols over diverse urban areas.

4. Therefore, regional tuning of the surface seems to be necessary even for POLDER.

5. The inclusion of a SWIR channel into the polarized measurement system would provide a very significant improvement and allow a separation of fine and coarse mode as well as providing an accurate retrieval of SSA.

3.2 GOES aerosol and smoke product (GASP) algorithm

It is quite apparent that observations from polar orbiters are not frequent enough to address many air quality measurement and forecasting issues. Clearly, there is a strong need for near real time aerosol information with high temporal resolution for air-quality applications.

Therefore, it is not surprising that efforts to retrieve aerosol properties from Geostationary Platforms have been actively pursued.

The current operational GASP algorithm [Knapp, 2002a, Knapp et al., 2002b, 2005] is a retrieval of AOD from GOES imagery. The GASP algorithm is performed with the imager data collected by the current GOES-13 (EAST). But the GASP retrievals were dated back to the the GOES-8 [Knapp, 2002a, Knapp et al., 2002b, 2005]. Unlike the multispectral polar orbiting sensors (MODIS, MISR, etc.), GASP only uses a single visible (VIS) channel to retrieve AOD. So, strong assumptions must be made in the retrieval process.

The imager of GOES measures the TOA radiance in one visible channel and 4 infrared channels with a fixed viewing angle. The visible channel is used for aerosol retrieval, while the infrared channels are used for cloud masking process. The cloud mask algorithm was adapted from AVHRR's cloud masking algorithm [Stowe et al., 1999, Heidinger et al., 2001]. Although the spatial resolution of the visible channel is 1 x 1 km, the GASP AOD resolution is aggregated to 4 km because the infrared channels used in the cloud masking process are 4 x 4 km in resolution. So, the visible imagery data was first averaged to 4 x 4 km before processing.

Before performing the AOD retrieval, the instrument response data GVAR transmitted by GOES needs to be converted into radiance or reflectance based on the pre-launch and post-launch calibration coefficients [Weinreb et al., 1997, Weinred and Han, 2009]. Unlike level 1 data sets from MODIS which are available in calibrated TOA radiance or reflectance, the GOES data is in raw format of digital counts which are the sensor's spectral response to the solar intensity.

The pre-launch calibration for all GOES imager follows the Equation 3.2 and Equation 3.3. The Equation 3.2 is for converting GVAR into spectral radiance R_{pre}. The Equation 3.3 is for converting GVAR to nornimal reflectance A$_{pre}$.

$$R_{pre} = m(X - X_{space}) \tag{3.2}$$

$$A_{pre} = k(X - X_{space}) \tag{3.3}$$

where X is the spectral response of sensor's visible channel. In Equation 3.2, m is the calibration coefficient, which is also commonly referred as slope. In Equation 3.3, k is the ratio of m to nominal solar radiance, which is the spectral radiance when the Sun is at local zenith and mean Sun-Earth distance. X$_{space}$ is the instrument response to space scene where signal is expected to be zero. For GOES imager, the X$_{space}$ should always be 29. Thus, the Equation 3.2 can be re-written as

$$R_{pre} = mX - b \tag{3.4}$$

where $b = mX_{space}$. The unit of R_{space} is $Wm^{-2}sr^{-1}m^{-1}$. Similarly, Equation 3.3 can be re-written as

$$A_{pre} = kX - \beta \tag{3.5}$$

where $\beta = kX_{space}$. Since A_{pre} is the ratio between the R_{pre} and nominal solar radiance, the A_{pre} is unitless and the value is between 0 and 1. The values of m and k are provided for each GOES satellite in Table 3.2.

Since GOES imager does not have onboard calibration instruments, a variety of calibration methods are applied such as star-based calibration [Chang et al., 2008], lunar-based calibration [Wu et al., 2006]. The operational post-launch calibration uses GOES-MODIS

Table 3.2: Pre-launch calibration coefficients for GOES 8-15 imager visible channels. (Source: `http://www.star.nesdis.noaa.gov/smcd/spb/fwu/homepage/GOES_Imager_Vis_PreCal.php`)

	m	k
GOES-8	0.5502	0.001062
GOES-9	0.5492	0.001067
GOES-10	0.5582	0.001110
GOES-11	0.5562	0.001121
GOES-12	0.5771	0.001141
GOES-13	0.6118	0.001160
GOES-14	0.5861	0.001106
GOES-15	0.5854	0.001106

inter-satellite calibration to provide the post-launch calibration coefficients for GOES imager visible channel [Wu, 2003, Wu and Sun, 2005]. This method uses well calibrated MODIS measurements to calibrate the GOES imager visible channel since both measurements are regularly co-located, and both measurements are in similar spectral interval and of similar spatial resolution. The implementation of the post-launch calibration follows the the Equation 3.6 for radiance and Equation 3.7 for reflectance.

$$R_{post} = C * R_{pre} \tag{3.6}$$

$$A_{post} = C * A_{pre} \tag{3.7}$$

where R_{post} is the post-launch calibrated radiance, A_{post} is the post-launch calibrated reflectance, C is the post-launch correction ($C = \alpha * exp(bt)$) which accounts for the accumulated degradation.

The first step in the GASP algorithm is to estimate the surface reflection by using background composite image technique. Unlike multispectral sensors which can estimate the surface reflectivity from long wavelength observations which have less aerosol effects, or multi-angle sensors which can utilize the angular information obtained in the observations to extract the surface reflection, the GASP only uses observations in visible channel. Thus, the GASP makes the use of high temporal resolution observations to estimate the surface reflectivity. In this step, the clear-sky background image needs to be created for the observation that the aerosol retrieval will be performed. This background image is created by selecting the second darkest observations for each pixel from the past 28 days images of the same time period. For example, to create the background image for observation of 06/30/2011 19:15 GMT, the images of time in 19:15 GMT from 06/03/2011 to 06/30/2011 will be used, then the second lowest values will be selected for each pixel. From the composite background image, the surface albedo is retrieved using the LUT generated with the Second Simulation of the Satellite Signal in the Solar Spectrum (6S) radiative transfer model [Vermote et al., 1997] with assumption that the background aerosol loading is minimum at 0.02. This process is possible to isolate the ground albedo contributions simply by making observations over sufficiently long periods of time and expecting that in such a long time period "clean" atmospheres in which the aerosol loading is negligible, can be observed. Then, assuming the same surface albedo holds over the entire period, the aerosol contribution can now be determined for all other cloud cleared observations. The choice of using the second darkest pixel instead of the darkest is to avoid or reduce cases where cloud shadow contamination might arise [Knapp et al., 2005]. Also, although the choice of 28 days is fixed in the operational code, it should be pointed out that such rules may not be optimal and can vary seasonally and geographically. Generally, the choice was made as a way of balancing between a longer time period, which increases the chances of finding an image with clear sky conditions, and a shorter time period to increase the probability that the underlying surface reflectivity is stable.

After the surface contribution is retrieved, the next step in GASP is quite straightforward for retrieving AOD from the visible channel image. The AOD retrieval includes corrections of gaseous absorption and Raleigh scattering with assumption that the aerosol model is continental aerosol used in 6S radiative transfer code [Vermote et al., 1997]. The gaseous absorption is calculated using a U.S. standard atmosphere water vapor and ozone profile. The Raleigh scattering is calculated using surface topography data from the National Geophysical Data Center TerrainBase data set [Prados et al., 2007].

The routine GASP retrieval is performed with GOES Northern Extended scan, which occurs every 30 minutes at 15 or 45 past the hours. The AOD imagery is available at `http://www.ssd.noaa.gov/PS/FIRE/GASP/gasp.html`. A sample image of GASP AOD is shown in Figure 3.1.

The binary format of the AOD product is available at `ftp://satepsanone.nesdis.noaa.gov/GASP/AOD/`.

3.3 Assessment of GASP against AERONET retrieved AOD

3.3.1 AERONET retrieved AOD

The Aerosol Robotic Network (AERONET) is a ground-based aerosol remote sensing networks established by NASA in collaboration with other regional agencies, institutes, universities, and individuals, such as PHOTONS in France and RIMA in Spain. The global AERONET sites coverage is shown in Figure 3.2. The AERONET provides long-term continuous and public accessible data sets of aerosol optical, radiative, and microphysical properties. The AERONET data sets are widely used for validation purpose of satellite aerosol retrievals.

The standard instrument deployed in AERONET is CIMEL sun photometer as shown in Figure 3.3. It measures the direct solar irradiance and diffuse sky radiance with 1.2o field of view (FOV) at almucantar and principal solar plane. The measurements at selected wavelengths of 340, 380, 440, 670, 870, 1020 nm is for retrieving aerosol, while the wavelength of 936 nm is for water vapor. The inversion algorithm to retrieve AOD and other aerosol properties, such as refractive index, single scattering albedo, the phase function, the size

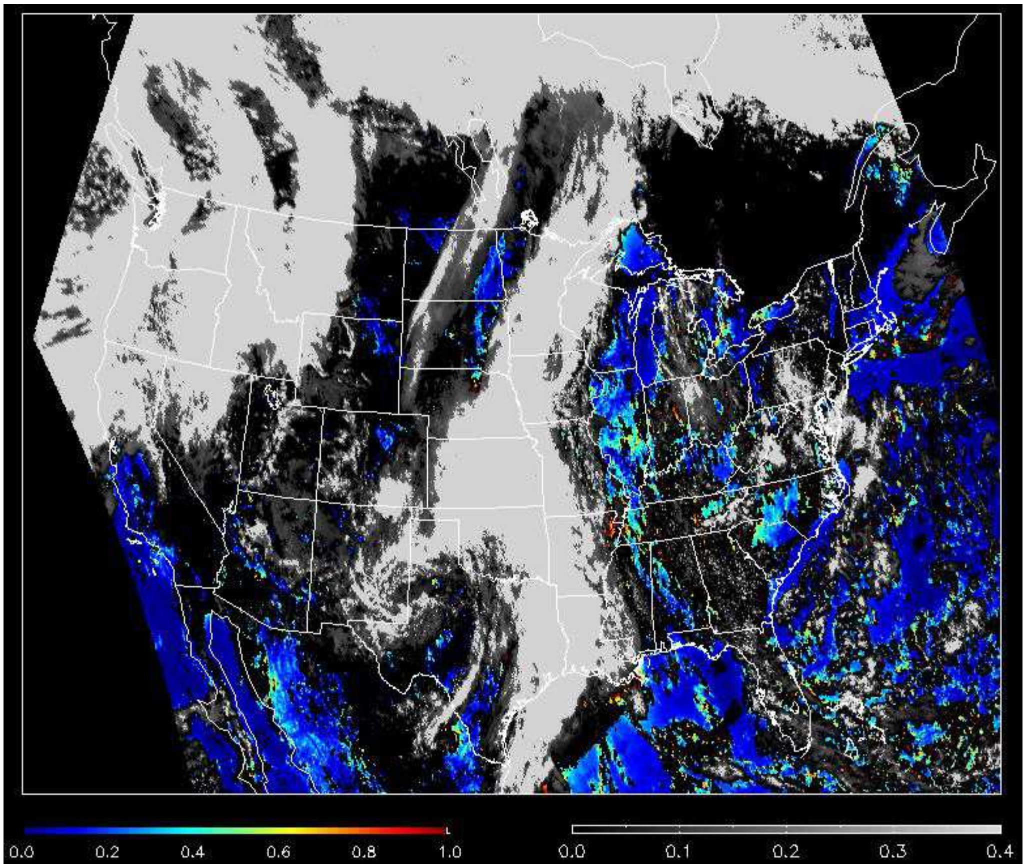

Figure 3.1: GASP AOD image of 19:15 UTC 03/20/2012. The color scale is for indicating the AOD from 0.0 to 1.3. The background image is the visible channel image shown in grey scale. (Source: `http://www.ssd.noaa.gov/PS/FIRE/GASP/AOD/latest_US.jpg`)

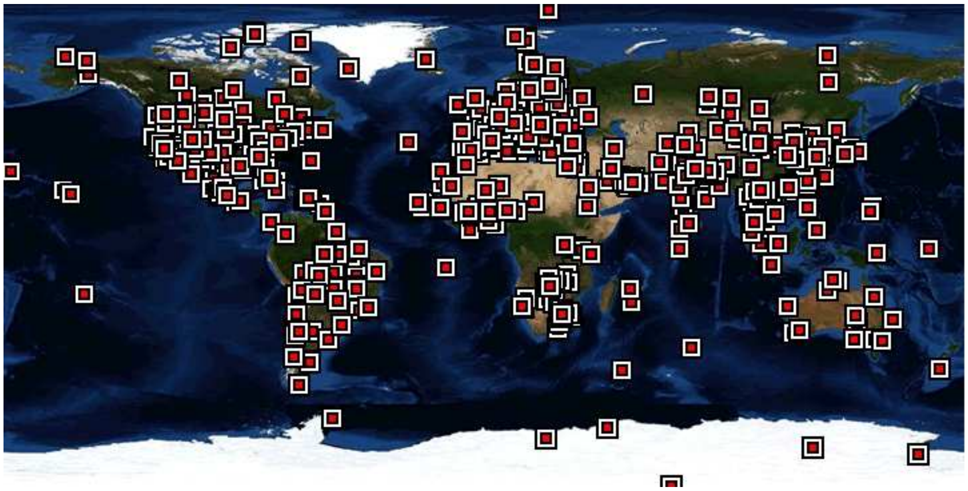

Figure 3.2: The global AERONET sites. (source: NASA)

Figure 3.3: The CIMEL sun photometer mounted at City College of New York (CCNY in AERONET).

distribution, from the sun photometer measurements is developed by Dubovik and King [2000]. The principle of the AERONET inversion algorithm consists two components: an accurate forward radiative transfer model and optimized mathematical procedures to invert the measured radiance data with a priori constrains [Dubovik and King, 2000, Estelles et al., 2012].

3.3.1.1 The basic equation for AERONET retrieved AOD

The direct solar irradiance F measured by sun photometer is assumed to obey Bouguer-Lambert-Beer law:

$$F(\lambda) = F_0(\lambda) exp(-m_0 \tau(\lambda)) \tag{3.8}$$

where F_0 is the monochromatic irradiance at the top of atmosphere at wavelength λ and standard Sun-Earth distance of 1 astronomical unit, m_0 is the optical air mass ($m_0 \approx 1/cos(\theta_0)$), θ_0 being the solar zenith angle, τ is the total optical depth.

The total optical thickness $m_0\tau$ includes several terms τ_j which describes the extinction by different atmospheric components: Rayleigh scattering, gaseous absorption and aerosol extinction. It is easily to see that aerosol optical depth can be retrieved from Equation 3.8 after subtraction of the Rayleigh scattering and gaseous absorption optical depth, if the ground irradiance F is measured and the solar irradiance at TOA F_0 is known.

3.3.1.2 AERONET AOD data set

As mentioned earlier, the sun photometer measurements can retrieve aerosol optical depth as well as other aerosol properties. In particular, it is of the most interest for us is the retrieved AODs at 0.34, 0.38, 0.44, 0.50, 0.67, 0.87 and 1.02 μm with an uncertainty of 0.01 [Holben et al., 2001]. These retrieved AODs allow us to obtain interpolated AOD at 0.550μm, which is comparable to the satellite retrieved AOD products.

The AERONET AOD data sets are computed for three data quality levels: Level 1.0 (unscreened), Level 1.5 (cloud-screened), and Level 2.0 (cloud-screened and quality-assured). For our purposes, both the spectral AOD and Level 1.5 Direct Sun and Inversion measurement data sets are downloaded from `http://aeronet.gsfc.nasa.gov` [AERONET]. While the purpose of the AOD retrievals is obvious, the calculation of the angstrom coefficient also allows us to filter out cases where coarse mode aerosols are significant. In addition, time series data are used to assess homogeneity of aerosol conditions which are requires if consistent matchups with satellite products is attempted.

The simplest way to explore the AERONET AOD data sets is to plot the time series of the AODs. The time series can illustrate the AOD variation by season or by diurnal or by annual. We chose two AERONET observation sites to demonstrate the time series observation of AODs. One site is City College of New York (CCNY in AERONET). The sun photometer at CCNY is located in Manhattan of New York city, where the latitude is 40.82131 North, longitude is 73.94904 West with 100.0 Meters in elevation. The other site is Brookhaven National Laboratory at Upton, New York (Brookhaven in AERONET). The Brookhaven site coordinates and elevation are: latitude is 40.87000 North, longitude is 72.88917 West, and elevation is 33.0 meters.

The instantaneous and hourly average AODs of two sites from 2011 level 1.5 data sets were plotted as shown in Figure 3-4. The instantaneous AOD is the AOD retrieved from each sun photometer measurement. The hourly average AOD is the mean AOD of the hour in which two or more AOD retrievals are performed. The standard deviation of the hourly average AOD is also plotted with the error bar in Figure 3.4.

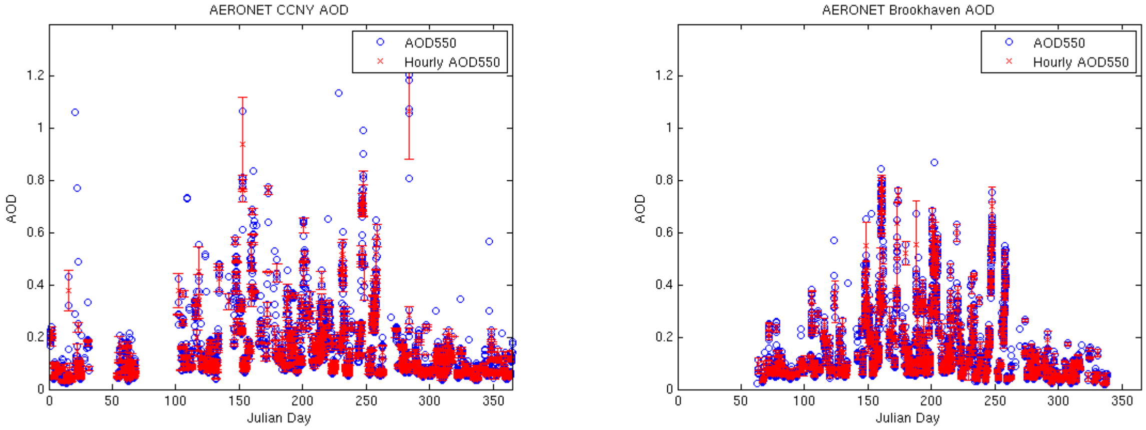

(a)

(b)

Figure 3.4: AERONET instantaneous and hourly averaged AODs of 2011 level 1.5 data sets for (a) CCNY, (b) Brookhaven

We can see that there is seasonal variations in AODs in both sites. The summer season has high AODs while the low AODs were observed in spring and winter seasons. Both sites are within the metropolitan area of New York. So, it indicates that during the summer season the aerosol emission is much active than other seasons, which might be linked to the human activities in the summer season. It is also interesting to note the spatially correlation of two sites. The two site are about 60 miles apart. One is in the center of New York city, the other is in the suburb of New York city. Although both have similar seasonal AOD variability, the magnitude of CCNY is much higher than Brookhaven.

3.3.2 Comparison of GASP and AERONET retrieved AOD

It is of importance to examine the accuracy of the GASP before we can use its data set to study aerosol-cloud interaction. Uncertainty study examined possible errors introduced by which includes the cloud contamination, the assumption of aerosol loadings of 0.02 for clear sky condition, the number of days for selecting the composite background imagery, the uncertainty in surface estimation, and concluded that there is 18% to 34% errors in GASP retrieval [Knapp, 2002a, Knapp et al., 2002b]. Previous assessment of GASP has shown that the retrieved AOD has higher correlation against AERONET AODs in the east coast region while the performance is quite poor for the west region [Prados et al., 2007]. The evaluation of aerosol models also suggests that the biomass-burning aerosol model lead to lower RMS difference between GASP and AERONET AODs [Kondragunta et al., 2008].

We chose AERONET sites from north eastern and western regions to conduct the assessment of GASP performance. We also separate the data sets in to seasons. However, the winter season is not included due to the poor statistics of the retrieved AOD from satellites. In the north eastern region, we chose CCNY and GSFC. In the west region, UCSB is chosen because it has a full year AERONET observation in 2011. It is quite clearly that GASP in north eastern region performs better than the western region. We can also see that the summer season has the best performance of all. However, we also noticed the reverse behavior of CCNY and GSFC in high AOD cases in summer. CCNY tends to have underestimates of the high AODs, while GSFC seems to overestimate the high AODs in summer. It is also noticed that the dramatic underestimates from the satellite in fall season in UCSB. All of them lead us to explore the differences in aerosol models which is discussed in details in section 3.4.

3.4 Aerosol models

The aerosol optical properties are mainly determined by the size distribution, the shape, the chemical composition, as well as the total particle concentration. However, for modeling

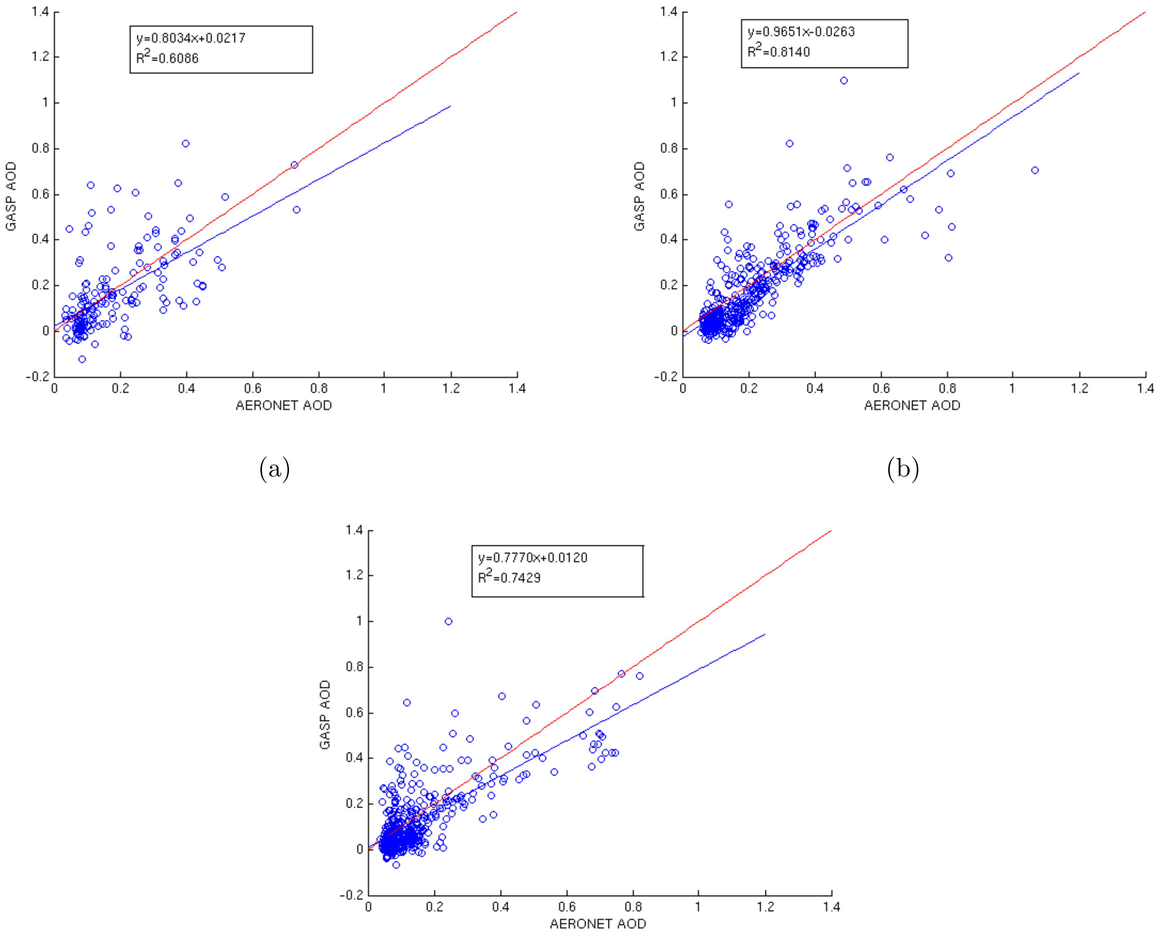

(a)

(b)

(c)

Figure 3.5: Matchups between GASP and AERONET AOD at CCNY for (a) Spring, (b) Summer, (c) Fall seasons.

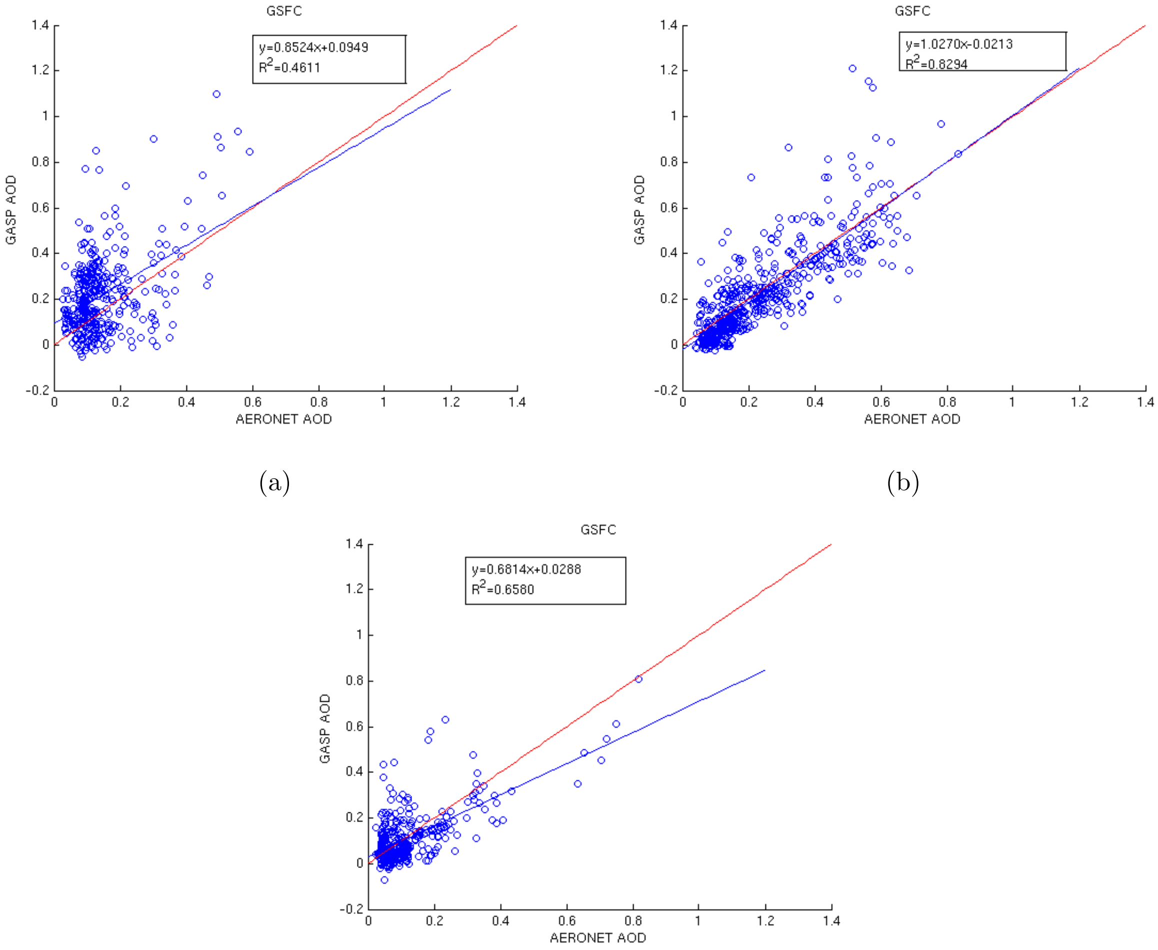

(a)

(b)

(c)

Figure 3.6: Matchups between GASP and AERONET AOD at GSFC for (a) Spring, (b) Summer, (c) Fall seasons.

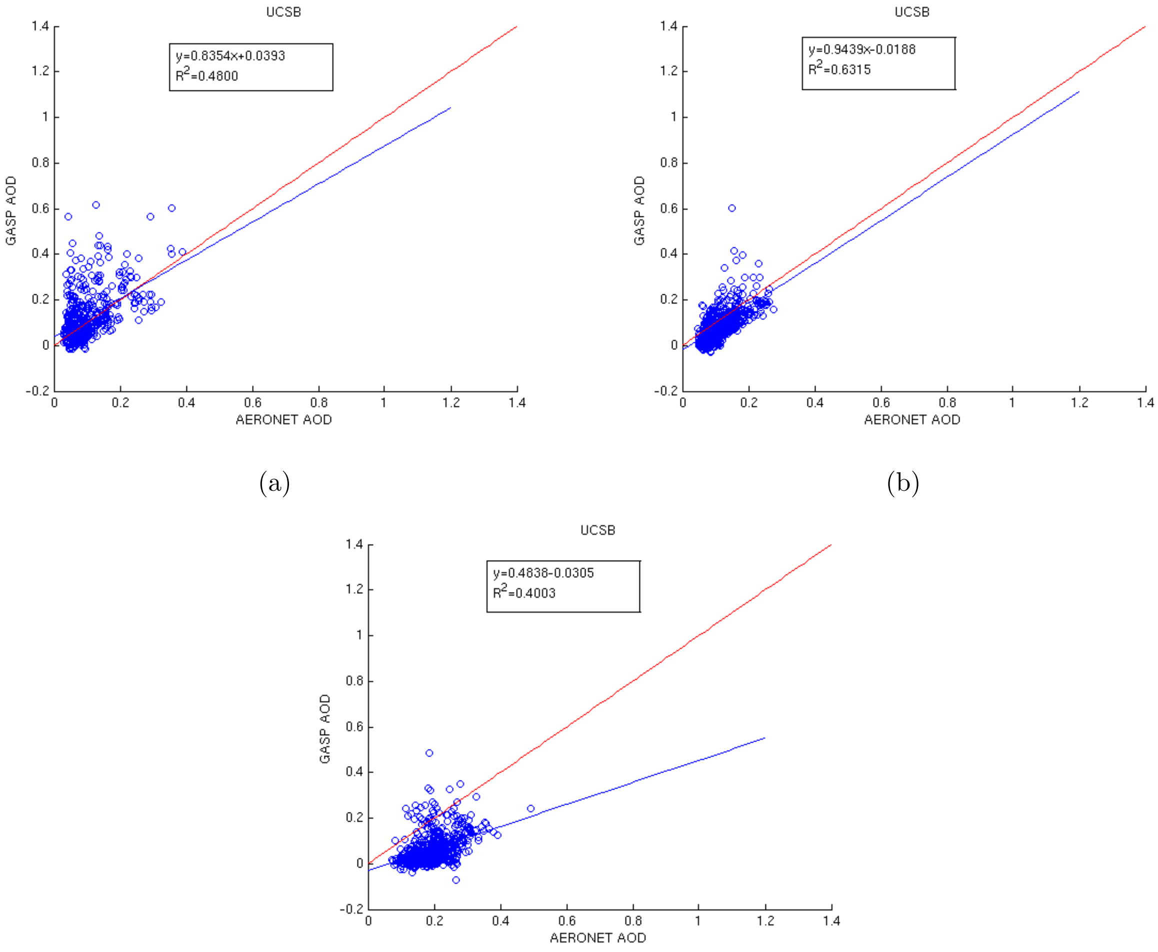

(a) (b)

(c)

Figure 3.7: Matchups between GASP and AERONET AOD at UCSB for (a) Spring, (b) Summer, (c) Fall seasons.

purpose, it is of importance to have simplified models which capture the main microphysical characteristics of atmospheric aerosol in a correct way and offer a simple way for the optical modeling [Kokhanovsky, 2008]. The simplest assumption used for most aerosol models is that aerosols are spherical and are externally mixed [Hess et al., 1998, Seinfeld and Pandis, 1998]. In this important case, aerosols are described by a small number of parameters that define the size distribution or modes and the complex refractive index.

Before introducing the aerosol size distribution model, it is worth reviewing the Ångstrom exponent. AOD can be easily retrieved in discrete spectral intervals with sun photometer measurements. However, at the strong gaseous absorption spectral wavelengths, it is quite difficult to measure the AOD. Ångstrom [1929] was first noted that the spectral dependency of aerosol extinction may be approximated by a power-law relationship:

$$\frac{\tau(\lambda)}{\tau_0} = (\frac{\lambda}{\lambda_0})^{-\alpha} \tag{3.9}$$

where $\lambda(\tau)$ is spectral AOD at wavelength τ, τ_0 is the AOD at reference wavelength λ_0, and α is the Ångstrom exponent. In additional to extrapolating AOD, Ångstrom exponent is a qualitative indicator of aerosol sizes. Small particles that usually associated with air pollution and biomass burning have large Ångstrom exponent, while large particles typically found with dust or sea salt have small Ångstrom exponent.

Based on careful measurements of aerosol sizes conducted over many parts of the world , Junge [1952] was first to show that the size distribution of aerosols whose radii range between 0.1 and 20 μm can be described as the power-law function:

$$\frac{dN(r)}{dlog(r)} = Ar^{-\gamma} \tag{3.10}$$

where A and γ are the coefficients that characterize the size distribution, $N(r)$ is the aerosol number density, r is the aerosol radius. It is shown that $\gamma \approx \alpha + 2$ for non-absorbing aerosols with $\alpha > 1$ [Junge, 1955, 1963]. This relationship has the strength in simplicity. Till today, it is still found in many literatures and even 6S radiative transfer model having an option of aerosol distribution in Junge Law. However, the simple relation does not hold for small value of α ($\alpha < 1$) or absorbing aerosols. Thus, the usefulness of the Junge aerosol size distribution is quite limited.

Most commonly, the aerosol size distribution is described by multimodal log-normal function [Davies, 1974, Whitby, 1978, Ott, 1990]:

$$\frac{dV(r)}{dln(r)} = \sum_{i=1}^{n} \frac{V_i}{\sqrt{2\pi}\sigma_i} exp(-\frac{1}{2}(\frac{lnr - lnR_i}{\sigma_i})^2) \tag{3.11}$$

where V_i is the particle volume concentration, R_i is the median or geometric mean radius, σ_i is the standard deviation or width of each mode, and n is the number of log-normal aerosol modes. Here, the volume concentration $dV(r) = 4/3\pi r^3 dN(r)$ is used because the optical effects of aerosols are found to be more closely related to their volume than their number [Whitby, 1978, Seinfeld and Pandis, 1998]. Study [Whitby, 1978] has also shown that the modes of aerosols could be described in three categories shown in Figure 3.8:

a ultra fine or nuclei mode with geometric mean radii of 0.0075-0.020 μm, an accumulation or fine mode with geometric mean radii of 0.075-0.25 μm, and a coarse mode with geometric mean radii of 2.5-15 μm. The fist mode is less relevant from a climate standpoint, since the ultra fine particles accumulate rapidly into larger particles.

In particular, the aerosol size distribution is commonly described with two modes: fine mode aerosol and coarse mode aerosol with log-normal distributions. In fact, the bimodal log-normal distribution parameterization is used in almost all satellite remote sensing efforts given by Equation 3.12 which is consistent with measurement retrievals taken from

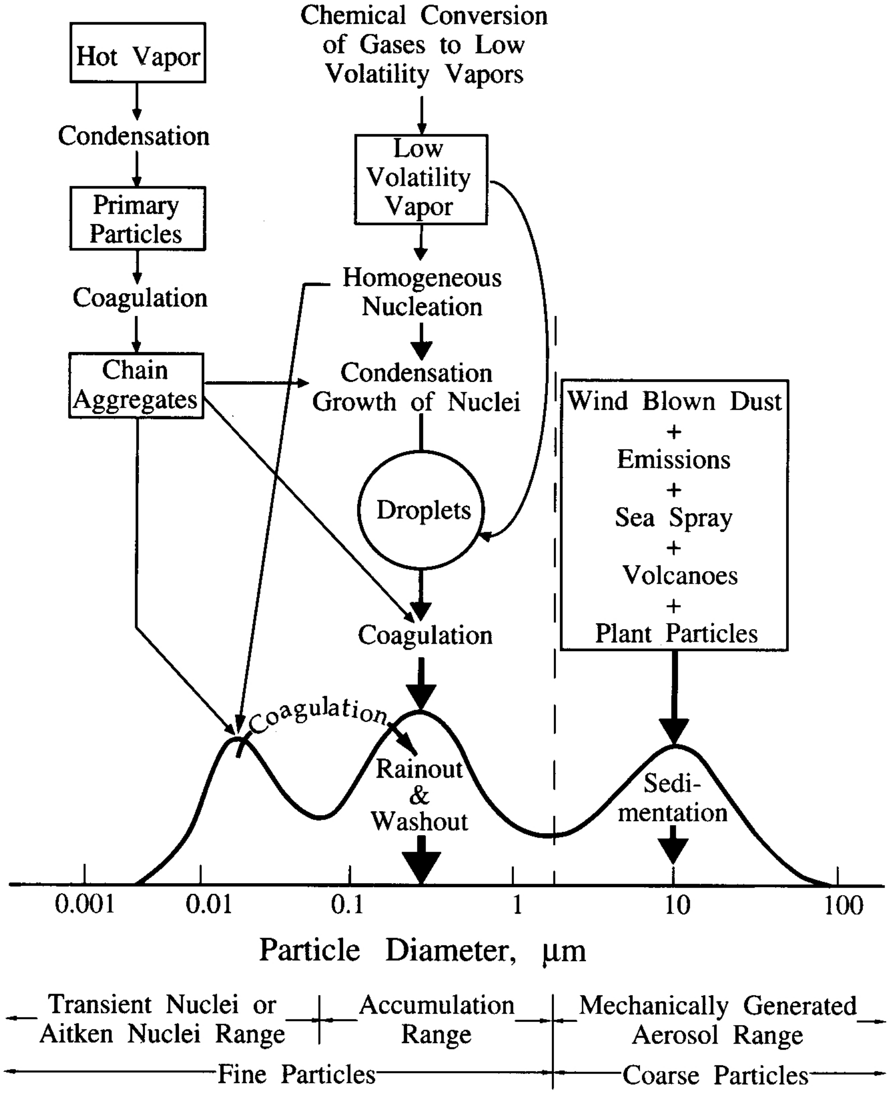

Figure 3.8: The sources and sinks of atmospheric aerosols along with their ultrafine, fine, and coarse modes of their size distribution. (source: [Seinfeld and Pandis, 1998])

AERONET.

$$\frac{dV(r)}{dlnr} = \frac{V_f}{\sqrt{2\pi}\sigma_f} exp(-\frac{1}{2}(\frac{lnr - lnR_f}{\sigma_f})^2) + \frac{V_c}{\sqrt{2\pi}\sigma_c} exp(-\frac{1}{2}(\frac{lnr - lnR_c}{\sigma_c})^2) \tag{3.12}$$

here, the log-normal parameters $V_i, R_i, \sigma_i, i = f, c$ describe the total volume in each mode, the mean mode radius and mode width. AERONET is an extensive global scanning sky radiometer network capable of retrieving not only AOD but bimodal size distribution parameters [Dubovik and King, 2000, Dubovik and Holben, 2002a,b] and complex refractive index (or SSA) and functions as the main validation network in which satellite remote sensing aerosol retrievals are compared.

The characteristics of aerosols from AERONET for different regions worldwide show significant variability not only in AOD but in the ratio of fine - coarse mode and SSA [Dubovik and Holben, 2002b]. The main urban feature in contrast with other cases (desert, oceanic) is the higher fine mode aerosol contribution with angstrom coefficients ranging from $1.2 \leq \alpha_{440-870} \leq 2.5$ [Schuster et al., 2006]. Aerosol absorption in urban areas such as the North East (NE) coast of the US have high SSA at 440nm $0.92 \leq \omega_0 \leq 0.98$ but cases such as Mexico City with heavy biomass burning contributions have SSA much smaller with ranges $0.60 \leq \omega_0 \leq 0.92$. This is consistent with the high degree of variability expected since the albedo strongly depends on the age of the burning aerosol from the combustion source.

In addition, it is possible that the effective mode radii can depend on optical depth. This dynamic feature occurs for hygroscopic aerosols which, by definition, undergo changes in both physical (effective radius) and optical (refractive index) when subjected to high relative humidity RH [Hanel, 1976] conditions. Examples of such aerosols include ammonium sulfate (NH4)2SO4, sea salt, and ammonium nitrate NH4NO3 which, for example, are the dominant modes in many urban coastal areas (i.e., North East US). However, not all aerosols are hygroscopic [Vlasenko et al., 2005]. Most prominent among these are desert (mineral) dusts and most organic aerosol species. Therefore, aerosol models must account for the high probability of these aerosol classes in different areas of the world. For example, aerosol models are best modeled as static over the West Coast, USA and in many other world regions where dust and organic aerosol components are significant while dynamic models are best suited to hygroscopic aerosols (NE). Further complications arise with mineral dust species since these particles are far from spherical. To model these aerosols, non-spherical models including the most popular model of spheroids [Dubovik et al., 2006] are used in operational models. These models may be considered within the general Particle Size Distribution framework since they are characterized by a size distribution and refractive index. However, realistic assumptions on the statistics of the aspect ratio (semi major / semi minor axis) of constituent ellipsoids must be assumed a-priori.

3.4.1 Continental aerosol model

The aerosol model used in GASP algorithm is continental aerosol model [WCP-112], which is also provided in 6S [Vermote et al., 1997]. Four basic components which are dust-like (DL) component, oceanic component (OC), water-soluble (WS) component, and soot component (SC), have the pre-defined size distributions and refractive index. The continental aerosol model as well as maritime and urban aerosol models are created by externally mixing those four basic components with the volume percentages in Table 3.3.

For each component, the volume concetration V_i and the particle number concentration N_i is computed using the log-normal distribution shown in Table 3.4, where $V_i = \frac{4\pi}{3}\int_0^{infity} r^3 \frac{dN_i(r)}{dr} dr$

Table 3.3: Mixing volume percentage of four basic components for continental, maritime, and urban aerosol models.

	DL	OC	WS	SC
Continental	0.7		0.29	0.01
Maritime		0.95	0.05	
Urban	0.17		0.61	0.22

Table 3.4: Volume concentration and particle number concentration of four basic components.

	DL	OC	WS	SC
$V_i, \mu m^3/cm^3$	113.98	5.14	$113.98 * 10^{-6}$	$59.78 * 10^{-6}$
$N_i, part/cm^3$	54.73	276.05	$1.87 * 10^6$	$1.87 * 10^6$

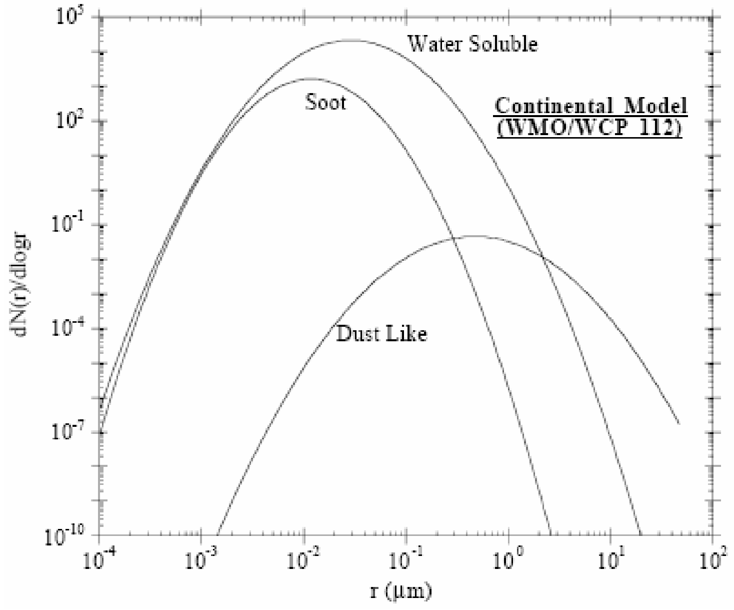

Figure 3.9: Log-normal size distribtuion function for continental aerosol model (WCP-112).

The size distribution of the continental aerosol model is shown in Figure 3.9

3.4.2 Local aerosol model derived from AERONET

As discussed in section 3.4, the AERONET retrieved aerosol size distribution follows the bimodal log-normal function. The fine and coarse mode aerosol parameters are retrieved from each sun photometer measurement by using the version 2 inversion algorithm [Dubovik and King, 2000]. In order to generate the seasonal aerosol size distribution, all retrieved size parameters, in particular the median of the mode R_i and the standard deviation of the mode σ_i, are averaged for each season. For the year of 2011, we generate the local aerosol size distribution of spring, summer, and fall seasons, since satellite retrieved AODs are more frequent in these three seasons compared to the winter season in which the AODs are retrieved less frequent from the satellite and with poor quality due to the snow coverage in the Eastern part of the U.S. The seasonal bimodal aerosol size distribution of the three sites is shown in Figure 3.10.

3.4.3 Comparison of aerosol models

Clearly, from Figure 3.10 we can see that the UCSB aerosol has relatively strong coarse mode domination. But to further assess the differences cause by aerosol models, we need to understand the changes in optical properties, which can be obtained from the size distribution and complex refractive index. In particular, we examined the SSA, which indicates the scattering and absorbing characteristics of aerosols. The two sites from north eastern region showed opposite features in SSA, as seen in Figure 3.11.

The CCNY aerosol has lower SSA compared to continental aerosol model, while GSFC aerosol has higher SSA. The different SSA also showed different behavior in the TOA reflection calculated by the 6SV radiative transfer code, shown in Figure 3.12. The differences are even more significant when looking at the SSA from fall season of UCSB regional aerosol model compared to continental aerosol model, shown in Figure 3.13. The UCSB aerosol during the fall season showed relatively strong absorbing characteristics which may be due to the biomass burning in this season. This probably cause the significant underestimates from the satellite retrieval.

3.5 Conclusion for GASP

It is clear that significant errors result when the regional model optical properties are not consistent with the assumed continental model. A particularly illustrative example is the

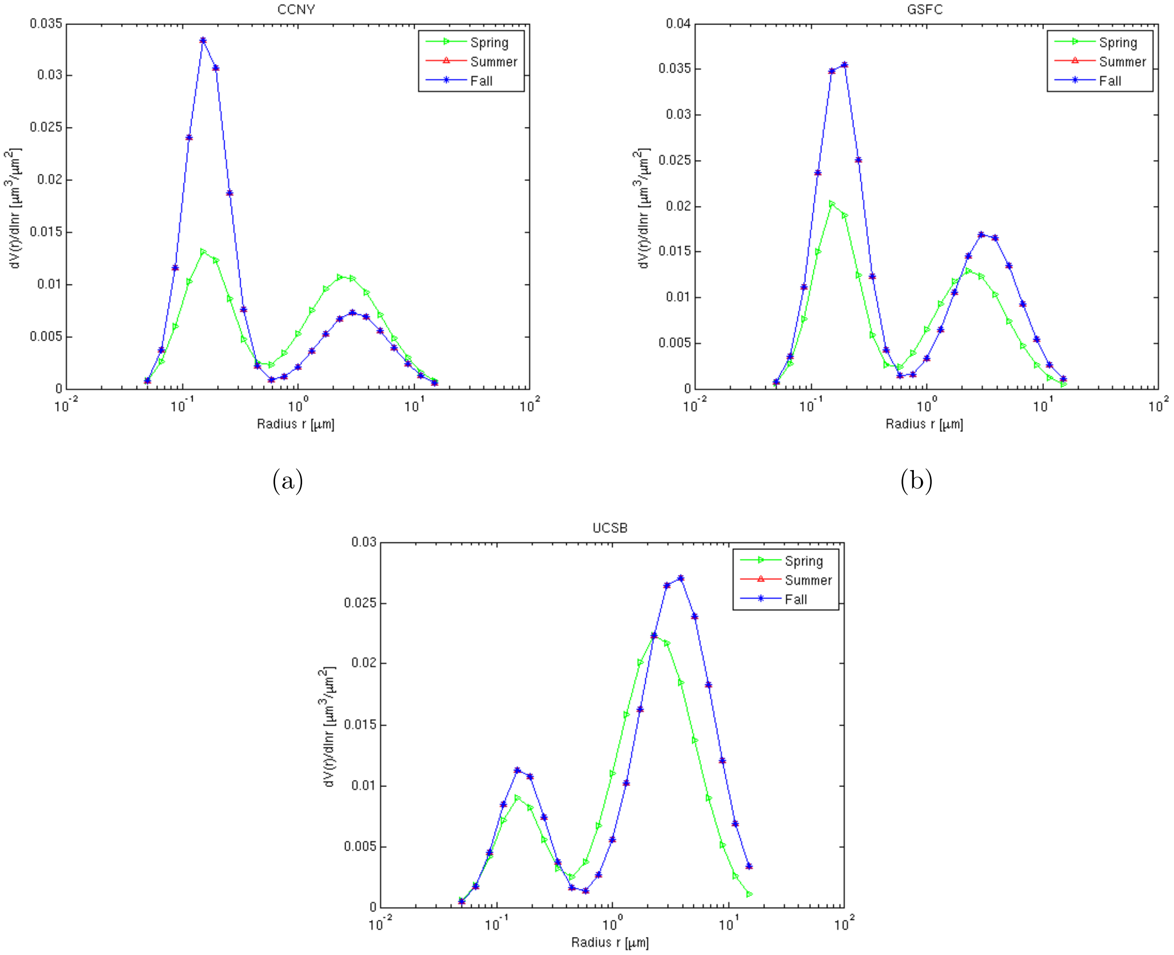

(a)

(b)

(c)

Figure 3.10: Seasonal aerosol size distribution derived from AERONET for (a) CCNY, (b) GSFC, (c) UCSB

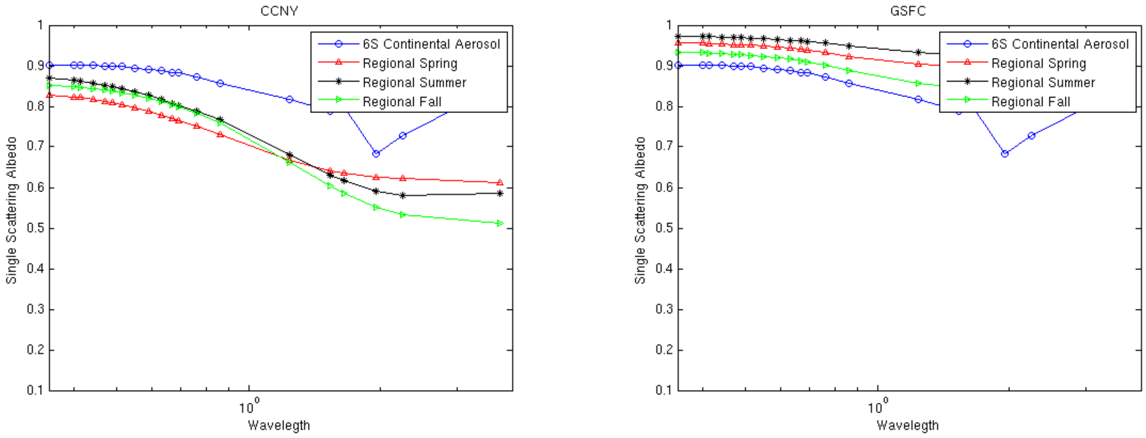

(a) (b)

Figure 3.11: Single Scattering Albedo with regional aerosol model compared to continental aerosol model for (a) CCNY, (b) GSFC

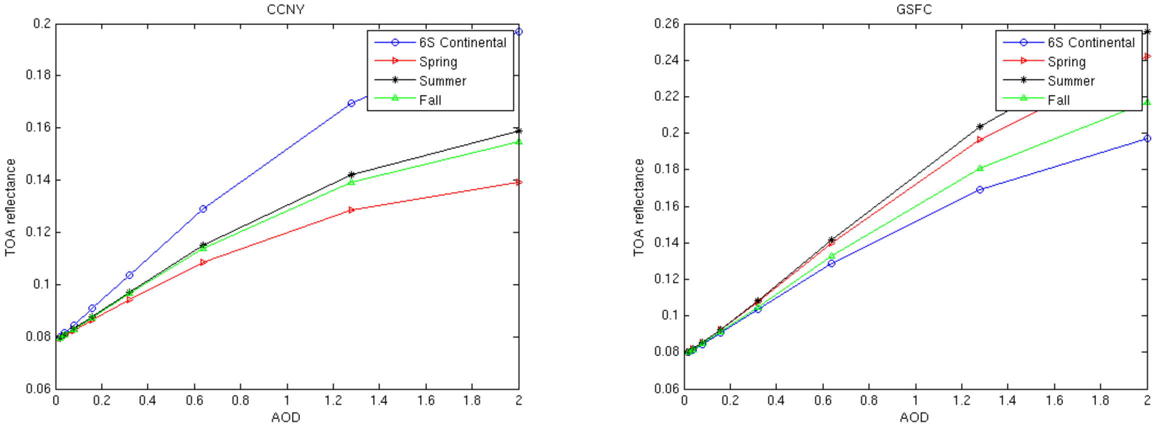

(a) (b)

Figure 3.12: TOA reflection with regional aerosol model compared to continental aerosol model for (a) CCNY, (b) GSFC

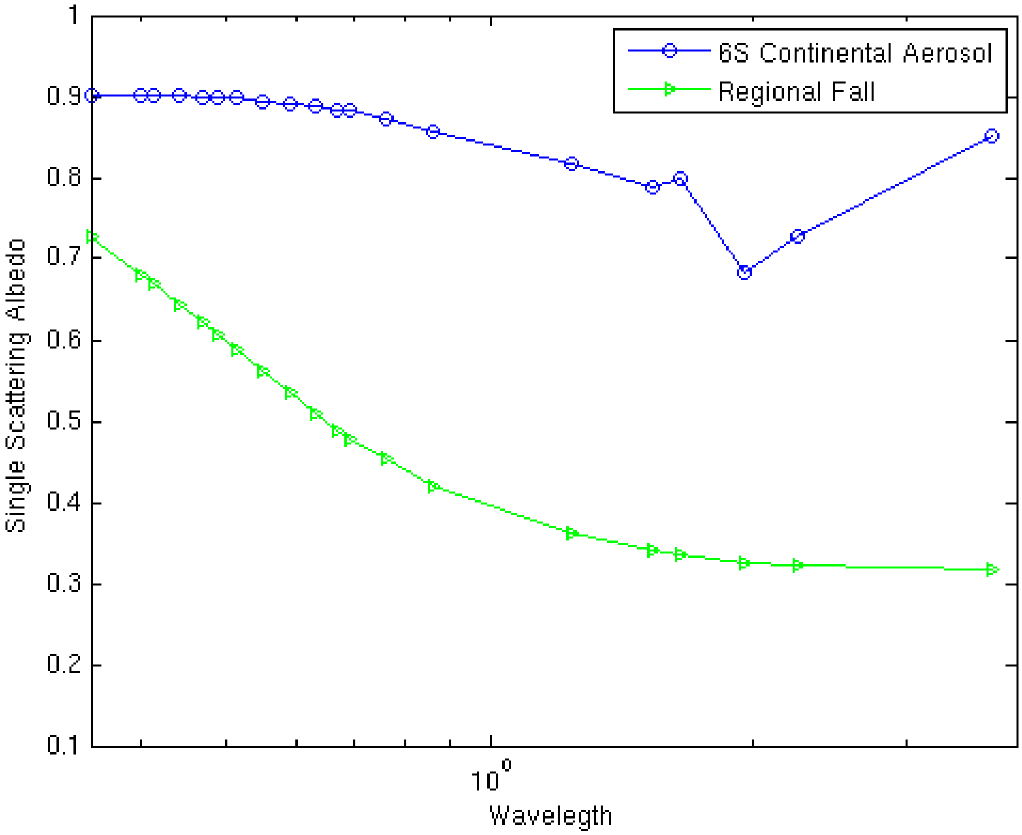

Figure 3.13: Single scattering albedo in fall season from UCSB regional model compared to continental aerosol model.

west coast (USCB) during the fall when heavy smoke events resulted in extremely low surface albedos which strongly bias the AODs. For this reason, it is important to develop multiple LUTs that take into account the diversity of aerosol properties that can occur.

One problem with this is the large CPU requirements needed to generate these LUTs. However, bases on the comparisons, it seems that the natural limitations of the GOES SNR makes it less important to generate the LUT's with the high accuracy (density) being used currently by GASP. We therefore propose to explore the tradeoffs between accuracy and computer complexity in regards to the inversion process. In particular, we focus on studying a relaxation of the LUT dimensions which will undoubtedly decrease accuracy but greaty improve overall LUT development time. A preliminary study of this will be made for the thesis and the modified LUT's will be used to reprocess the USCB datasets.

Chapter 4

Cloud retrieval by GOES

Optical depth retrievals from satellite radiances are particularly sensitive to assumptions regarding particle phase and single scattering properties as well as instrument calibration [Pincus et al., 1995]. For thick cloud cases, uncertainties in satellite optical depth retrievals are further magnified because of the asymptotic relationship between reflectance and optical depth [Min and Harrison, 1996a] where small differences in reflectance equate to very large differences in optical depth as the optical depth becomes large. This uncertainty likely contributes to much of the scatter in our comparisons. Due to horizontal transport of photons, bias in visible optical depth retrievals from satellite radiances are known to occur when the scale of the satellite retrieval is less than a radiative smoothing scale that depends on cloud geometry [Davis and Marshak, 1997]. The cloud retrievals from VISST algorithm (GOES) have been compared with active and passive radiometric measurements at surface sites, primarily at ARM SGP central facility in Oklahoma [Garreaud et al., 2001, Mace et al., 1998, Dong et al., 2002]. Another source of bias in optical depth is caused by sub-pixel variability of optical depth. A satellite radiometer measures pixel mean radiance and from this quantity derives an optical depth that equates to an approximation of the logarithmic mean of the optical depth within the pixel. The exact relationship in any given instance between pixel-mean radiance and the desired pixel-mean optical depth depends on the variability of the cloud field within the pixel [Cahalan, 1994].

4.1 Goes VISST cloud retrieval algorithm

To obtain cloud property measurements (COD and Reff), the need for multi-wavelength imager measurements is critical. Over the past 10 years, significant improvements in multi-spectral satellite sensors onboard polar and geostationary orbiting satellites and the radiative transfer modeling of clouds have provided a mechanism for the retrieval of relevant cloud microphysical properties as well as estimates of aerosol column properties.

In order to improve the climatology of satellite-derived cloud properties over the ARM SGP domain (32N-42N, 91W-105W), the Visible Infrared Solar-infrared Split Window Technique (VISST algorithm), developed by Minnis et al., [1995], is a more advanced algorithm applied on a near real time measurements from the Geostationary Operational Environmental Satellite (GOES). The VISST algorithm utilizes the split window (12.0 m) and the infrared (10.8 m) channels to determine cloud temperature and phase, the visible (0.65 m) reflectance to retrieve COD, and the solar-infrared (3.9 m) radiance to derive cloud particle size. To visualize this VISST algorithm performance, we plot a standard bispectral Figure 4.1

displaying the TOA reflectance measurement space as a function of COD and Reff.

Clearly, the retrieval sensitivity for the cloud effective radius is nearly independent of the VIS COD retrieval. Therefore, a reasonably accurate calibration of the 3.9 micron should

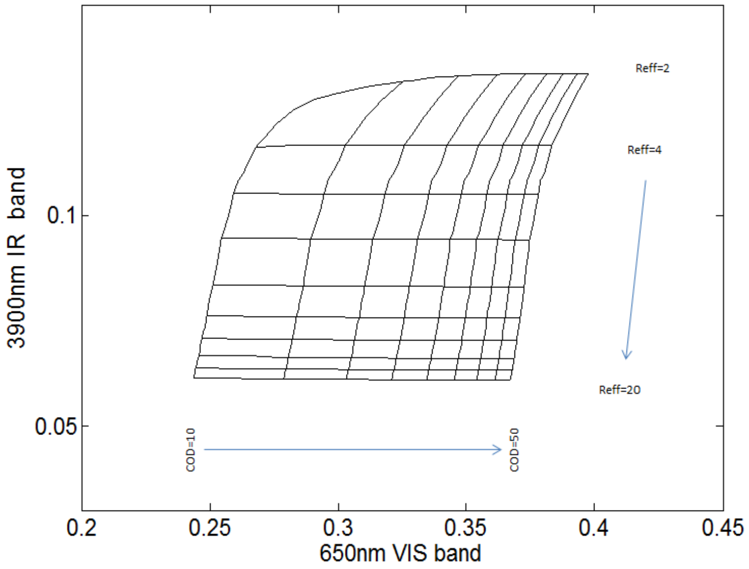

Figure 4.1: Reflectance sensivity plot for VISST channels assuming water phase cloud.

result in quite good retrievals of the Reff as long as the cloud parameterization is reasonably accurate.

The GOES radiances are calibrated with collocated measurements from the TRMM (Tropical Rainfall Measuring Mission Visible Infrared Scanner) [Minnis et al., 2002]. Based on various size distributions of water droplets and hexagonal ice crystal columns, radiances are modeled in VISST to simulate liquid and ice clouds, respectively [Minnis et al., 1998]. The VISST provides cloud optical depth, phase, effective particle size, ice or liquid water path, effective radiating temperature, and effective cloud height (determined from the effective cloud temperature using a vertical profile of temperature for a particular location). The pixel level data from GOES-WEST (G10/G11) & GOES-EAST (G12/G13) over ARM SGP domain can be obtained in netcdf format from the archives of the ARM site.

4.2 Assessment of GOES cloud products

4.2.1 Intercomparison between GOES-VISST and MODIS cloud retrievals

In a fairly similar multispectral approach, the MODIS (Moderate Resolution Imaging Spectroradiometer) Level 2, Collection 5 retrievals [Platnick et al., 2003] are provided at 1 km X 1 km spatial resolution at nadir by combining infrared and visible techniques to determine physical and radiative properties. Using the MODIS visible (0.645 μm) and near-infrared (1.64, 2.13, and 3.75 μm) spectral bands, the daytime shortwave cloud retrieval algorithm over land surfaces will provide the cloud optical thickness and effective particle radius. The 3.75 μm band uses a ten element linear array detector for the 1000 m spatial resolution bands, a 20-element array for the 500 m bands at the 1.64 and 2.13 μm bands, and a 40-element array for the 250 m band at 0.645 μm. To retrieve cloud optical thickness and effective particle radius, a radiative transfer model is first used to compute the reflected intensity field (radiance). This radiance, $I_\lambda(0, -\mu, \Phi)$, is normalized in terms of the incident solar flux, $F_0(\lambda)$, such that the reflection function, $R_\lambda(COD, R_{eff}; \mu, \mu_0, \Phi)$, is given by

$$R_\lambda(COD, R_{eff}; \mu, \mu_0, \Phi) = \frac{\pi I_\lambda(0, -\mu, \Phi)}{(\mu_0 F_0(\lambda)} \tag{4.1}$$

where COD is the total optical thickness of the atmosphere (or cloud), R_{eff} the effective particle radius as defined in Hansen and Travis [1974]. The differences in reflected solar radiation between the 0.645 and 1.64 μm bands contain information regarding cloud particle phase due to distinct differences in bulk absorption characteristics between water and ice at the longer wavelength. If the cloud is composed of ice, or if the surface is snow covered, then reflectance of the cloud at both 1.64 μm and 2.13 μm bands will show a decrease in reflectance, but the reduction is more significant with the former band. Details of retrieval technique are described in King et al. [1997].

All the pixel data covering 10 km and 20 km radii centering the Central Facility at Lamont, Oklahoma are averaged hourly over the four year data period (2007 - 2010). Intercomparison of cloud retrievals from MODIS and GOES in Figure 4.2 show fairly good linear correlation for both COD ($r^2 \approx 0.92$) and Reff ($r^2 \approx 0.86$). Minnis et al. [2011] reported that MODIS tends to throw out a large percentage of small clouds, but the average CODs only differed by ~ 2.0 in non-polar regions. In summary, due to the very similar structure of the algorithms, strong agreement is expected.

4.2.2 Preliminary intercomparison between GOES-VISST and ground based retrievals

The data for a preliminary comparison was given to us by Xiquan Dong which was obtained during the March 2000 IOP campaign over the SGP [Dong et al., 2002]. The cases considered where the ground retrievals were considered robust were made over 4 days from SGP March 2000 IOP "Spring Clouds" campaign (03/03, 03/17, 03/19,03/21/2000). The cumulative results are given in Figure 4.3

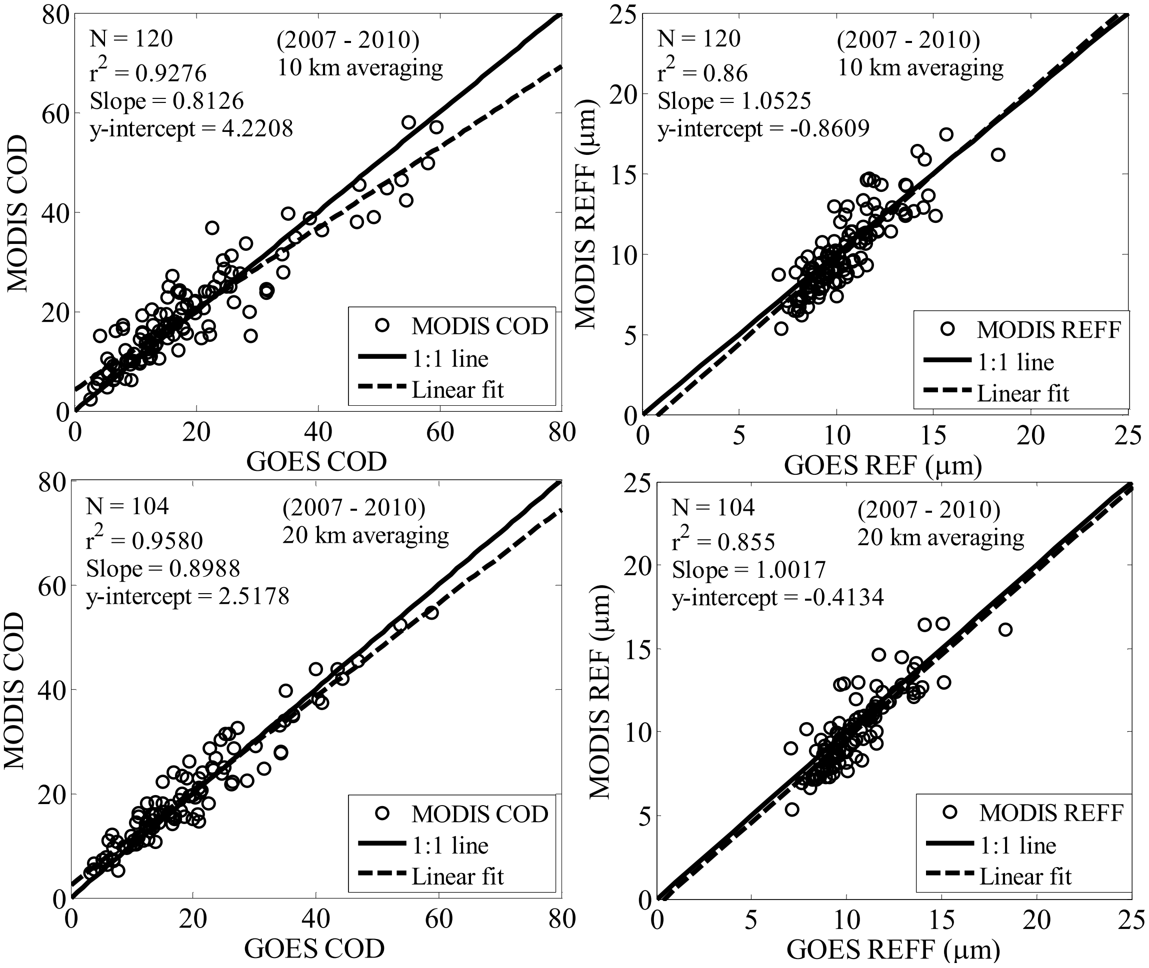

Figure 4.2: Comparison plots of MODIS and GOES derived COD and Reff with 10 km and 20 km averaging centering ARM SGP site Lamont (Oklahoma) for the data covering 2007 - 2010.

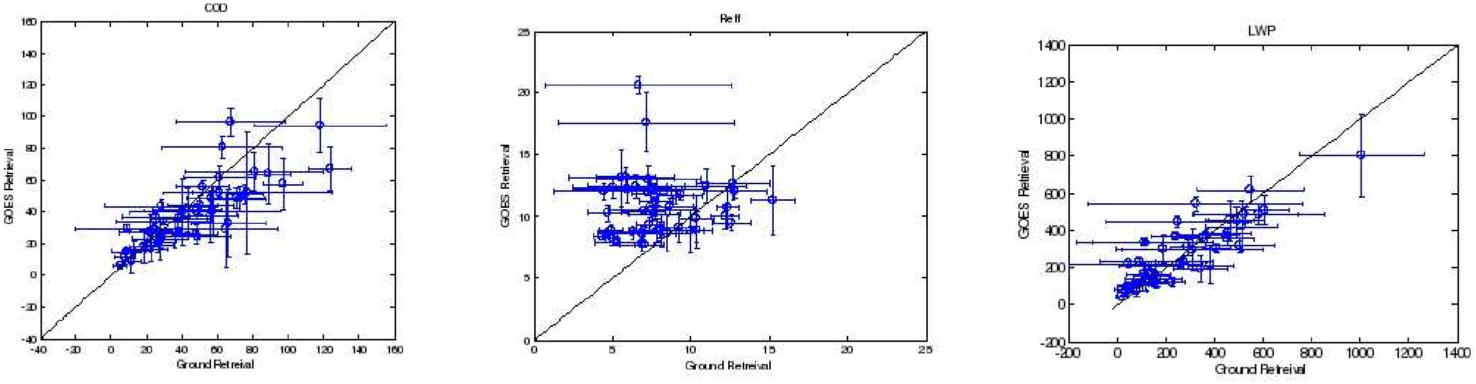

(a) (b) (c)

Figure 4.3: Statistical matchups between GOES VISST and ground retrieval for (a) COD (b) Reff (c) LWP.

The most striking observation is that the retrieval of the LWP and COD are much better than Reff. If we look at the sensitivity plot Figure 4.1, accurate retrieval of Reff is mainly due to accurate calibration of the 3.9 um IR channel which is known to improve significantly as more recent GOES sensors and better calibrations were implemented.

Clearly, it is of interest to assess the satellite performance as later algorithm / satellite platforms were implemented. The holdings for the VISST cloud data are given in Figure 4.4. The pixel level datasets are given at 4km resolution which is commensurate with the MFRSR FOV. In choosing the pixels for the matchups, we make use of the following conditions

1. Only those cases where number of water phase cloud pixels in the 5 x 5 box (20km resolution) is 15 are used.

2. The variability (standard deviation) of the cloud properties < 30

3. IR brightness temperature flags for 10.8 um channel > 255K.

The most important observation is that although the COD retrievals are fairly robust over all solar zenith angles especially for COD < 50, the effective radius shows very strong bias and poor correlation to ground retrievals when $\theta_{sun} > 50$ degrees. Specifically GOES retrieved R_{eff} is larger than ground retrieved R_{eff}. When solar zenith angle θ_{sun} is greater than 50 degrees, effective cloud optical depth also becomes larger. For this reason, photons incident on a water cloud are likely to be reflected back to satellite from an upper part of the cloud without penetrating into a lower part of the cloud. On the other hand, photons incident on a cloud transmit through the whole layer to the ground, whether effective cloud optical depth is thin or thick. Many researchers [Curry, 1986, Garrett and Hobbs, 1995, Nicholls and Leighton, 1996, Noonkester, 1984, Slingo et al., 1982, Stephens and Platt, 1987] reported that cloud droplet effective radius increases from cloud base to cloud top, as illustrated schematically in Figure 4.5

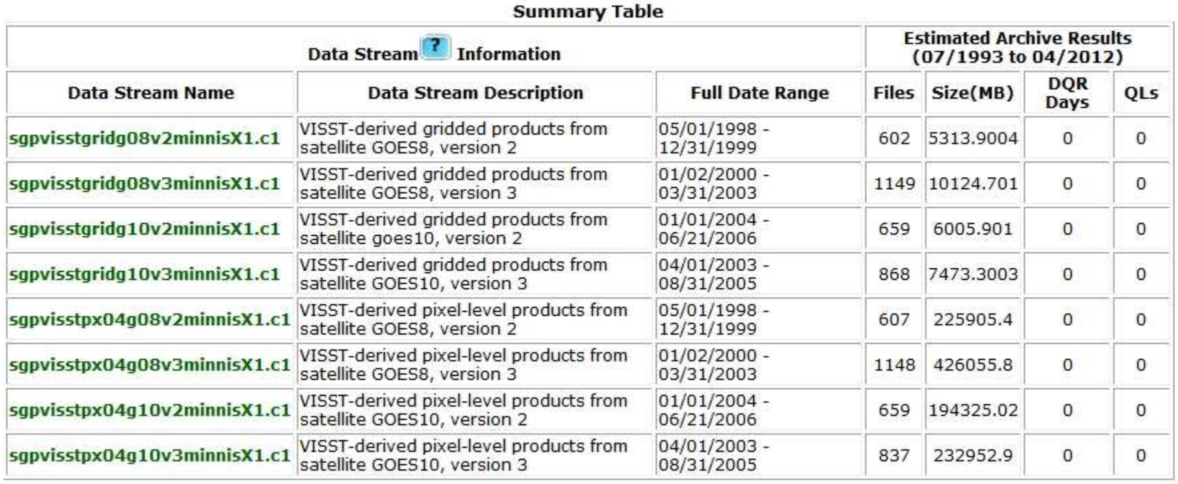

Summary Table

Data Stream Information			Estimated Archive Results (07/1993 to 04/2012)			
Data Stream Name	**Data Stream Description**	**Full Date Range**	**Files**	**Size(MB)**	**DQR Days**	**QLs**
sgpvisstgridg08v2minnisX1.c1	VISST-derived gridded products from satellite GOES8, version 2	05/01/1998 - 12/31/1999	602	5313.9004	0	0
sgpvisstgridg08v3minnisX1.c1	VISST-derived gridded products from satellite GOES8, version 3	01/02/2000 - 03/31/2003	1149	10124.701	0	0
sgpvisstgridg10v2minnisX1.c1	VISST-derived gridded products from satellite goes10, version 2	01/01/2004 - 06/21/2006	659	6005.901	0	0
sgpvisstgridg10v3minnisX1.c1	VISST-derived gridded products from satellite GOES10, version 3	04/01/2003 - 08/31/2005	868	7473.3003	0	0
sgpvisstpx04g08v2minnisX1.c1	VISST-derived pixel-level products from satellite GOES8, version 2	05/01/1998 - 12/31/1999	607	225905.4	0	0
sgpvisstpx04g08v3minnisX1.c1	VISST-derived pixel-level products from satellite GOES8, version 3	01/02/2000 - 03/31/2003	1148	426055.8	0	0
sgpvisstpx04g10v2minnisX1.c1	VISST-derived pixel-level products from satellite GOES10, version 2	01/01/2004 - 06/21/2006	659	194325.02	0	0
sgpvisstpx04g10v3minnisX1.c1	VISST-derived pixel-level products from satellite GOES10, version 3	04/01/2003 - 08/31/2005	837	232952.9	0	0

(a)

Summary Table

Data Stream Information			Estimated Archive Results (07/1993 to 04/2012)			
Data Stream Name	**Data Stream Description**	**Full Date Range**	**Files**	**Size(MB)**	**DQR Days**	**QLs**
sgpvisstgridg11v3minnisX1.c1	VISST-derived gridded products from satellite GOES11, version 3	06/21/2006 - 06/30/2011	1836	16202.202	0	0
sgpvisstgridg11v4minnisX1.c1	VISST-derived gridded products from satellite GOES11, version 4	07/01/2011 - 11/30/2011	151	1363.3999	0	0
sgpvisstpx04g11v3minnisX1.c1	VISST-derived pixel-level products from satellite GOES11, version 3	06/21/2006 - 06/30/2011	1836	540827.4	0	0
sgpvisstpx04g11v4minnisX1.c1	VISST-derived pixel-level products from satellite GOES11, version 4	07/01/2011 - 11/30/2011	151	45546.797	0	0

Note:

(b)

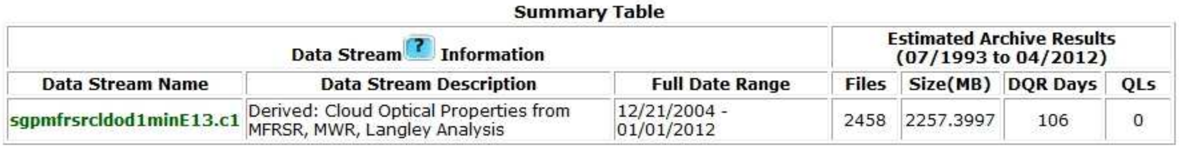

Summary Table

Data Stream Information			Estimated Archive Results (07/1993 to 04/2012)			
Data Stream Name	**Data Stream Description**	**Full Date Range**	**Files**	**Size(MB)**	**DQR Days**	**QLs**
sgpmfrsrcldod1minE13.c1	Derived: Cloud Optical Properties from MFRSR, MWR, Langley Analysis	12/21/2004 - 01/01/2012	2458	2257.3997	106	0

(c)

Figure 4.4: DOE ARM site data archive holdings for cloud / ground retrieval comparison (a) GOES 8/10 (b) GOES 11 (c) MFRSR.

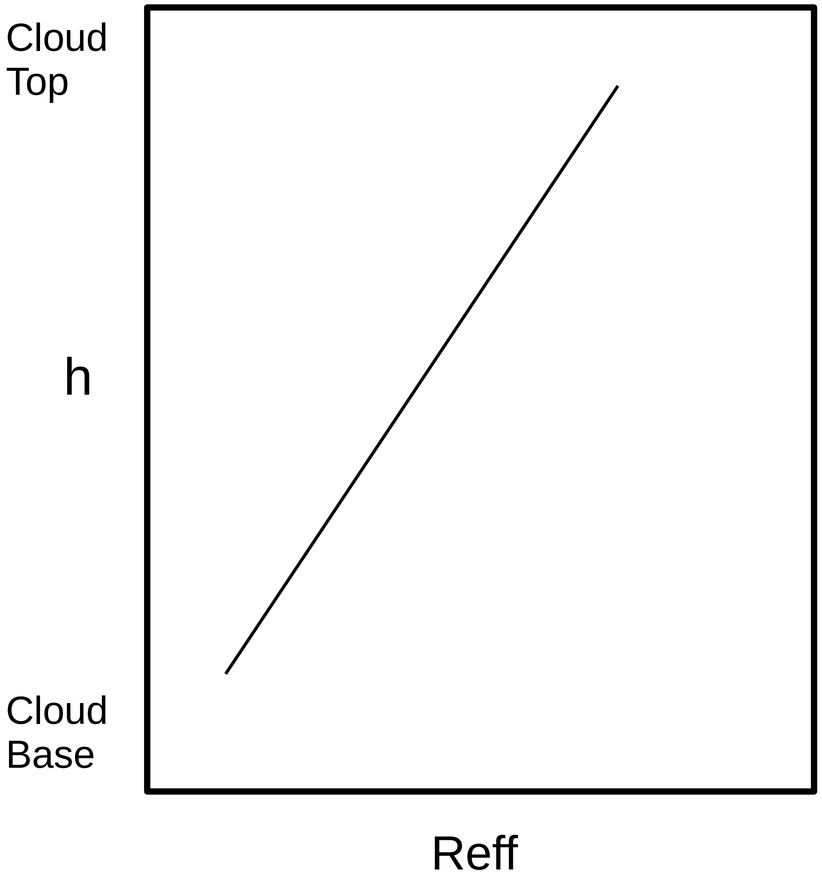

Figure 4.5: Schematic diagram of cloud droplet effective radius Reff vs. height h in a water cloud.

Chapter 5

Ground based approach

5.1 Instrumentation and data processing

In the present study, we focus on the measurements from the ground based radiometers, namely, Multi-Filter Rotating Shadowband Radiometer (MFRSR, Model: MFR-7, Yankees Environmental Systems Inc.) shown in Figure 5.1 and profiling Microwave Radiometer (MWR, Model: MP-3000A, Radiometrics) shown in Figure 5.2 for cloud retrievals. It should be pointed out that the MP-3000A at CCNY is an advanced radiometric system in comparison to the existing 2 channel MWR deployed at the ARM site. Therefore, it is expected that some additional improvements in the MWR performance of the LWP can be obtained.

The MFRSR is a seven channel radiometer with six passbands of 10 nm FWHM (Full Width Half Maximum) centered at 415, 500, 615, 670, 870 and 940 nm and an unfiltered Si broadband (300-1100 nm) channels. It uses an automated shadowbanding technique to measure the total-horizontal (global), diffuse-horizontal, and direct-normal spectral irradiances through a single optical path [Harrison et al., 1994, Min and Harrison, 1996a]. The global

Figure 5.1: Multifilter Rotating Shadowband radiometer (MFRSR).

Figure 5.2: Microwave Radiometer, Model: MP-3000A.

and diffuse components are measured directly. And the direct-normal component is computed from the difference of the two measured components. MFRSR takes measurements at four different shadowband positions to collect a single record. The first measurement is taken with the shadowband in the nadir (home) position. The next three measurements are, in sequence, the first side-band, sun-blocked, and the second side-band. The side-band measurements are used to correct for the portion of the sky obscured by the shadowband. An automated, microprocessor-controlled shadowband is used to alternately shade and then expose the entrance aperture of the instrument, allowing for the measurement of the three solar radiation components. Each record is available in short intervals (of 15 seconds) and integrated into one minute averages throughout the day. The diffuse and global irradiance measurements are guaranteed to have the same passband and sensitivity as the direct-normal irradiances. Accuracies are demonstrated in comparison with other tracking instruments for the direct-normal component (and thus optical depths), and they are superior to those of existing Lambertian radiometers for the diffuse-horizontal and total-horizontal irradiances. On a clear day, most of the solar radiation received by a horizontal surface will be direct-normal irradiance, while on a cloudy day most will be diffuse-horizontal irradiance. Observations of atmospheric irradiance (direct, diffuse and global) under overcast skies by MFRSR provide the potential capability to infer cloud transmittance or the COD.

An automated MFRSR data processing algorithm developed at NASA GISS by Alexandrov et al., [2002] with cloud screening procedure [Alexandrov et al., 2002] is used for aerosol retrieval as well as calibration. In our application, the calibration is crucial since the cloud properties are determined radiatively from a diffuse transmission which can only be obtained from the diffiuse irradiance if calibrated. In the GISS method we applied to the CCNY system, the calibration independent direct to diffuse ratio was used in the regression analysis (minimum airmass range for regression is taken as 0.1) to enhance the stability of regression and decrease the noise in the retrieved calibration coefficients when compared to traditional Langely technique. Since, this method is applicable at different sensitivities to atmospheric stability; it takes care of data for which Langley regression fails. Thus, more observational data is included in the determination of the calibration coefficients. Most notable aspect about this MFRSR processing algorithm is that both calibration and retrieval procedures are not separated, while the traditional retrievals [Holben et al., 1998, Schmid et al., 1997, 1998] require prior determination of calibration constants (through a calibration procedure) and applied to the data. In this approach, contributions due to different physical parameters (such as aerosol extinction, gaseous absorption) into total optical depths are separated first and then calibration is applied independently. Thus calibration errors in one parameter do not affect the accuracy of the other retrievals.

To improve consistency over long time periods, the NASA GISS algorithm is applied simultaneously to a set of daily datasets covering at least a month (or maximum 4 months) of measurements through a sequential set of procedures: first all days are cloud screened, and then all 870 nm records are calibrated using compatibility between the direct and diffuse measurements. This approach allows for stabilization of the daily calibration constants at each level using a robust smoothing technique. Internal coefficients are instantaneous, derived for each day (using direct to diffuse ratio and size-regression methods) independently from other days, while the external coefficients result from averaging (smoothing) and/or interpolation of time series of internal coefficients over a long period (default $\sim$ 4 months). These external coefficients are the ones ultimately used to compute the top-of-atmosphere (TOA) irradiance. In the code, the measured irradiance is divided by a nominal TOA irradiance value, I_0, and calibration constant, $C = exp(-c)$, where c is the external calibration coefficient providing correction to it. Thus, the TOA irradiance value, equivalent to that of Langley regression, is given by $I_0 = exp(-c)$.

Atmospheric transmittances can be subsequently calculated under cloudy conditions as the ratio of the uncalibrated output to the extrapolated TOA value. The diffuse and total components of solar irradiance reaching the surface will be equal when optically thick cloud conditions prevail. So, atmospheric transmittance implies to the ratio of one of these components to the TOA irradiance value.

In order to obtain simultaneously both the cloud optical depth and cloud droplet effective radius of the prevailing thick clouds, we require an additional measurement which can give the total liquid water content in the cloud layer, termed as liquid water path, in the zenith direction which is the main function of the MWR. In particular, both column integrated precipitable water vapor (PWV) and cloud liquid water path (LWP) defined as

$$PWV = \frac{1}{\rho_{wt}} \int \rho_v(z) dz \tag{5.1}$$

$$LWP = \frac{1}{\rho_{wt}} \int w(z) dz \tag{5.2}$$

where ρ_{wt} is the density of liquid water, $\rho_v(z)$ is the vertical distribution of water vapor density and $w(z)$ is the vertical distribution of cloud liquid water content. Here we express PWV in cm and LWP in gm^{-2}.

The profiling Microwave Radiometer (MWR) contains two radio frequency (RF) subsystems sharing the same antenna and antenna pointing system in the same cabinet. The water vapor profiling subsystem utilizes sky brightness temperature observations at selected frequencies between 22 and 30 GHz (21 channels). The temperature profiling subsystem utilizes sky brightness temperature observations at selected frequencies between 51 and 59 GHz (14 channels). The profiler makes use of atmospheric radiation measurements in the RF domain and provides high resolution vertical profiles of temperature, humidity, water vapor and low resolution profiles of liquid density at 58 altitude levels, starting with 50 m steps from the surface up to 500 m, then 100 m steps to 2 km, and 250 m steps from 2 to 10 km. In addition, surface relative humidity, temperature and barometric pressure measured by the radiometer are used in the determination of profiles. An internally mounted and vertically pointed Infrared Thermometer (IRT) indicates the presence of cloud, and measures cloud base temperature, if clouds are present. Knowing cloud base temperature yields the vapor density at cloud base (at saturation), and when combined with the retrieved temperature profile, yields cloud base altitude. These physical measurements are important constraints for profile retrieval. Neural networks (site specific) derived using the Stuttgart Neural Network Simulator and long-term record of radiosonde profiles are provided by Radiometrics. A standard back-propagation algorithm was used for training and a standard feed-forward network is used for profile determination. Although the number of independent measurements (Eigenvalues) are less than the 58 retrieved layers, the finer resolution provides better displays and easier processing in subsequent data processing steps. In our application, we are interested mainly in the LWP but validation of this parameter is very difficult in the absence of aircraft measurements. Therefore, efforts to assess performance of the MWR are mainly accomplished using PWV. As an example, we can compare the MWR-PW performance against the PWV derived from the AERONET radiometer water vapor channel.

The comparison of integrated column water vapor from MWR and AERONET for clear

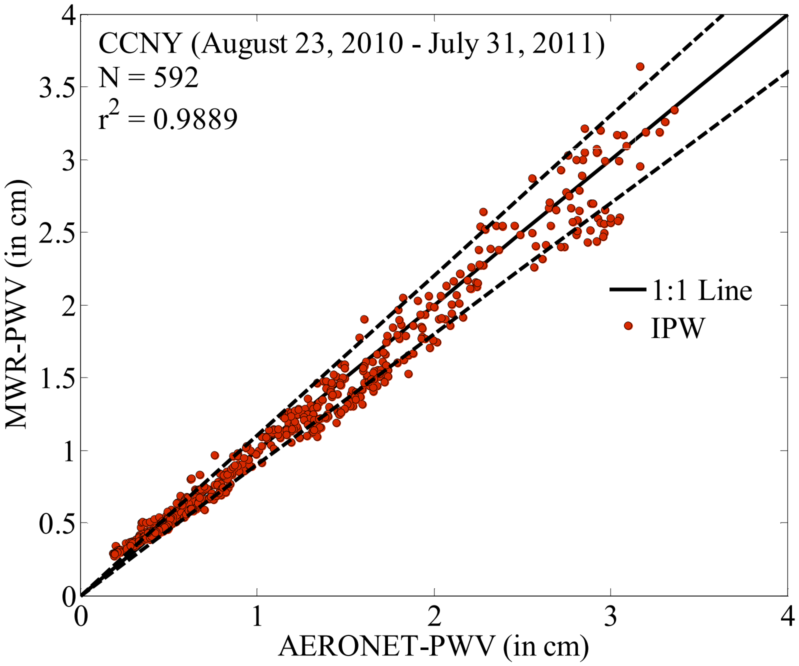

Figure 5.3: Comparison of hourly averaged precipitable water vapor from MWR and AERONET at CCNY (for clear sky condition) during August 23, 2010 and July 31, 2011.

sky observations over CCNY is shown in Figure 5.3.

The PWV from MWR indicate that except for very low cases in winter, the results are unbiased with errors $< 10\%$.

In order to illustrate the improvements we have by using the MP3000A against the SGP 2 channel WVP-1500 radiometer, we have made some cross validations against the two instruments against existing radiosondes and AERONET at the Brookhaven National Laboratory (BNL) as part of an overall calibration exercise. The results are given in Figure 5.4 for the 2 days when all measurements are available.

For both days, the MP3000A was a better match against the AERONET retrievals then the WVP-1500. In addition, there is clear improvement (especially for day 2) in the com-

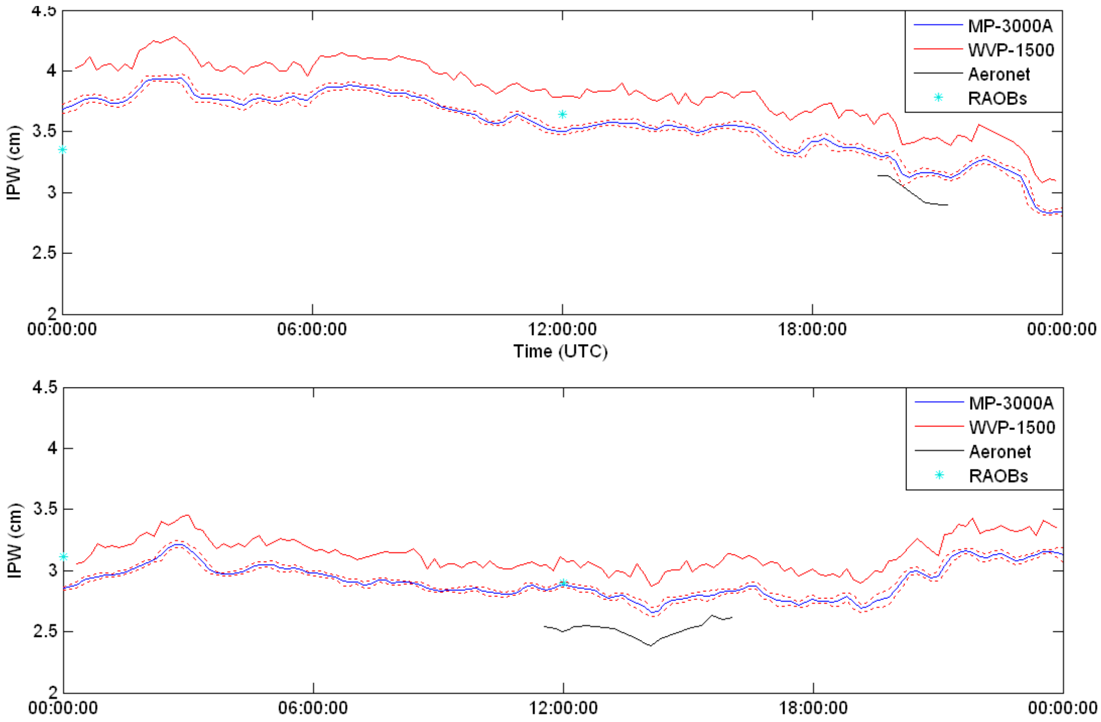

Figure 5.4: Integrated precipitable water vapor comparison. Red line represents the interval of confidence for the MP-3000A dataset based solely on temporal fluctuation of retrieval a) 09/10/11 b)09/11/11

parisons against the Radiosonde launches. This comparison illustrates the fundamental superiority of the MP-3000A system which undoubtedly points to improvements in the LWP retrieval as well.

5.2 Development of cloud retrieval algorithm

Of the various ground based cloud retrieval techniques, the most extensively used and reference approaches for measurements from MFRSR-MWR system is the Nonlinear Least Squares retrieval algorithm of Min and Harrison [1996a], hereafter referred as MIN, is based on the parameterization of scattering properties at 415 nm on the effective radius and LWP using Mie theory. MIN uses an adjoint formulation of the radiative transfer [Min and Harrison, 1996b] to maintain accuracy and improve its execution speed. In this approach, traditional Langley regression of the direct-normal irradiance taken on clear stable days are used to extrapolate the MFRSR's response to the TOA [Harrison et al., 1994], and this calibration is applied to the total-horizontal irradiance. The MIN method is applied to measurements of atmospheric transmittance at 415 nm band because this band is completely insensitive to absorption by ozone and by permanent atmospheric gases, and the surface albedo is low and stable for natural surfaces (except for snow-covered surfaces). Moreover, for this wavelength, both the asymmetry parameter and the single scattering albedo (close to unity) show little discrepancy on droplet size. In another approach, Matamoros et al., [2011] builds a parameterized regression based inversion of a radiative transfer model hereafter referred as PAR based on the assumption of a fixed rural background aerosol mode for SGP ARM site. The parameterization based on regression fitting from the RT simulations is given by

$$\tau_c = \frac{1+r_e}{(1+0.4125r_e)}\frac{1}{(1-r_g)}[(P_1\mu_0+P_2)\frac{1}{T}+P_3-\frac{0.007}{T^2}] \tag{5.3}$$

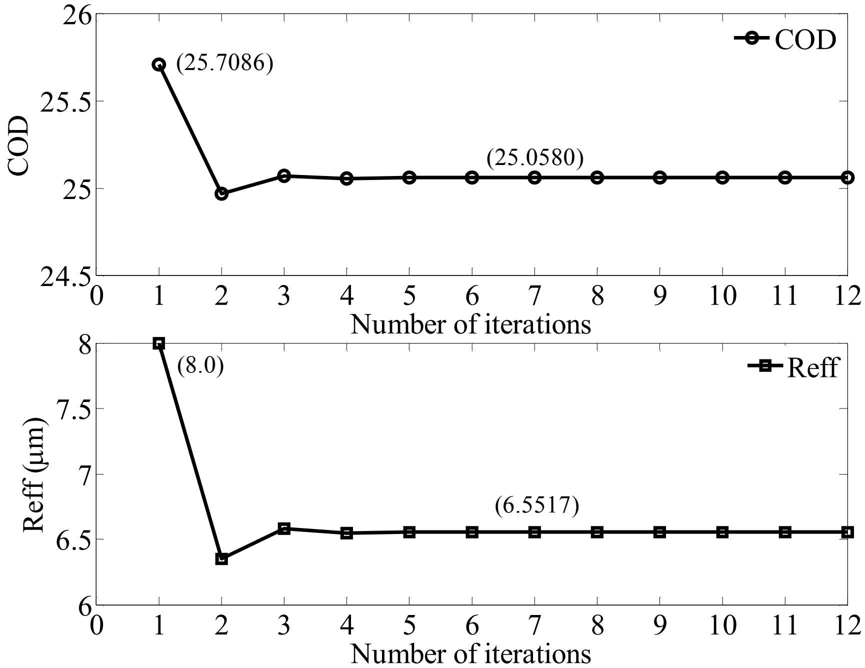

Figure 5.5: Convergence of iterative retrieval algorithm.

where $P1 = -0.4330AOD + 3.6659$, $P2 = -0.7686AOD + 2.0895$, $P3 = -0.1986AOD - 5.7936$. Here μ_0 is the cosine of the solar zenith angle, T is the atmospheric transmittance, r_g is the surface albedo at 415 nm, τ_c and r_e are the visible COD and droplet effective radii. The linear dependence of P1, P2 and P3 with AOD agrees for AOD ranging from 0 to 0.2. Also, this method points out that AOD has an effect in the retrieval of cloud properties, but was unable to prove that by introducing AOD improves the agreement between the retrieved properties and the true (and unknown) values of COD and Reff. Of course, this approach can be extended to more regional realistic aerosol models for different locations as needed.

In our analysis, we closely follow the MIN algorithm but instead of a LSQ optimization, we develop an iterative inversion approach. The schematic of our LUT based iterative approach for cloud optical properties of thick clouds is shown in Figure 5.5. This iteration approach forms the basis of our retrieval algorithm, hereafter referred to as RET. Initially, Reff is fixed at 8 μm and the first estimation COD from the LUT is obtained. Then $Q_{415nm}(Reff)$ is estimated from Equation 5.5 assuming again Reff = 8 μm. Subsequently, by introducing the MWR measured value of LWP (i.e., LWP_{meas}), Equation 5.4 is used to obtain better estimation of effective radius (Reff), which will again obtain a better estimate of COD using the LUT. This iteration procedure continues until stable values of COD and Reff (i.e., convergence of LWP_{theory} to LWP_{meas} occurs) are obtained for each of the atmospheric transmittance measurement. To implement efficiently, initial 2D LUT's are developed for the LWP and diffuse transmittance and interpolation is used when readjusting Reff during the retrieval. By following the MIN approach, we can verify the results directly against the SGP database. In order to retrieve cloud optical properties of thick water clouds, we require real-time measurements of atmospheric transmittance (for 415 nm wavelength) as a function of cosine of solar zenith angle (μ_0) from MFRSR, and LWP from MWR as well as estimated of aerosol loading and surface al. Santa Barbara DISORT Atmospheric Radiative Transfer (SBDART) [P.Ricchiazzi et al., 1998] model, which is based on DISORT algorithm for discrete ordinate radiative transfer in multiple scattering and emitting layered media [Stamnes et al., 1988], is used for computing the radiation fluxes at the surface and at the TOA. In terms of SBDART, atmospheric transmittance is defined as the ratio of downwelling irradiance at the surface to that at the TOA for a narrow wavelength band corresponding to MFRSR. We define site specific aerosol model based on the long-term climatological record of AERONET Level 2 datasets. The aerosol climatology parameters include aerosol optical depth, single scattering albedo and asymmetry parameter spectrally covering the shortwave region. Also, the climatological surface albedo value is chosen from the ASRVN (AERONET Surface Reflectance Validation Network) data record. SBDART treats atmosphere as a plane parallel system, so vertical inhomogeneities of the atmosphere and the aerosol distribution can be taken into account. Given the fixed the aerosol model, surface albedo, atmospheric model (US62 Standard Atmosphere), an LUT for inverse of atmospheric transmittance (T^{-1}) can be computed by varying the COD, Reff and μ_0 together in the radiative transfer code. From the LUT, as expected, the linearity of the relationship between COD and T^{-1} is observed and their slope is dependent on μ_0, while the intercept is almost independent. Figure 5.6 shows the schematic of the algorithm. Here LWP_{meas} represents the real-time instantaneous liquid water path measurement from MWR and the order (or number) of iteration is denoted by 'n' as subscript to the variable terms.

In implementing the algorithm, we utilize a relationship between COD, Reff and LWP, assuming a size distribution $n(r)$ of droplets with radius r and with an effective radius Reff, given by

$$COD = \frac{3Q_{\lambda}(R_{eff})LWP}{4\rho_w R_{eff}} \tag{5.4}$$

where ρ_w is the water density and $Q_{lambda}(Reff)$ is defined as the weighted extinction efficiency by the droplet size distribution. For $\lambda = 415nm$ and for modified gamma size distribution with width $p = 7$ [P.Ricchiazzi et al., 1998], the weighted extinction efficiency can be approximated by

$$Q_{415nm}(R_{eff}) = 2.00196 + 0.36411 R_{eff}^{-0.70043} \tag{5.5}$$

which is only a slight correction to $Q_{415nm}(R_{eff}) \approx 2$ which yields the simple and often

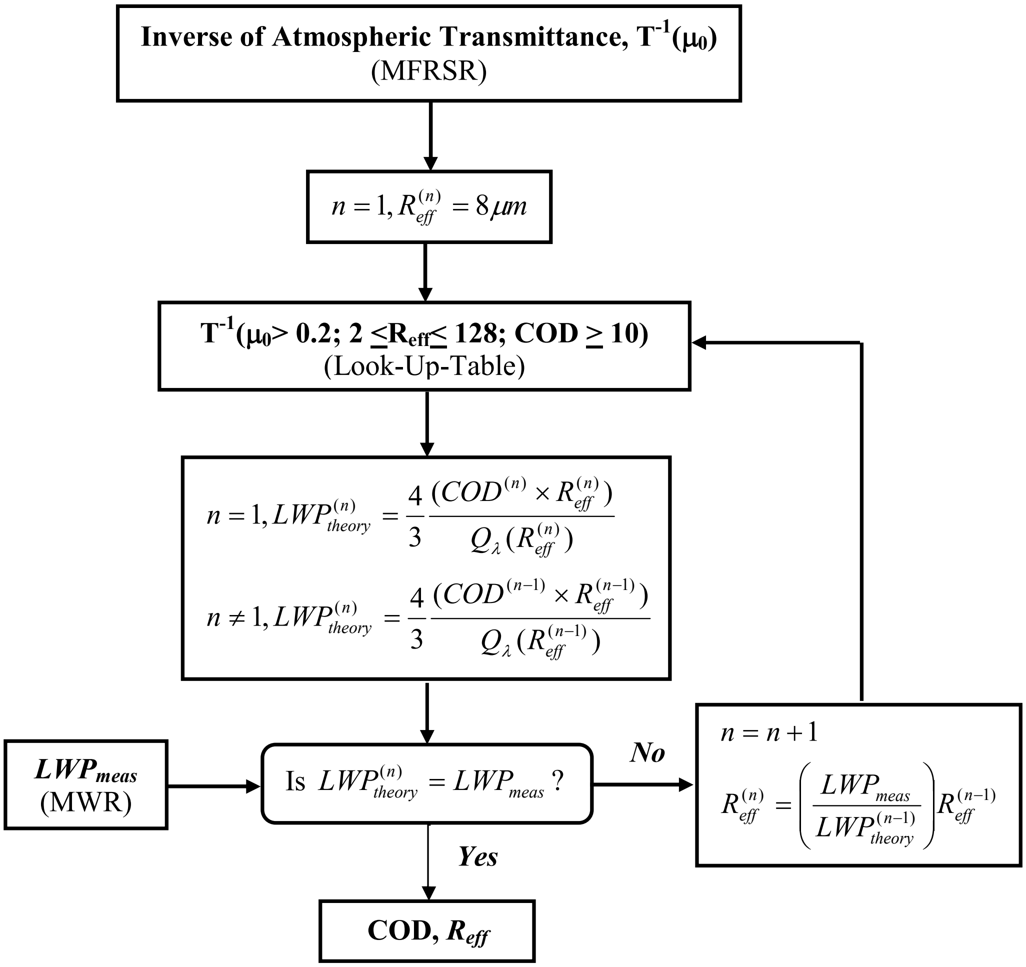

Figure 5.6: Schematic of the Look-Up-Table based iterative approach for retrieving cloud optical properties of thick water clouds using MFRSR measurements.

used result

$$COD = \frac{3LWP}{2\rho_w R_{eff}} \tag{5.6}$$

5.3 Intercomparison of cloud retrievals at SGP

In an effort to better assess the performance of the ground retrievals, we look to compare our retrievals against both the existing algorithms (MIN, PAR), which have basically similar underlying mathematics, as well as comparisons against Dong et. al. [1997, 2002] which has a fundamentally different approach consisting different instrumentation.

5.3.1 Comparison with Min's MFRSR retrieval

At SGP ARM site, the Microwave Water Radiometer (MWR, Model WVR-1100) measures column-integrated amounts of water vapor and liquid water. This MWR receives microwave radiation from the sky at duel frequencies (23.8 GHz and 31.4 GHz), which allow simultaneous determination of total water vapor and liquid water burdens along the selected path. In the present study, we have taken utmost care for excluding the LWPs recorded during precipitation from our analysis. Various studies have reported uncertainties in LWP retrievals to be around ∼ 20-30 gm^{-2}

Existing cloud optical properties from MFRSR are obtained using MIN algorithm within the SGP Value Added Product (VAP) called MFRSRCLDOD [Turner et al., 2004]. We use the atmospheric transmittance as a function of cosine of solar zenith angles for thick cloud cases along with instantaneous LWP measurements from MWR, which are available in the VAP. Cloud retrievals from our approach (RET) are compared with MIN retrievals and parameterization (PAR) scheme are shown as scatter plots in figure 6 for the period covering April to September, 2008. COD retrievals from our approach show excellent correlation (r2 $\sim$ 0.99) and consistency with those obtained from both the methods and this is maintained over large datasets. However, we note that there is a spread or discrepancy in the retrieved Reff from RET approach which is mainly due to the difference in LWP measurements used by MIN algorithm. So, for similar instantaneous LWP measurements the PAR approach clearly shows consistency throughout.

The uncertainty in the retrieved COD is mainly dominated by the uncertainty in the instrument calibrated TOA irradiance value, while the uncertainty in the LWP is evident in the effective radius uncertainty. In Figure 5.5, our retrievals are limited to instantaneous LWP values. In order to avoid the spatial inhomogeneities in the cloud which affect the diffuse irradiance field, VAP provides both "instantaneous" retrievals at nominal 20 seconds resolution of the MFRSR and "average" retrievals where the data have been averaged for 5 minutes centered upon the output sample run. Metamoros et al. [2011] obtained maximum relative deviations of 5% and 8% for cloud optical depth and effective radius, respectively, when compared with the MIN retrievals at ARM SGP site. In understanding this discrepancy, we note that the MIN retrievals are based on an internal estimation of 5 minute averaged LWP and the details of that averaging are not accessible. Therefore, when we perform an averaging procedure, it may not be identical to the approach that MIN uses. To test this, we perform in Figure 5.8 a closure study where the MIN retrieval products are used to "derive" the LWP (MIN-DER) which are compared to the Averaged LWP. The discrepancy is on the same order of magnitude of the errors in Reff observed illustrating that there is ambiguity in how the Average was calculated. The sensitivity is further demonstrated where the instanta-

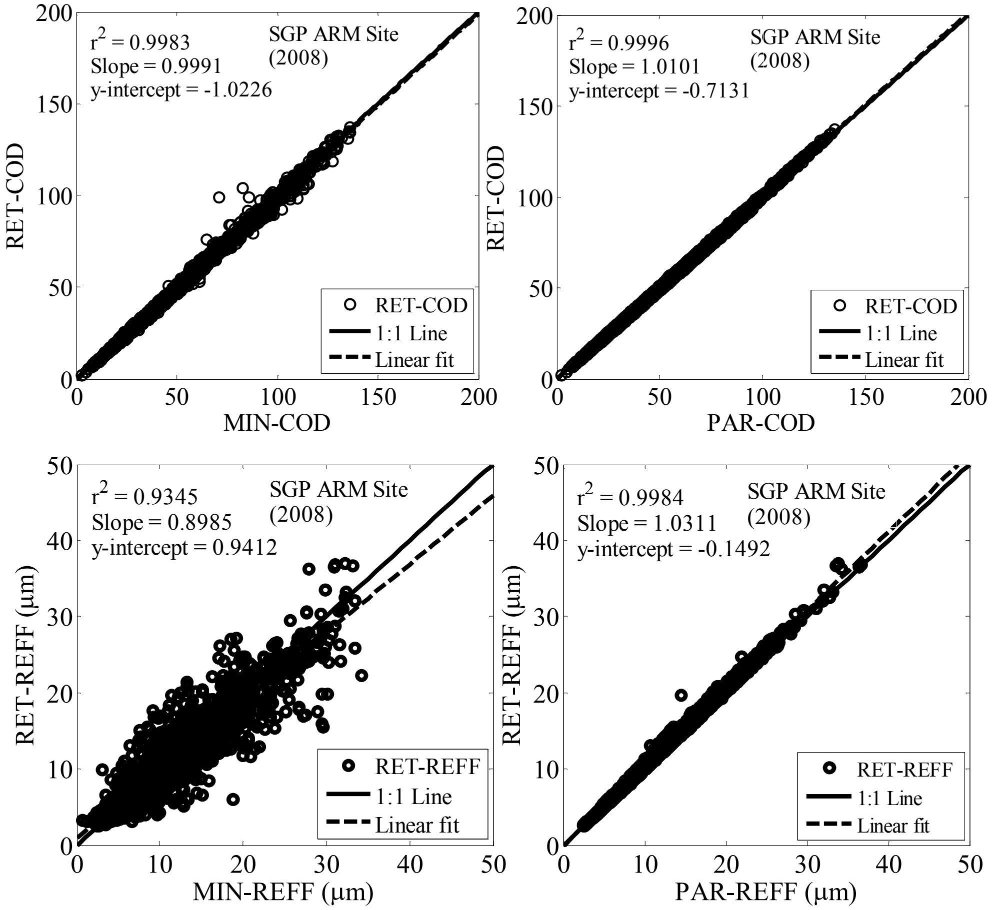

Figure 5.7: Scatter plot between retrieved instantaneous COD and Reff using RET approach to those of MIN (top left and bottom left) and PAR retrievals (top right and bottom right)

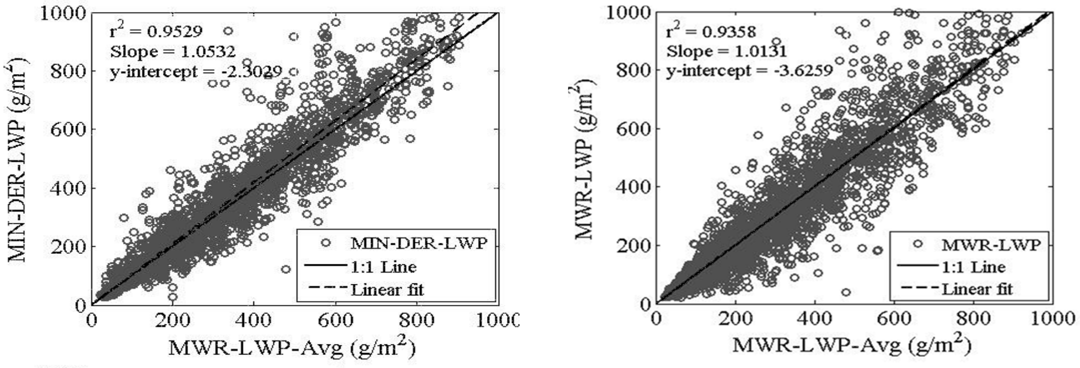

Figure 5.8: Regression plot between LWP derived in different ways a) closure comparison between averaged measured and derived LWP (left) b) averaged vs. instantaneous LWP (right).

neous LWP is compared to the averaged LWP demonstrating comparably higher variability.

5.3.2 Comparison with Dong's ground retrieval approach

It is also important to compare our cloud retrieval results against a mathematically different approach which utilizes a combined measurements of Precision Spectral Pyranometer as well as MWR [Dong et al., 1997]. Dong et. al. [1997, 2002] demonstrated the method to retrieve cloud microphysical properties as well as shortwave radiative properties by using 2-stream radiative transfer model in conjunction with the ground based measurements.

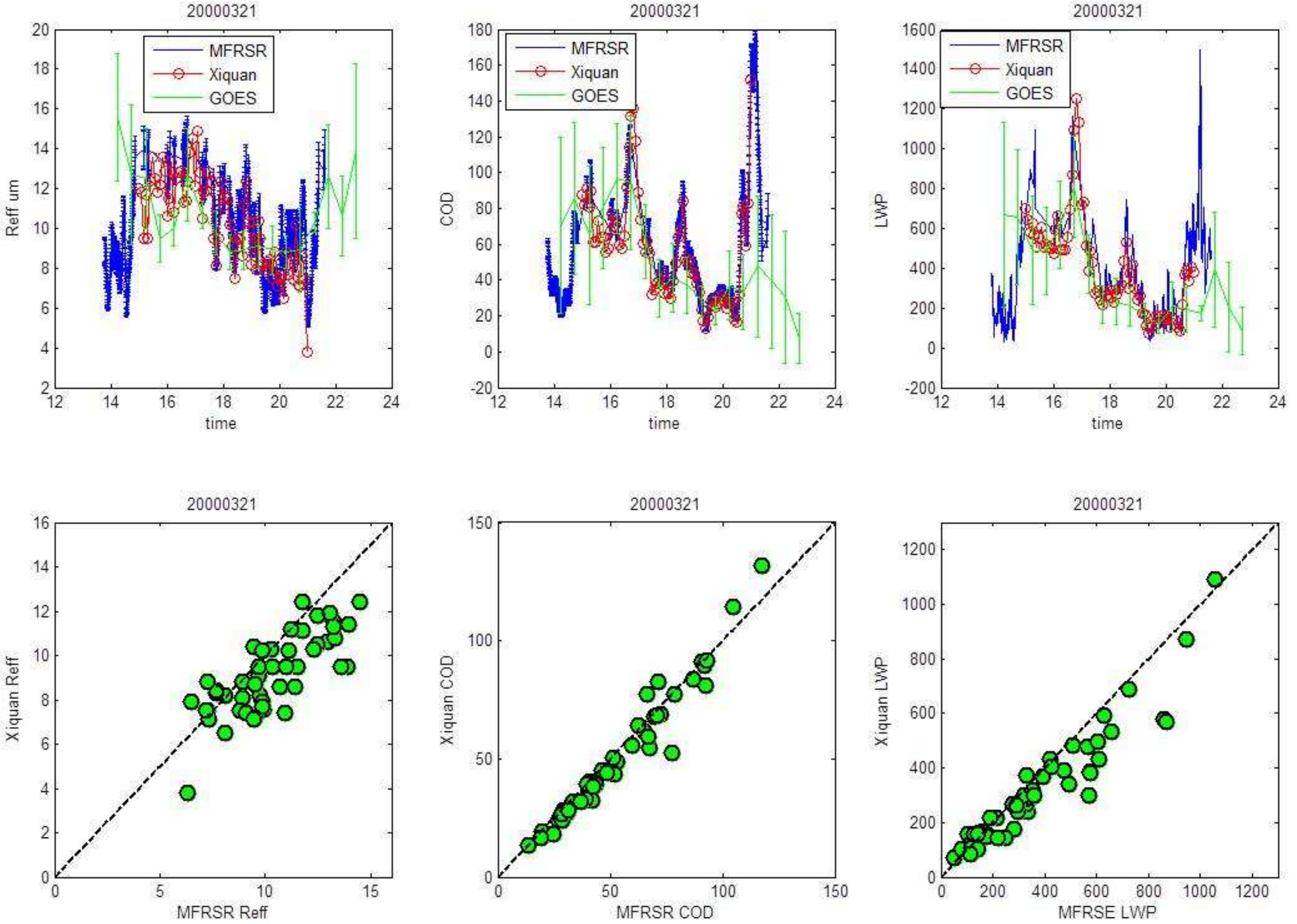

Figure 5.9: Comparison of cloud optical properties between our retrieval and Dong's retrieval at SGP site. Top row is the time series comparing ground and satellite retrievals of Reff, COD, and LWP from left to right. The bottom row shows the regression between ground retrievals for Reff, COD, and LWP from left to right.

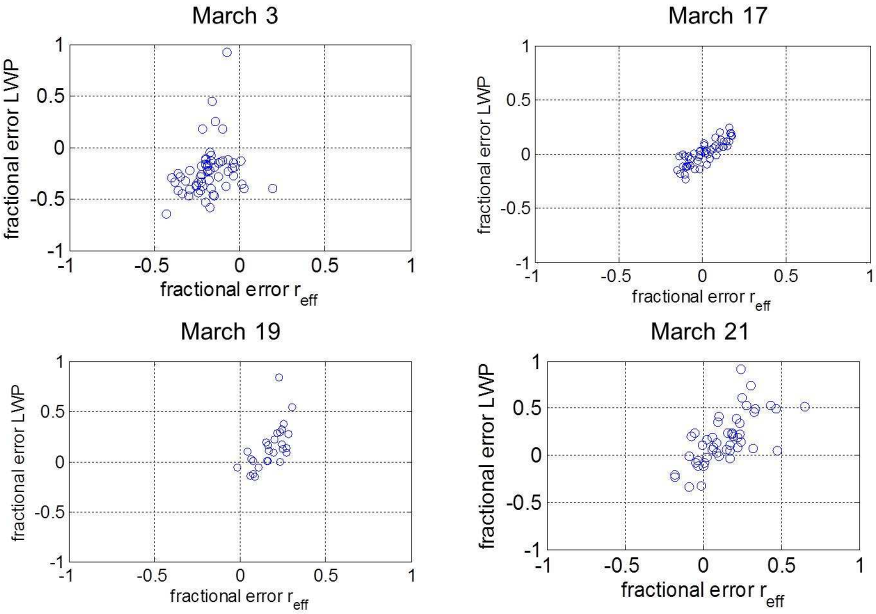

Figure 5.10: The correlation between LWP and Reff.

In Figure 5.9, we note the general agreement between our method and that in [Dong et al., 1997], although small biases are seen predominately in Reff. However, we also not that biases are also observed in the MWR LWP further demonstrating the importance of the MWR LWP estimates and how the averaging is performed. This is further demonstrated in Figure 5.10 where the fractional bias errors for the Reff retrieval are compared to the LWP fractional error biases. The nearly 1-1 relationship is consistent with the underlying relation in Equation 5.4 when COD retrieval shows no bias.

5.4 Sensitivity of cloud retrieval

In order to assess the realistic errors in cloud retrievals, a sensitivity analysis is performed focusing on errors that may occur due to incorrect aerosol assumptions below the cloud as well as imprecise surface albedo. Other variables such as geometric cloud base and cloud extent are less important and will not be considered here. In performing this sensitivity analysis, the "reference" cloud properties should correspond to values which are most likely be influenced by aerosols within the aerosol-cloud interaction. Based on the cases considered by Feingold et al. [2003], the LWP measurements seem to be constrained to a reasonably low values around 120 gm^{-2} with effective radii near 6 μm. Using the approximate relationship of $LWP = (2/3)(R_{eff} * COD)$, a representative COD $\sim$ 30 can be obtained. We now limit the solar geometry, cloud altitude or thickness etc. and perform the following sensitivity analysis.

1) Fixing the surface albedo at 415 nm as the mean surface reflectance from the MODASVRN data, vary the atmosphere based on the aerosol data from AERONET to obtain an ensemble of LUTs.

2) Fixing the mean aerosol model, vary the surface based on this current data and collect the ensemble of LUTs Figure 5.11

Once the "reference" cloud state is determined, the variability of the atmosphere and surface albedo needs to be estimated. For the surface, we make use of the MODIS land surface product MODASRVN (accessed through Level 1 and atmosphere achieve and Distribution System, `http://ladsweb.nascom.nasa.gov/data/search.html`), which provides the best estimate of the surface albedo since it routinely ingests AERONET aerosol properties allowing for the most accurate surface estimate from satellite that can be made. Since the surface albedo is only retrieved at the MODIS land surface channels, and extrapolation is performed on the spectral albedo retrievals to the 415nm channel. In figure 11, the results of the retrievals over the period 2007-2008 are given. We note that although the surface albedo tends to be brighter in the CCNY (urban) area, the data spread (uncertainty) is

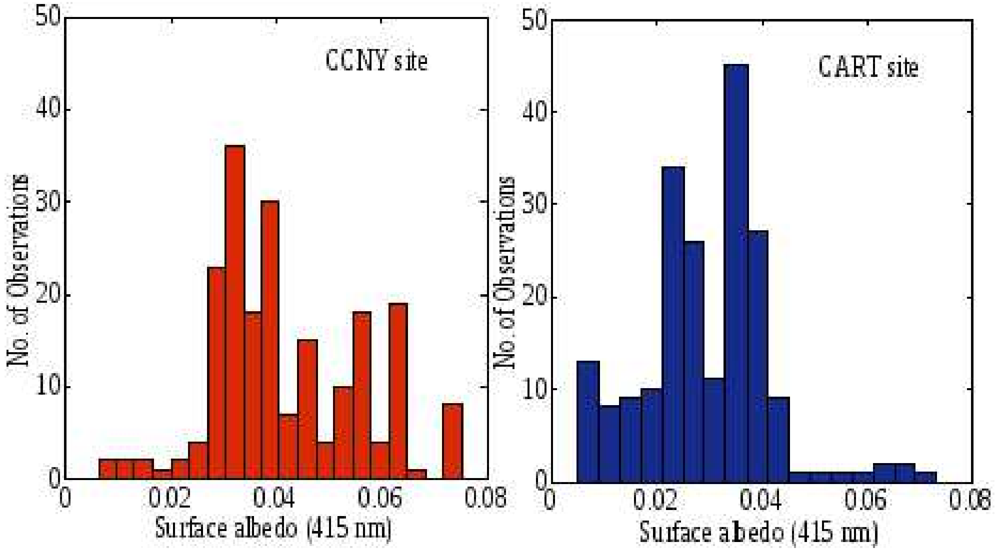

Figure 5.11: Statistics of 415 nm surface albedo using the MODASRVN retrieval for (a) CCNY site, and (b) CART site.

fairly similar with $\sigma_{CCNY} = 0.014$ in comparison to $\sigma_{SGP} = 0.012$. The aerosol properties on the other hand come from the microphysical retrievals of AERONET. In SBDART, the actual bimodal size distribution is not completely embedded but is approximated using the SSA (ω_0), asymmetry parameter (g) and AOD (τ). While this approximation may miss some fine properties, the main variability is mostly determined by these parameters. The statistics of these aerosol parameters is given in Figure 5.12 with the upper row displaying the CCNY retrieval statistics and the lower row displaying the SGP retrievals. Once the statistics of the atmospheric and surface parameters are obtained, we now perform the sensitivity analysis using the following procedure:

1. Determine the reference state where the cloud reference of COD = 30 and Reff = 6μm is used and the atmospheric and surface reference are taken to be the mean of the distributions.

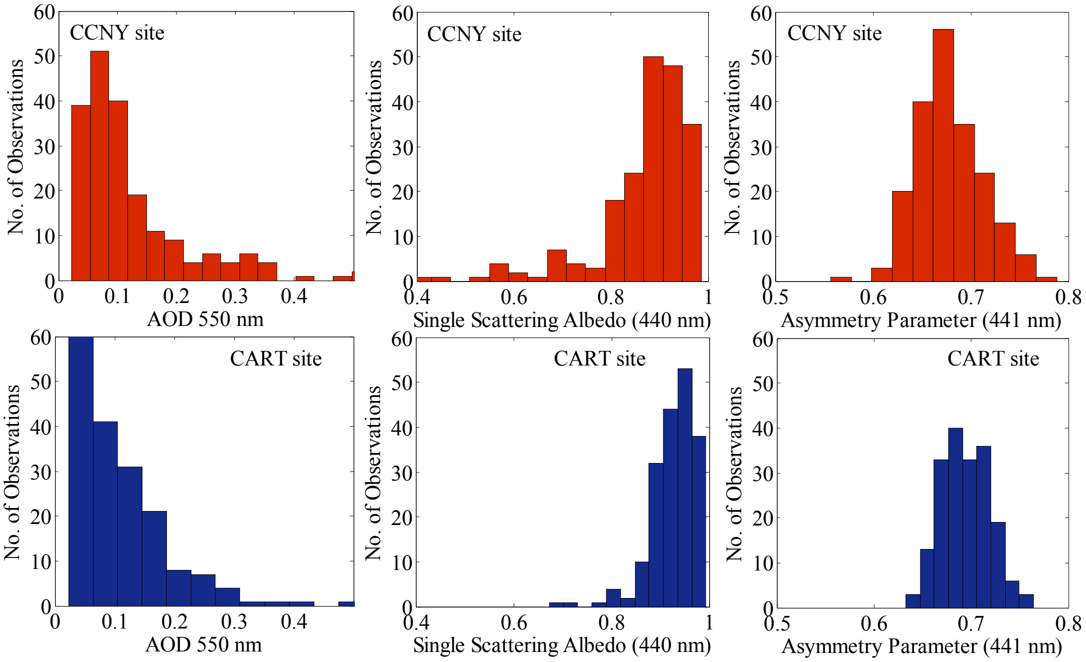

Figure 5.12: Statistics of the aerosol microphysical properties used within SBDART (a) CCNY site (top row) and (b) SGP site (bottom row).

2. Given this mean state, we obtain the LWP and diffuse transmittance obtained for this state (i.e., LWP_0 and $Tdiff_0$).

3. To assess the sensitivity of the aerosol, for example, we perform the retrieval for each admissible atmosphere with all other parameters (e.g. surface) taking on their mean values.

4. For each atmosphere, j, we determine the mean value of the retrieval based on the inversion of the LWP and diffuse transmittance LUT's constrained within

a. $LWP_0 - \Delta LWP < LWP_j(COD, Reff) < LWP_0 + \Delta LWP$

b. $T_0 - \Delta T < T_j(COD, Reff) < T_0 + \Delta T$

5. Determine the ensemble statistics based on the retrieval over all atmospheres

6. Repeat the steps 3 to 5 for the surface albedo uncertainties in this case letting the atmosphere take on the mean state.

Based on the above procedure, the statistics of the surface reflectance for CCNY and CART site are shown in Figure 5.13

While there is a small increase in the uncertainty in the retrievals for the CCNY site, the difference is compatible with the 15% differences we see in the uncertainty of the surface parameters. In particular, if we denote σ_s as the retrieval standard deviation of the effective radius retrieval due to surface albedo uncertainty, we observe $\sigma_s \approx 0.08\mu m$ or equivalently, a 1.3% fractional error which is clearly negligible in comparison to the 50% changes we expect in the dynamic range changes of Reff during the aerosol - cloud interaction.

$$\sigma_s = \sigma_a + \sigma_m \tag{5.7}$$

where σ_a is the retrieval uncertainty due to aerosol model uncertainty and σ_m is the retrieval uncertainty due to measurement uncertainty each estimated based on the description. The same exercise can be applied to the atmosphere variability. The results can be seen in

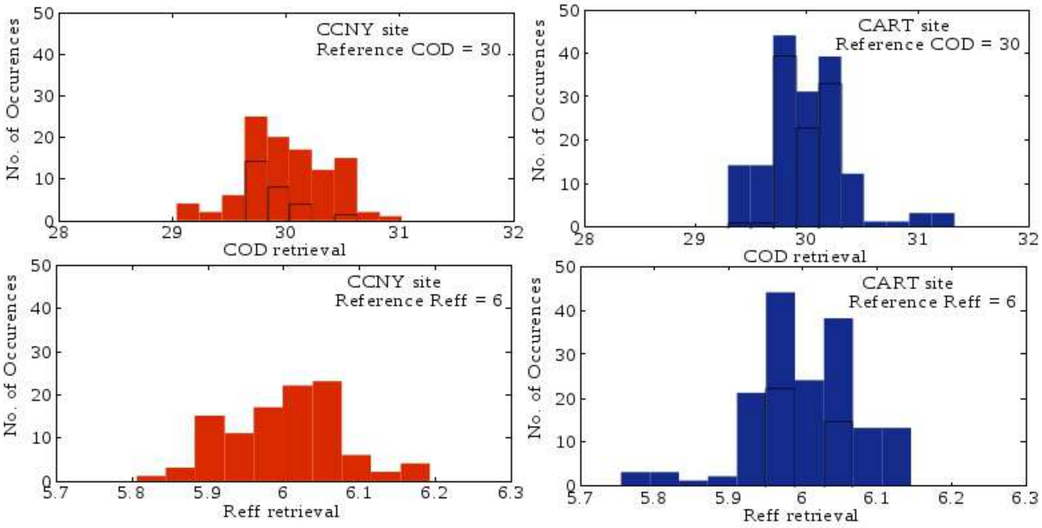

Figure 5.13: Cloud properties retrieval dispersion due to surface albedo uncertainty (a) CCNY site (b) ARM SGP (or CART) site.

Figure 5.14 for both the CCNY and SGP sites.

Clearly, the errors due to atmosphere variability is somewhat bigger with RMS errors of 3% occurring in the effective radius for the cart site while a 5% RMS error is seen at the CCNY site due to the significantly larger atmospheric variability. In addition, due to the non-linearity of the diffuse transmittance parameter on the cloud parameters, we note a significant bias of 5% in the overall retrieval. The above procedure provides an estimate of the uncertainties due to the model assumptions. At the same time, the error in an individual retrieval due to the measurement uncertainty of the LWP and diffuse transmission needs to be estimated.

When using the duel frequency microwave radiometer from the SGP site, the conservative estimate of the uncertainty [Feingold et al., 2003] is taken as 30 gm/m^2 Harrison and Michalsky, [1994] have indicated that the standard deviation of the traditional Langley

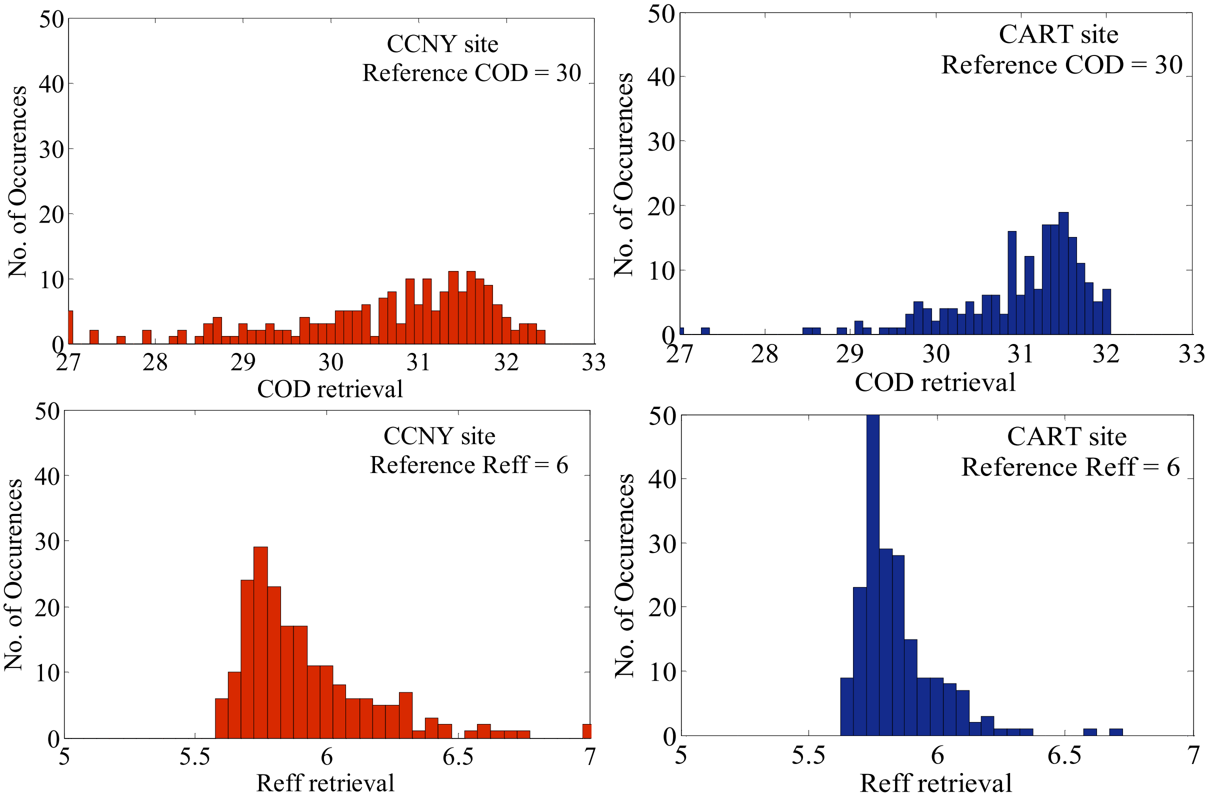

Figure 5.14: Cloud property retrieval dispersion due to aerosol model uncertainty (a) CCNY site (left panel), and (b) ARM SGP (or CART) site (right panel).

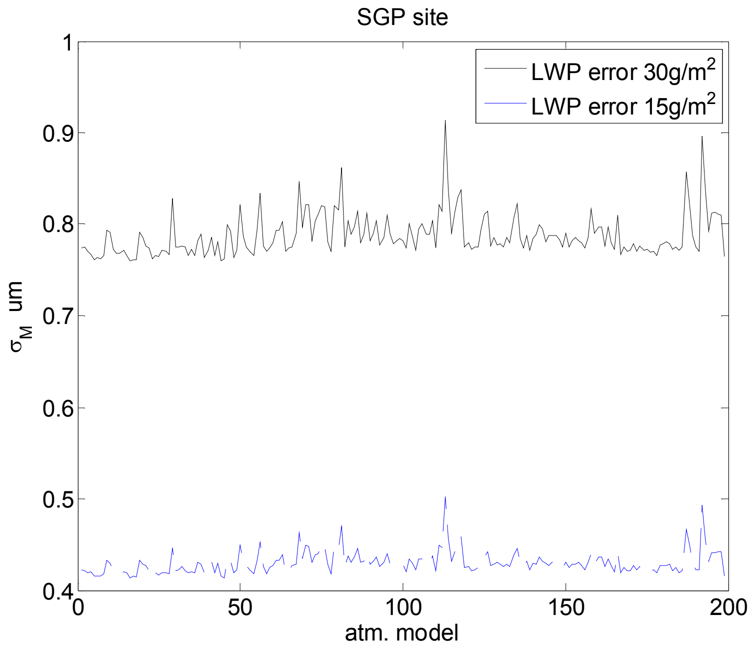

Figure 5.15: Standard error for cloud droplet effective radii (Reff).

analysis inferred extraterrestrial response from a single retrieval at a difficult site to be approximately 5%. The results of these uncertainties when applied to each ensemble element are quite stable with standard deviations in Reff = 0.8 μm of approximately 14%. On the other hand, we note that the addition of the MP-3000A MWR High frequency channels between 51 and 59 GHz can significantly improve the assumed error in the LWP retrieval [Crewell and Lohnert, 2003]. In particular, sensitivity studies estimate that LWP uncertainties to be reduced to 30 gm/m^2 . As illustrated in Figure 5.15, the measurement uncertainty is reduced by 50% to $\sim$ 7%.

Instrument radiometric uncertainties due to the sensor, data acquisitions etc. are significantly smaller and are not considered in the error budgets. Note that this "measurement" uncertainty dominates the errors we estimated due to uncertainty in the aerosol loading / surface albedo and ultimately all errors should be combined in quadrature resulting in estimated errors $\sim 20\%$. Based on the considerations by Feingold et al. [2003], dynamic changes in the cloud droplet effective radii are around 30% making these measurements quite challenging.

On the other hand, the ground based methods make some global assumptions including the requirements of single layer clouds and horizontal homogeneity (i.e., no broken clouds). The lack of broken clouds can be seen by imposing a buffer of 1 hour to the times when the lidar captures broken portion while coincident GOES data can assist in identifying single layer cases. Only when all these assets are combined we can quantitatively explore the changes in Aerosol Cloud Index (ACI).

5.5 Study case for aerosol-cloud interaction

To explore the aerosol-cloud interaction, we focus on an interesting case from those considered in [Kim et al., 2003]. Whereas in most cases considered, a weak correlation or no significant correlations, the case of April, 13, 2000 tends to show small anti-correlations. In their analysis, the surface extinction was obtained from ground based Nephelometer, which seemed to show a slight increase in cloud droplet radius with increase in extinction in opposition to the assumed aerosol cloud trend. One possible explanation advanced is that on this day, the surface was strongly decoupled from the cloud base aerosols. In Figure5.16, the Raman lidar derived extinction profile was shown for March 30, 2000. In particular, the period from 1500 - 1800 UTC time shows excellent horizontal homogeneity making the surface retrievals most reliable.

The high temporal density retrievals are given in Figure5.17 for our retrieval algorithm as well as the values obtained from both MIN and PAR algorithms. The results clearly show

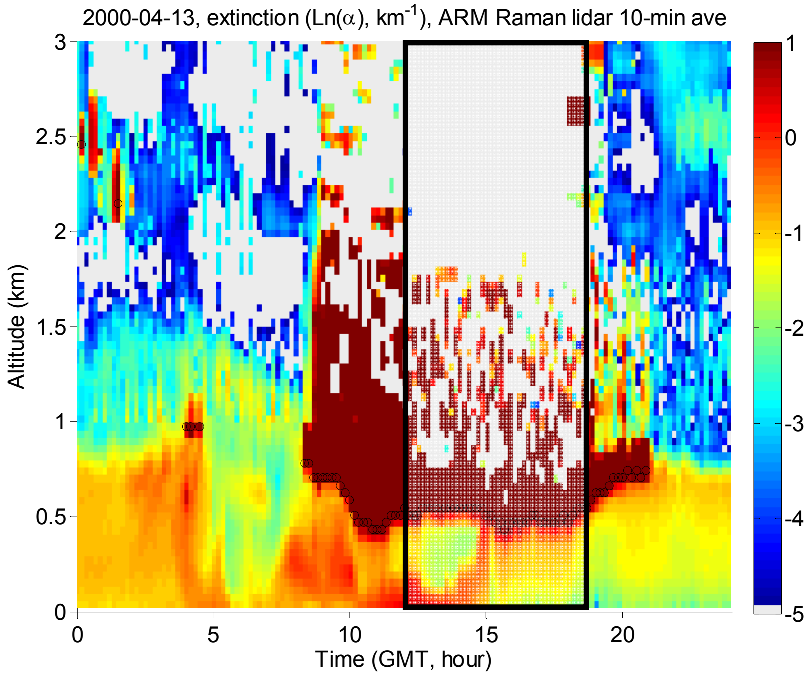

Figure 5.16: Raman Lidar derived extinction profile and marked cloud boundar for March 30, 2000 at ARM SGP site.

that our inversions closely follow those of MIN and the PAR approaches.

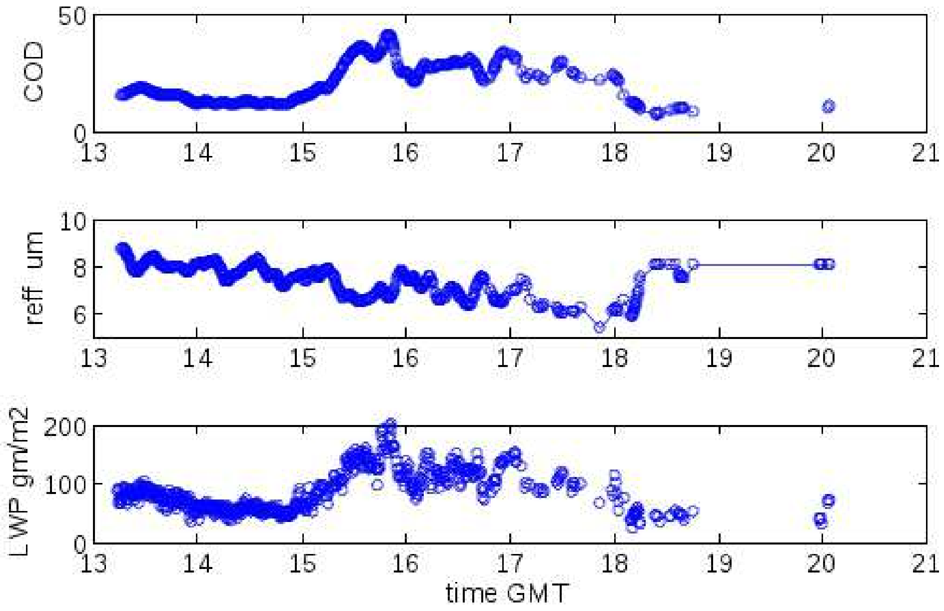

Figure 5.17: Cloud retrievals (a) COD (b) Reff (c) MWR LWP using all the three approaches for ARM SGP site on March 30, 2000.

In Figure 5.18 we plot on log scale the relationship between the effective radius and extinction where we consider both the surface extinction (lidar ground bin = 30 meters) as well as the extinction 150 meters below the cloud base. Here the cloud base was determined using a simple threshold of 1 m-1 and is displayed as black circles in figure 18. In addition, for each retrieval an approximate uncertainty for each measurement was obtained based on a quadrature sum of the errors We see that the surface results are at best uncorrelated with no trend but a clearer trend is seen when considering the aerosol 150 meters below cloud base. It must be remembered that we are using the uncertainty model associated with the LWP errors assumed for the two channel radiometer. Using the MP3000A significantly reduces

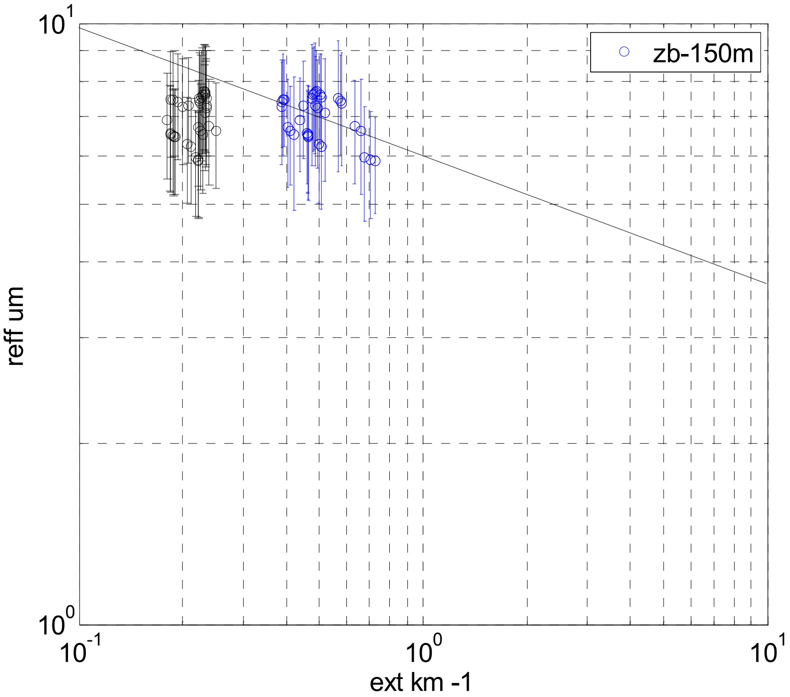

Figure 5.18: Log-Log plot of below cloud Raman extinction against the cloud effective radius.

the noise on the effective radius measurement improving the capability of this approach. In figure 19, as we might expect, we see a significant decoupling of the surface to the layer below cloud. Besides being more likely to mix with the cloud, aerosols close to the cloud are expected to have significant hygroscopic modification enhancing their extinction which is clearly seen in the lidar profile.

One way to see this coupling dynamics is to explore the relationship between the optical coefficients at the surface with both the Physical Particle Mass at the surface (PM2.5) as well as the relationship as a function of height. In making these calculations, we make use of the Vaisala Ceilometer which allows near field profiles to be measured. Although the noise of the ceilometer makes measurements above 1km very difficult, reasonable retrievals of backscatter can be obtained < 1km. An example of a ceilometer profile is given in Figure 5.19. Although we clip the figure at 300 meters to better compare against lidar, the height can be reduced to 10 meters due to the unique wide field optics of the ceilometer. Overlaid on the ceilometer backscatter is a wavelet derived PBL height. which compares well with that obtained from lidar during the time of overlap.

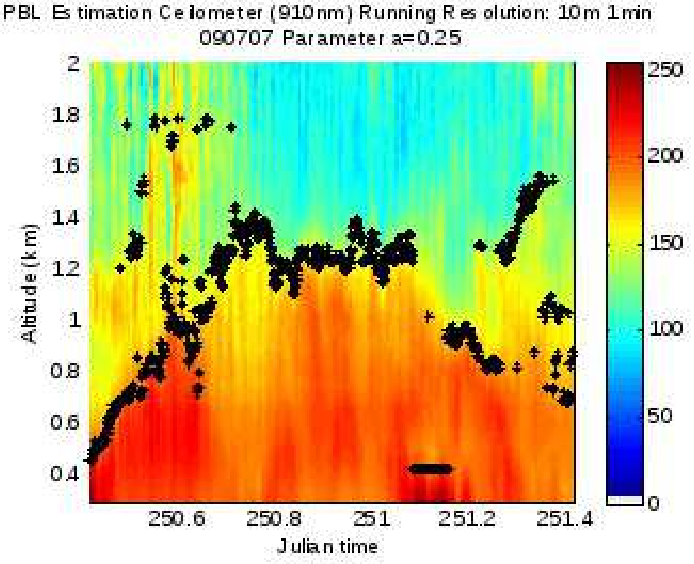

Figure 5.19: Near field ceilometer backscatter

Given the reasonable performance of the ceilometer backscatter, we can now address the vertical scales where the aerosols can couple to the surface. In particular, in Figure 5.20, we vary as a function of height the correlation between the ceilometer backscatter and the surface PM2.5 mass and note the strong decrease in correlation as we move away from the surface. This indicates that even for heights as low as 400 meters, it is possible to totally decouple from the surface making comparisons of cloud properties with surface aerosol measurements often useless.

In summary, we see that the surface measurements can be less than optimal in looking

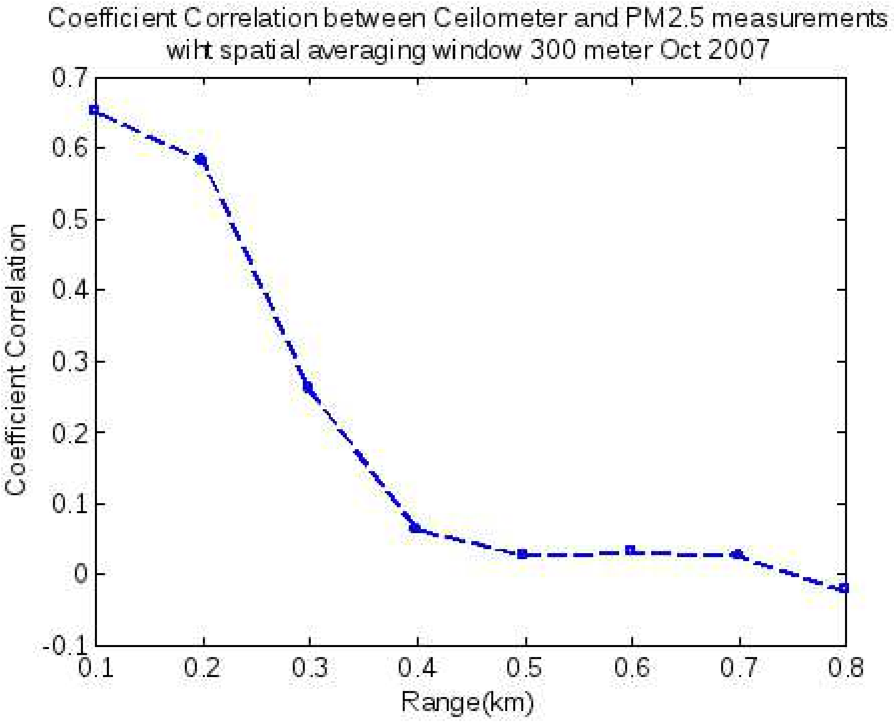

Figure 5.20: Correlation coefficient between ceilometer near-surface backscatter signal and TEOM PM2.5 concentration in the function of range

for aerosol cloud interactions and that profile measurements near the cloud base can be used to better probe these interactions under suitable conditions. Based on the regression slope, an IE exponent of 0.23 is obtained which is realistic if not on the high side in comparison to other cases seen [Feingold et al., 2003]. Clearly, the error budget we estimate is of the order of dynamic range making it hard to state that this is a clear observation of aerosol cloud interaction but in comparison to the surface, a clearer trend is detected.

Chapter 6

Future directions

In justifying the effort we are making to develop a comprehensive testbed, we make three points. The first point is that while the COD retrieval seems to be improved using the latest version of the VISST algorithm as seen in Figure 6.1, there still seems to be much difficulty with the effective radius retrieval directly. This is even more obvious using the latest version (Version 4) of the VISST algorithm including new calibrations and improved ozone correction from Mannis's group. Data over the SGP site was obtained from July 1 2011 to Nov 30,2011. We note excellent agreement with the COD (using a 30% homogeneity flag) to eliminate heterogeneous cloud fields. However, with the same flags in place, a strong bias and lack of correlation is observed in the effective radius. On the other hand, the LWP shows less bias than the effective radius. Therefore, the ground method which includes an independent LWP measurement is clearly important as a means to remove these biases. Second, we want to explore aerosol / cloud interactions over environmental and meteorological conditions very different than the SGP cite with more aerosol variability an urban heating mechanisms not seen at SGP. Third, we wish to demonstrate that more cost effective solutions which

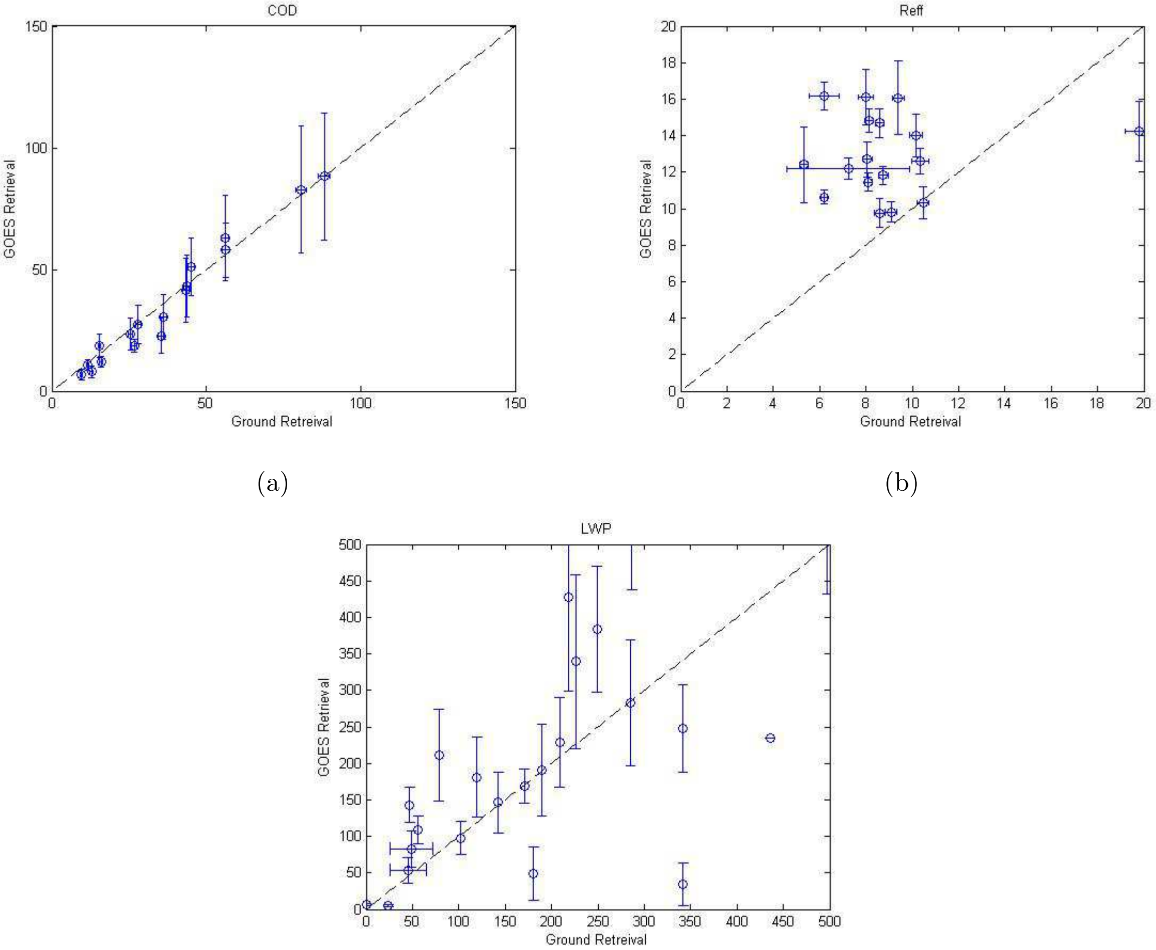

(a)

(b)

(c)

Figure 6.1: Comparison of ground based cloud retrievals with GOES VISST Version 4 a) COD, b) Reff, c) LWP

bypass the needs for Milimeter Radar are capable of studying this phenomenon. Finally, we want to explore modifications to the "standard" ARM site instrumentation that may provide improved capabilities.

6.1 Current Performance

Due to our limited database at present, we can compare only the cloud property comparisons. In particular, we have developed simultaneous measurements from MFRSR and MWR are available at CCNY (40.821438 N, 73.948114 W) from July 2011 - Sept 30. In our comparisons with the Satellite, we used an additional filter by ensuring that all the pixels were marked as water clouds. we first filter out the precipitation cases when merging the data from both the instruments and then calculate the mean and standard deviation for the cloud properties in 15 minute windows. The GOES East conus pixel netcdf files was not available as pixel data but is available as 20km gridded data which was obtained from `http://www-pm.larc.nasa.gov//cgi-bin/site/showdoc?docid=22&domain=eastconus&lkdomain=Y`. In order to compare the cloud retrievals from our approach with the GOES retrievals, we adopted the following filters for data screening:

(a) Out of all the available pixels, all 100% of them are not missing, and then the averaging is performed to obtain a single COD value representative for that time centering CCNY.

(b) The cloud phase of all the pixels within the 10 km angular radii shall be water clouds (=1).

(c) IR channel (10.8 μm) $>$ 255.0 K (for water clouds). In general, IR brightness temperature is considered as an indicator for cloud phase change.

(d) COD $>$ 100 are excluded because the ground measurements become so weak that sig-

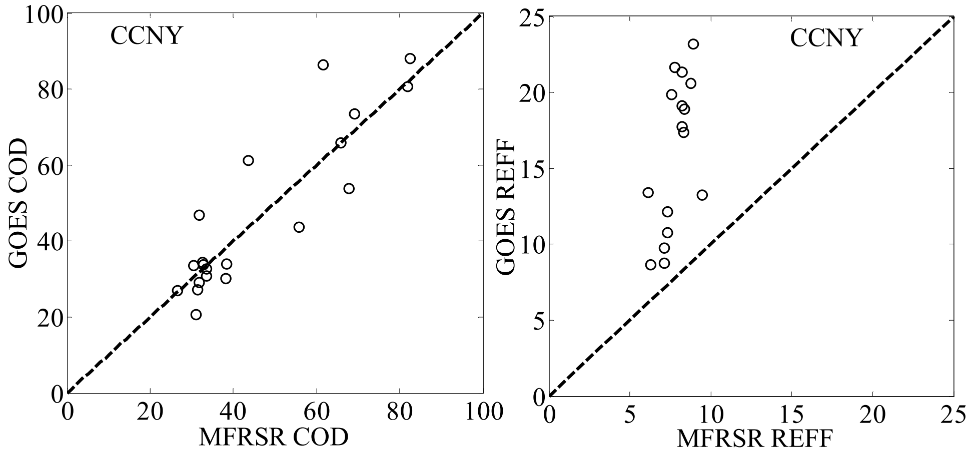

Figure 6.2: Comparison of ground based cloud retrievals with GOES at CCNY.

nal to noise ratio become too much and the noise drives the surface MFRSR down compared to GOES retrievals.

(e) At least one measurement both before and after the satellite observation time i.e., ±30 minutes, must be available from the ground retrievals.

(f) Use the matchups whose ratio of standard deviation to mean of COD and the effective radius are strictly less than 20% for both ground and satellite retrievals.

The correlations for COD and Reff are 0.82 and 0.62 respectively which compare favorably with the SGP matchups. In particular, we further restrict the MFRSR COD to Reff < 10 so we can focus on the cases where aerosol cloud interactions are dominant, which usually occur for low LWP ($< 200gm^2$) and Reff < 10 [Feingold 2003]. Again, we note that the results obtained Figure 6.2 are not biased for the COD while the magnitudes are off (2) for Reff retrievals. These results are in significant agreement with all the SGP retrievals we have made making it very difficult for satellites alone to quantify the effect.

6.2 Improvements in GOES Aerosol Retrievals

One of the biggest limitations is the need to assume a single aerosol model in the current operational GASP algorithm but as we can see, this can result in significant errors over regions where aerosol - cloud interactions can be expected to be significant such as biomass burning. One example is the fall season over the west coast we already mentioned in chapter 4. Other examples are recent wildfire burning in Long Island. We therefore will develop new LUT's which are more appropriate for biomass burning episodes. In addition, one of the major issues we need to confront is the extensive time needed to construct the LUT's needed for the inversion. However, we note that the inherent satellite retevial dispersion is much higher than that of MODIS due in part to lower SNR thresholds from geostationary platforms. Therefore, we propose to accelerate the calculation of new LUT's by using a subsampled LUT and performing multidimensional splines to allow better interpolation of the LUT. This would allow the time needed for LUT generation (>14 days) to be reduced to about 1 day. This will allow us to provide a wide database of LUT's which can be tuned to regional information from ground observations or MODEL forecasts.

6.3 Improvements in technology testbed

To begin, we consider the need to better assess vertical winds since the existence of vertical updrafts greatly improve the aerosol residency time in the interaction. In [Feingold et al., 2003], wind measurements were based on the Millimeter Wind Radar which gives winds within the clouds. Besides the great cost of this instrument, it is particularly desirable to obtain wind estimates below the cloud base which cannot be done this way. In this case,

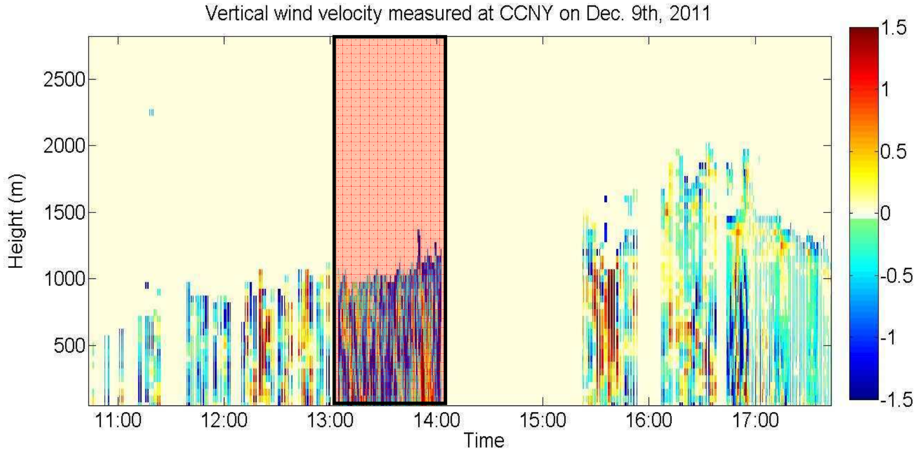

Figure 6.3: Vertical wind speed as a function of time up to 2 km.

the use of SODARS may be used for ranges below 200 meters but this limitation is clearly not optimal. In assisting this effort, we are making use of telecommunication technology to build more inexpensive Doppler wind lidar [Arend et al., 2012] that can be used to probe the vertical winds directly. This effort is being led by Dr. Mark Arend and his students. The representations of the vertical component of wind speed are shown in Figure 6.3. The lidar was operated in a purely vertical mode during the periods between 13:00 and 14:00 and also from about 16:45 on. An interesting feature to notice is the prominent down draft during 13:00-14:00 period as compared to more well mixed (both up and down drafts) in the earlier periods. Since there is no validation directly, we look at indirect evidence of this downdraft. In Figure 6.4 we plot the coincident lidar backscatter and note that during this interval, a significant collapse of the PBL was observed. It is also important to note that the use of the MWR with higher frequency bands deployed at CCNY can reduce the averaged error in LWP by 50%. The LWP result compared between the dual band MWR which is used at SGP site and our multispectral MWR was shown in Figure 5.4.

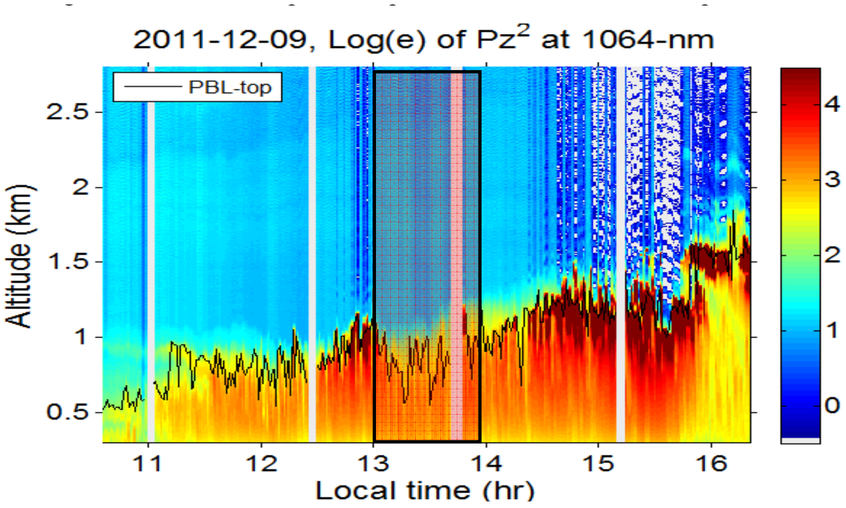

Figure 6.4: Coincident lidar backscatter profile illustrating collaps of PBL.

Bibliography

A.S. Ackerman, O.B. Toon, D.E. Stevens, A.J. Heymsfield, V. Ramanathan, and E.J. Welton. Reduction of tropical cloudiness by soot. *Science*, 288:1042–1047, 2000a.

A.S. Ackerman, O.B. Toon, J.P. Taylor, D.W. Johnson, P.V. Hobbs, and R.J. Ferek. Effects of aerosols on cloud albedo: Evalution of twomey's parameterization of cloud susceptibility using measurements of ship tracks. *J. Atmos. Sci.*, 57:2684–2695, 2000b.

A.S. Ackerman, M.P. Kirkpatrick, D.E. Stevens, and O.B. Toon. The impact of humidity above stratiform clouds on indirect aerosol climate forcing. *Nature*, 432:1014–1017, 2004.

B.A. Albrecht. Aerosols, cloud microphysics and fractional cloudiness. *Science*, 245:1227–1230, 1989.

M.D. Alexandrov, A.A. Lacis, B.E. Carlson, and B. Cairns. Remote sensing of atmospheric aerosols and trace gases by means of multifilter rotating shadowband radiometer. part i: Retrieval algorithm. *J. Atmos. Sci.*, 59:524–543, 2002.

M. Arend, S. Abdelazim, D. Santoro, F. Moshary, B. Gross, Y. Wu, and S. Ahmed. Fiber coherent doppler lidar development for characerization of planetary boundary layer dynamics and comparison to other vertical profilers. *26th International Laser Radar Conference (ILRC 26)*, 2012.

F.M. Breon, D. Tanre, and S. Generoso. Aerosol effect on cloud droplet size monitored from satellite. *Science*, 295:834–838, 2002.

R.F. Cahalan. Bounded cascade clouds albedo and effective thickness. *Nonlinear Proc. Geophys.*, 1:156–167, 1994.

I. L. Chang, C. Dean, M. Weinreb, X. Wu, D. Han, K. Mitchell, Z. Li, G. Sindic-Rancic, and F. Yu. Using raw star signals in the monitoring of goes imager visible-channel responsivities. In *Proc. SPIE 7081*, page 70810G, 2008.

R.J. Charlson, S.E. Schwartz, J.M. Hales, R.D. Cess, J.A. Coakley, J.E. Hansen, and D.J. Hofmann. Climate forcing by anthropogenic aerosols. *Science*, 25:426–430, 1992.

J.A. Coakley, R.L. Bernstein, and P.A. Durkee. Effect of ship-track effluents on cloud reflectivity. *Science*, 237:1020–1022, 1987.

J.A. Coakley Jr. and C.D. Walsh. Limits to the aerosol indirect radiative effect derived from observations of ship tracks. *J. Atmos. Sci.*, 59:668–680, 2002.

S. Crewell and U. Lohnert. Accuracy of cloud liquid water path from ground-based microwave radiometry - 2. sensor accuracy and synergy. *Radio Sci.*, 38:73–81, 2003.

J.A. Curry. Interactions among turbulence, radiation, and microphysics in arctic stratus clouds. *J. Atmos. Sci.*, 43:90–106, 1986.

C. Davies. Size distribution of atmospheric particles. *Aerosol Science*, 5:293–300, 1974.

A. Davis and A. Marshak. Levy kinetics in slab geometry: Scaling of transmission probability. *Fractal Frontiers*, pages 63–72, 1997.

P.Y. Deschamps, F.M Bréon, M. Leroy, A. Podaire, A. Bricaud, J.C. Buriez, and G. Seze. The polder mission: instrument characteristics and scientific objectives. *IEEE Trans. Geosci. Remote Sens.*, 32:598–615, 1994.

J.L. Deuzé, F.M. Bréon, and C. Devaux. Remote sensing of aerosols over land surfaces from polder-adeos-1 polarized measurements. *J. Geophys. Res.*, 106(D5):4913–4926, 2001.

D.J. Diner. *Multi-angle Imaging Spectro-Radiometer (MISR) level 2 aerosol retrieval algorithm theoretical basis document.* http://www-misr.jpl.nasa.gov.

D.J. Diner, J.V. Martonchik, R.A. Kahn, B. Pinty, N. Gobron, D.L. Nelson, and B.N. Holben. Using angular and spectral shape similarity constraints to improve misr aerosol and surface retrieval over land. *Remote Sens. Environ.*, 94:155–171, 2005.

X. Dong, T.P. Ackerman, E.E. Clothiaux, P. Pilewskie, and Y. Han. Microphysical and radiative properties of boundary layer stratiform clouds deduced from ground-based measurements. *J. Geophys. Res.*, 102:23829–23843, 1997.

X. Dong, P. Minnis, G.G. Mace, W.L. Smith, M. Peollot, R. T. Marchand, and A.D. Rapp. Comparison of stratus cloud properties deduced from surface, goes, and aircraft data during the march 2000 arm cloud iop. *J. Atmos. Sci.*, 59:3256–3284, 2002.

O. Dubovik and B. Holben. Variability of absorption and optical properties of key aerosol types observed in worldwide locations. *J. Atmos. Sci*, 59(3):590–608, 2002a.

O. Dubovik and B. Holben. Non-spherical aerosol retrieval method employing light scattering by spheroids. *Geophys. Res. Lett.*, 29(10):GL0141506, 2002b.

O. Dubovik and M.D. King. A flexible inversion algorithm for retrieval of aerosol optical properties from sun and sky radiance measurements. *J. Geophys. Res.*, 105:20673–20696, 2000.

O. Dubovik, A. Sinyuk, T. Lapyonok, B.N. Holben, M. Mishchenko, P. Yang, T.F. Eck, H. Volten, O. Minunoz, B. Veihelmann, W.J. van der Zander, J.-F. Leon, M. Sorokin, and I. Slutsker. Application of spheroid models to account for aerosol particle nonsphericity in remote sensing of desert dust. *J. Geophys. Res*, 111:D11208, 2006. doi: 10.1029/2005JD006619.

V. Estelles, M. Campanelli, M. P. Utrillas, F. Exposito, and J. A. Martínez-Lozano. Comparison of aeronet and skyrad4.2 inversion products retrieved from a cimel ce318 sunphotometer. *Atmos. Meas. Tech.*, 5:569–579, 2012. doi: 10.5194/amt-5-569-2012.

F.F. Evans and G.L. Stephens. A new polarized atmospheric radiative transfer model. *J. Quant. Spectrosc. Radiat. Transfer.*, 5:413–423, 1991.

G. Feingold, W.L. Eberhard, D.E. Veron, and M. Previdi. First measurements of the twomey aerosol indirect effect using ground-based remote sensors. *Geophys. Res. Lett.*, 30:1287, 2003.

A.S. Frisch, C.W. Fairall, G. Feingold, T. Uttal, and J.B. Snider. On cloud radar and microwave radiometer measurements of stratus cloud liquid water profile. *J. Geophys. Res.*, 103(D18):23195–23197, 1998.

N. Fukuta and L. A. Walter. Kinetics of hydrometeor growth from a vapor-spherical model. *J. of the Atmo. Sci.*, 27:1160–1172, 1970.

R.D. Garreaud, J. Rutllant, J. Quintana, J. Carrasco, and P. Minnis. Cimar-5: A snapshot of the lower troposphere over the subtropical southeast pacific. *Bull. Am. Meteorol. Soc.*, 82:2193–2207, 2001.

T. J. Garrett and P.V. Hobbs. Long-range transport of continental aerosols over the atlantic ocean and their effects on cloud structure. *J. Atmos. Sci.*, 52:2977–2984, 1995.

J.Y. Han and J.J. Baik. Theoretical studies of convectively forced mesoscale flows in three dimensions. part i: Uniform basic-state flow. *J. Atmo. Sci.*, 66:947–965, 2009.

Q. Han, W. B. Rossow, J. Zeng, and R. Welch. Three different behaviors of liquid water path of water clouds in aerosol-cloud interactions. *J. Geophys. Res.*, 59:726–735, 2002.

G. Hanel. The properties of atmospheric aerosol particles as functions of relative humidity at thermodynamic equilibrium with surrounding moist air. *Advance in Geophy.*, 19:73–188, 1976.

J.E. Hansen, M. Sato, and R. Ruedy. Radiative forcing and climate response. *J. Geophys. Res.*, 102,D6:6831–6864, 1997.

J.E. Hansen, M. Sato, A. Lacis, R. Ruedy, I. Tegen, and E. Matthews. Climate forcing in the industrial era. *Proc. Natl. Acad. Sci.*, 95:12753–12758, 1998.

L.C. Harrison, J.J. Michalsky, and J. Berndt. Automated multifilter rotation shadowband radiometer: An instrument for optical depth and radiation measurements. *Appl. Opt.*, 33: 5118–5125, 1994.

A. Hauser, D. Oesch, and N. Foppa. Aerosol optical depth over land: Comparing aeronet, avhrr and modis. *Geophys. Res. Lett.*, 32, 2005a.

A. Hauser, D. Oesch, N. Foppa, and S. Wunderle. Noaa avhrr derived aerosol optical depth over land. *J. Geophys. Res.*, 110:D08204, 2005b.

A.K. Heidinger, V. R. Anne, and C. Dean. Using modis to estimate cloud contamination of the avhrr data record. *J. Atmos. Oceanic Technol.*, 19:586–601, 2001.

M. Herman, J.L. Deuzé, C. Devaux, P. Goloub, F.M. Breon, and D. Tanre. Remote sensing of aerosols over land surfaces including polarization measurements and application to polder measurements. *J. Geophys. Res.*, 102(D14):17039–17049, 1997.

M. Hess, P. Koepke, and I. Schult. Optical properties of aerosols and clouds: The software package opac. *Bull. Am. Met. Soc.*, 79:831–844, 1998.

B.N. Holben, T.F. Eck, I. Slutsker, D. Tanre, J.P. Buis, A. Setzer, E. Vermote, J.A. Reagan, Y.J. Kaufman, T. Nakajima, F. Lavenu, I. Jankowiak, and A. Smirnov. Aeronet - a federal instrument network and data archive for aerosol claracterization. *Remote Sens. Environ.*, 66:1–16, 1998.

B.N. Holben, D. Tanre, and A. Smirnov. An emerging ground-based aerosol climatology: Aerosol optical depth from aeronet. *J. Geophys. Res.*, pages 12067–12097, 2001.

J. T. Houghton, Y. Ding, D.J. Griggs, M. Noguer, P.J.V. der Linden, X. Dai, K. Maskell, and C.A. Johnson. *Climate Change 2001: The Scientific Basis. Contribution of Working group I to the Third Assessment Report of the Intergovernmental Panel on Climate Change.* Cambridge University Press, 2001.

R.B. Husar, J.M. Prospero, and L.L. Stowe. Characterization of tropospheric aerosols over the oceans with the noaa advanced very high resolution radiometer optical thickness operational product. *J. Geophys. Res.*, 102(D14):16889–16901, 1997.

A. Ignatov and L. Stowe. Aerosol retrievals from individual avhrr channels. part i: Retrieval algorthm and transition from dave to 6s radiaton transfer model. *J. Atmos. Sci.*, 59: 313–334, 2002.

H. Jiang, H. Xue, A. Teller, G. Feingold, and Z. Levin. Aerosol effects on the lifetime of shallow cumulus. *Geophys. Res. Lett.*, 33:L14806, 2006.

C. Junge. The size distribution and aging of natural aerosols as determined from electrical and optical data in the atmosphere. *J. Appl. Meteorol.*, 12:13–25, 1955.

C. Junge. Air chemistry and radioactivity. *Int. Geophys. Series*, 4, 1963.

R.A. Kahn, P. Banerjee, and D. McDonald. Sensitivity of multiangle imaging to natural mixtures of aerosols ovre ocean. *J. Geophy. Res.*, 106(D16):18219–18238, 2001.

Y. J. Kaufman, I. Koren, L. A. Remer, D. Rosenfeld, and Y. Rudich. The effect of smoke, dust and pollution aerosol on shallow cloud development over the atlantic ocean. *Proc. Nal. Acad. Sci.*, 102:111207–11212, 2005.

Y.J. Kaufman and C. Sendra. Algorithm for atmospheric corrections. *Int. J. Rem. Sens.*, 9: 1357–1381, 1988.

Y.J. Kaufman and D. Tanre. *Algorithm for remote sensing of tropospheric aerosol from MODIS: MOD04 ATBD Document.* 1998.

Y.J. Kaufman, A.E. Wald, L.A. Remer, B-C. Gao, R-R. Li, and L. Flynn. The modis 2.1

νm channel-correlation with visible reflectance for use in remote sensing of aerosol. *IEEE Trans. Geosci. Rem. Sens.*, 35:1286–1298, 1997.

J.T. Kelly, C.C Chuang, and A.S. Wexler. Influence of dust composition on cloud droplet formation. *Atmospheric Environment*, 41(14):2904–2916, 2007.

B.G. Kim, S.E. Schwartz, M.A. Miller, and Q.L. Min. Effective radius of cloud droplets by ground-based remote sensing: Relationship to aerosol. *J. Geophy. Res.*, 108:125, 2003.

K.R. Knapp. Quantification of aerosol signal in goes 8 visible imagery over the united states. *J. Geophys. Res.*, 107(D20):4426–4438, 2002a.

K.R. Knapp, T. H. Vonder Haar, and Y. J. Kaufman. Aerosol optical depth retrieval from goes-8: Uncertainty study and retrieval validation over south america. *J. Geophys. Res.*, 107(D7):4055, 2002b. doi: 10.1029/2001JD000505.

K.R. Knapp, R. Frouin, S. Kondragunta, and A. I. Prados. Towards aerosol optical depth retrievals over land from goes visible radiances: Determining surface reflectance. *Int. J. Remote Sens.*, 26(18):4097–4116, 2005.

A. Kokhanovsky. *Aerosol optics: light absorption and scattering by particles in atmosphere.* Springer, 2008.

S. Kondragunta, P. Lee, J. McQueen, C. Kittaka, A. I. Prados, P. Ciren, I. Laszlo, R. B. Pierce, R. Hoff, and J. J. Szykman. Air quality forecast verification using satellite data. *J. Appl. Meteor. Climatol.*, 47:425–442, 2008.

E. Leontieva and K. Stamnes. Remotely sensed measurements of cloud optical depth using a ground-based multi-filter rotating shadowband radiometerin the arctic (methodology). *3rd Circumpolar Symposium on Remote Sensing of Arctic Environment*, 1994.

R.C. Levy, L. Remer, S. Mattoo, E. Vermote, and Y.J. Kaufman. Second generation algorithm for retrieving aerosol properties over land from modis spectral reflectance. *J. Geophys. Res.*, 112:D13211, 2007a.

R.C. Levy, L. Remer, and O. Dubovik. Global aerosol properties and application to modis aerosol retrieval over land. *J. Geophys. Res.*, 112:D13210, 2007b.

U. Lohmann. Aerosol effects on clouds and climate. *Space Sci. Rev.*, 125:129–137, 2006.

G.G. Mace, T.A. Ackerman, P. Minnis, and D.F. Young. Cirrus layer microphysical properties derived from surface-based millimeter radar and infrared interferometer data. *J. Geophys. Res.*, 103:23207–23216, 1998.

J.V. Martonchik, D.J. Diner, R.A. Kahn, T.P. Ackerman, M.M. Verstraete, B. Pinty, and H.R. Gordon. Techniques for the retrieval of aerosol properties over land and ocean using multi-angle imagery. *IEEE Trans. Geosci. Remote Sens.*, 36:1212–1227, 1998.

J.V. Martonchik, D.J. Diner, R.A. Kahn, and B. Gaitley. Comparison of misr and aeronet aerosol optical depths over desert sites. *Geophys. Res. Lett.*, 31:L16102, 2004.

J.V. Martonchik, R.A. Kahn, and D.J. Diner. *Retrieval of aerosol properties over land using MISR observations in: Satellite Aerosol Remote Sensing Over Land.* Springer, 2009.

T. Matsui, H. Masunaga, S. M. Kreidenweis, R. A. Pielke Sr., W. K. Tao, M. Chin, and Y. J. Kaukman. Satellite-based assessment of marine low cloud variability associated with aerosol atomspheric stability, and the diurnal cycle. *J. Geophys. Res.*, 111:D17204, 2006.

J. C. Maxwell. Theory of the wet bulb thermometer. *The Scientific Papers of James Clerk Maxwell*, 2:636–640, 1890.

Q.L. Min and L.C. Harrison. Retrievals of thin cloud optical depth from a multifiler rotating shadowband radiometer. *J. Geophys. Res.*, 109:D02201, 1996a.

Q.L. Min and L.C. Harrison. An adjoint formuation of the radiative transfer method. *J. Geophys. Res.*, 101:1635–1640, 1996b.

P. Minnis, D.P. Garber, D. F. Young, R.F Arduini, and Y. Takano. Parameterization of reflectance and effective emittance for satellite remote sensing of cloud properties. *J. Atmos. Sci.*, 55:3313–3339, 1998.

P. Minnis, W.L. Smith, D.F. Young, L. Nguyen, A.D. Rapp, P.W. Heck, and M.M. Khaiyer. Near-real-time retrieval of cloud properties over the arm cart area from goes data. *Proc. 12th Atmos. Radiat. Meas. Sci. Team Meet*, page 7, 2002.

M.I. Mishchenko and L.D. Travis. Satellite retrieval of aerosol properties over the ocean using polariztion as well as intensity of reflected sunlight. *J. Geophys. Res.*, 102:16989–17013, 1997a.

M.I. Mishchenko and L.D. Travis. Satellite retrieval of aerosol properties over the ocean using polariztion as well as intensity of reflected sunlight: Effect of instrumental errors and aerosol absorption. *J. Geophys. Res.*, 102:13543–13553, 1997b.

G. Myhre, F. Stordal, M. Johnsrud, Y.J. Kaufman, D. Rosenfeld, T. Storelvmo, J.E. Kristjansson, T.K. Berntsen, A. Myhre, and I.S.A. Isaksen. Aerosol-cloud interaction inferred from modis satellite data and global aerosol models. *Atmo. Chem. Phys.*, 7(12):3081–3101, 2007.

F. Nadal and F.M. Bréon. Parameterization of surface polarized reflectance derived from polder spaceborne measurements. *IEEE Trans. Geosci. Remote Sens.*, 37:1709–1718, 1999.

T. Nakajima, A. Higurashi, K. Kawamoto, and J.E. Penner. A possible correlation between satellite-derived cloud and aerosol microphysical parameters. *Geophys. Res. Lett.*, 28(7): 1171–1174, 2001.

S. Nicholls and J. Leighton. An observational study of the structure of stratiform cloud sheets, part 1, structure. *Q. J. R. Meteorol. Soc.*, 112:431–460, 1996.

V.R. Noonkester. Droplet spectra observed in marine stratus cloud layers. *J. Atmos. Sci.*, 41:829–845, 1984.

W. Ott. A physical explanation of the lognormality of pollutant concentrations. *J. Air Waste Manage. Assoc.*, 40:1378–1383, 1990.

R. Palikona, P. Minnis, D.A. Spangenberg, M.M. Khaiyer, M.L. Nordeen, J.K. Ayers, L. Nguyen, Y. Yi, P.K. Chan, Q.Z. Trepte, F.-L. Chang, and W.L. Smith, Jr. Nasa-langley web-based operational real-time cloud retrieval products from geostationary satellite. *Proc. of SPIE*, 6408:64081P, 2006.

R. Pincus, M. Szczodrak, J.J. Gu, and P. Austin. Uncertainty in cloud optical depth estimates made from satellite radiance measurements. *J. Clim.*, 8:1453–1462, 1995.

S. Platnick, M.D. King, S. Ackerman, P. Menzel, B. Baum, J.C. Riedi, and R.A. Frey. The modis cloud products: Algorithms and examples from terra. *IEEE Trans. Geosci. Remote. Sens.*, 41:459–473, 2003.

A. I. Prados, S. Kondragunta, P. Ciren, and K. R. Knapp. Goes aerosol/smoke product (gasp) over north america: Comparisons to aeronet and modis observations. *J. Geophys. Res.*, 112:D15201, 2007.

P.Ricchiazzi, S. Yang, C. Gautier, and D. Sowle. Sbdart: A research and teaching software tool for plane-parallel radiative transfer in the earth's atmosphere. *Bull. Amer. Meteo. Soc.*, 79:2101–2114, 1998.

H. R. Pruppacher and J. D. Klett. *Microphysics of Clouds and Precipitation: Second Revised and Enlarged Edition with an Introduction to Cloud chemistry and Cloud Electricity.* Kluwer, Dordrecht, 1998.

L.F. Radke, J.A. Coakley, and M.D. King. Direct and remote sesning obervations of the effects of ships on clouds. *Sci. Mag.*, 246:1146–1149, 1989.

L.A. Remer, D. Tanre, Y.J. Kaufman, R. Levy, and S. Mattoo. Algorithm for remote sensing of tropospheric aerosol from modis: Collection 005 atbd document. 2005.

D. Rosenfeld. Aerosol-cloud interactions contrl of earth radiatioin and latent heat release budgets. *Space Sci. Rev.*, 125:149–157, 2006.

B. Schmid, C. Matzler, A. Heimo, and N. Kampfer. Retrieval of optical depth and size distribution of tropospheric and stratospheric aerosols by means of sun photometry. *IEEE. Geosci. Remote Sens.*, 35(1):172–182, 1997.

B. Schmid, P.R. spyak, S.F. Biggar, C. Wehrli, J. Sekler, T. Ingold, C. Matzler, and N. Kampfer. Evaluation of the applicability of solar and lamp radiometric calibrations of a precision sun photometer operationg between 300 and 1025 nm. *Appl. Opt.*, 37(18): 3923–3941, 1998.

G.L. Schuster, O. Dubovik, and B.N Holben. Angstrom exponent and bimodal aerosol size distributions. *J. Geophys. Res.*, 111:D07207, 2006.

S. E. Schwartz. Kinetics of cloud droplet activation. *American Chemical Society 219th National Meeting*, pages PHYS–223, 2000.

J. Seinfeld and S. Pandis. *Atmospheric Chemistry and Physics: From Air Pollution to Climate Change*. Wiley, 1998.

M. Sekiguchi, T. Nakajima, K. Suzuki, K. Kawamoto, A. Higurashi, D. Rosenfeld, I. Sano, and S. Mukai. A study of the direct and indirect effects of aerosols using global satellite data sets of aerosol and cloud parameters. *J. Geophys. Res.*, 108(D22):4699, 2003.

J. L. Shereshefsky and S. Steckler. A study of the evaporation of small drops and of the relationship between surface tension and curvature. *J. chem. Phys.*, 4:108, 1936.

A. Slingo, S. Nicholls, and J. Schmetz. Aircraft observation of marine stratocumulus during jasin. *Q. J. R. Meteorol. Soc.*, 108:833–856, 1982.

K. Stamnes, S. Tsay, W. Wiscombe, and K. Jayaweera. Numerically stable algorithm for discrete-ordinate-method radiative transfer in multiple scattering and emitting layered media. *Appl. Opt.*, 27:2502–2509, 1988.

G.L. Stephens and C.M.R. Platt. Aircraft observation of the radiative and microphysical properties of stratocumulus and cumulus cloud field. *J. Clim. Appl. Meteorol.*, 26:1243–1269, 1987.

L.L. Stowe, P. A. Davis, and E. P. McClain. Scientific basis and initial evaluation of clavr-1 global clear/cloud classification algorithm for the advanced very high resolution radiometer. *J. Atmos. Oceanic Technol.*, 16:656–681, 1999.

L.L. Stowe, P.A. Davis, and E.P. McClain. Scientific basis and initial evalution of clvar-1 global clear/cloud classification algorithm for the advanced very high resolution radiometer. *J. Atmos. Oceanic Technol*, 16:656–681, 2002.

O. Torres, P.K. Bhartia, J.R. Herman, A. Sinyuk, P. Ginoux, and B. Holben. A long term record of aerosol optical depth from toms: Observations and comparison to aeronet measurements. *J. Atmos. Sci.*, 59:398–413, 2002.

D.D. Turner, C.H. Lo, and Q. Min. Cloud optical properties from the multi-filter shadowband radiometer (mfrsrcldod): An arm value added product,. 2004.

S. Twomey. The influence of pollution on the shortwave albedo of clouds. *Journal of the Atmospheric Sciences*, 34(7):1149–1152, 1977.

E. Vermote, D. Tanre, J. L. Deuze, M. Herman, , and J. J. Morcrette. Second simulation of the satellite signal in the solar spectrum, 6s: An overview. *IEEE Trans. Geosci. Remote*, 35:675–686, 1997.

VIIRS. Aot atbd 2010 viirs aerosol optical thickness (aot) and particle size parameter algorithm theoretical basis document (atbd). 2010.

A. Vlasenko, S. Sjogren, E. Weingartner, H. Gaggeler, and M. Ammann. Generation of submicron arizona test dust aerosol: Chemical and hygroscopic properties. *Aerosol Sci. Technol.*, 39(5):452–460, 2005.

S. Wang, Q. Wang, and G. Feingold. Turbulence, condensation, and liquid water transport in numerically simulated nonprecipitating stratocumulus clouds. *J. Atmos. Sci.*, 60:262–278, 2003.

F. Waquet, B. Cairns, K. Knobespiesse, J. Chowdhary, L.D. Travis, B. Schmid, and M.I. Mishchenko. Polarimetric remote sensing of aerosols over land. *J. Geophys. Res.*, 114: 1206, 2009. doi: 1029/2008JD010619.

M. Weinreb, M. Jamieson, N. Fulton, Y. Chen, J. X. Johnson, J. Bremer, C. Smith, and J. Baucom. Operational calibration of geostationary operational environmental satellite-8 and-9 imagers and sounders. *Appl. Opt.*, 36:6895–6904, 1997.

M. Weinred and D. Han. http://www.oso.noaa.gov/goes/goes-calibration/goes-vis-ch-calibration.htm, 2009.

K. Whitby. The physical characteristics of sulfur aerosols. *Atmos. Environ.*, 12:135–159, 1978.

C. T. R. Wilson. On the comparative efficiency as condensation nuclei of positivly and negatively charged ions. *iPhilos. Trans. R. Soc. Lond.*, A 193:289–308, 1900.

W.J. Wiscombe. Improved mie scattering algorithm. *Appl. Opt.*, 19:1505–1509, 1981.

X. Wu. Post-launch calibration of goes imager visible channel using modis. In *2003 International Symposium on Spectral Sensing Research*, 2003.

X. Wu and F. Sun. Improved post-launch calibration of goes imager visible channel using modis data. In *SPIE 2005*, 2005.

X. Wu, T. C. Stone, F. Yu, and D. Han. Vicarious calibration of goes imager visible channel using the moon. In *SPIE Proceedings Vol. 6296*, 2006.